Lunar Space Weathering by Charged Particles:

Reconsidering the Roles of Solar Wind and Solar Energetic Particle Events

by

Morgan Leigh Shusterman

A Dissertation Presented in Partial Fulfillment
of the Requirements for the Degree
Doctor of Philosophy

Approved December 2022 by the
Graduate Supervisory Committee:

Mark S. Robinson, Co-Chair
Thomas G. Sharp, Co-Chair
Maitrayee Bose
Charles A. Hibbitts
Steven Semken

ARIZONA STATE UNIVERSITY

August 2023

ABSTRACT

Space weathering of planetary surfaces is a complex process involving many mechanisms that work independently over different timescales. This research aims to address outstanding questions related to solar wind rim formation on space weathered regolith and tests a new hypothesis that dielectric breakdown plays an important role in the optical maturation of lunar regolith. The purpose of this work is to highlight the limitations imposed by laboratory equipment to accurately simulate the solar wind's effects on regolith and to provide physical context for the possible contributions of dielectric breakdown to space weathering. Terrestrial and lunar samples were experimentally irradiated and damage was characterized using electron microscopy techniques. Low-fluence proton irradiation produced differential weathering in a lunar mare basalt, with radiation damage on some phases being inconsistent with that found in the natural lunar environment. Dielectric breakdown of silicates revealed two electrical processes that produce characteristic surface and subsurface damage, in addition to amorphous rims. The results of this research highlight experimental parameters that if ignored, can significantly affect the results and interpretations of simulated solar wind weathering, and provides a framework for advancing space weathering research through experimental studies.

This dissertation is dedicated to Susan J. Shusterman.

ACKNOWLEDGMENTS

I would first like to thank my husband, Mr. Benjamin Wing, for supporting me through every high and the many lows that come along with completing a graduate degree. Completing this degree without your endless, selfless support would have been an impossibility.

I would also like to thank my mom, Ms. Susan Shusterman, who has listened to me complain about being in school since Kindergarten; longer than any parent should have to endure. I promise I am done now, and forever. Thank you for giving up your dreams so that I could achieve mine.

Thank you to my family and friends, who were each supportive in their own ways. To Mr. Samuel Shusterman and Mr. G. Patrick Stoner, I am so appreciative of you both for being continually supportive throughout my life. We can finally plan that trip to Europe! To Dr. Michael Pickens and Mr. J. Corey Thompson, there are no words to express my gratitude for our friendship, which has endured against all odds. From Receptionist to Doctor, you have been my most stable rock. To Dr. Sheridan Moore, after six years I still haven't figured out how we're friends, but what a privilege it has been to go through some of life's biggest changes with you. Look at us now! I am forever grateful for your friendship. To Dr. Mallory Kinczyk, thank you for always lending a listening ear and asking about what is going well in life. You reminded me that for all the things that go wrong, there is always at least one thing going right. To Dr. Sean Czarnecki, thanks for your engaging conversations and for always making work travel more fun. Graduate school would not have been the same without you and Pizza Mondays.

Thank you to my committee for graciously putting up with me. To Dr. Mark Robinson, thank you for supporting research that challenges well-accepted hypotheses, and for always providing opportunities to attend conferences and trainings that most other graduate students could only wish for. To Dr. Thomas Sharp, thank you for your enthusiasm, technical expertise, and willingness to try something new. Without your curiosity, much of my research would not have been possible. It was a pleasure to learn together. To Dr. Steven Semken, thank you for supporting such a non-traditional project. Your excitement and engagement made the work easier. I also thank you for helping to improve my technical writing. To Dr. Maitrayee Bose, thank you for engaging with my work in ways that made me consider other applications. I can always count on you to ask great questions that expand my understanding of a topic. To Dr. Charles Hibbitts, thank you for giving me a chance. I will never enjoy a job more than I enjoyed working directly with you. Thanks for sticking it out through my graduate program.

Finally, I would like to thank everyone who provided academic and technical support throughout my program: Dr. Caixia Bu, Dr. Roy Christoffersen, Dr. Catherine Dukes, Dr. Bruce Hapke, Dr. Anthony Irving, Dr. Noam Izenberg, Dr. Andrew Jordan, Dr. Lindsay Keller, Mr. Kenneth Mossman, Mr. Zia Rahman, Dr. Manuel Roldan Gutierrez, Mr. Emerson Speyerer, and Dr. Tim Stubbs. Every conversation, every question, and every lesson helped make me a better scientist.

TABLE OF CONTENTS

Page

CHAPTER Page

CHAPTER Page

LIST OF TABLES

LIST OF FIGURES

Figure Page

INTRODUCTION

1.1 Introduction to Space Weathering

The Moon provides an exceptional setting to study a number of Solar System processes, including the evolution and modification of planetary surfaces that result from exposure to the space environment. The scale of processes affecting surfaces varies greatly, but this work focuses on a subset of small-scale processes collectively referred to as *space weathering*. Space weathering occurs across the Solar System on planetary bodies with weak magnetospheres and tenuous exospheres or a complete lack of atmosphere. The rate at which space weathering modifies planetary surfaces depends largely on target composition, environmental factors, and distance from the Sun. A vast body of observational, theoretical, and experimental work has revealed several fundamental processes that contribute to space weathering, but there remains questions regarding the relative role of each process and the timescales over which they alter the surface. More work is required to resolve these questions and determine whether there are weathering processes yet to be detected.

The relationship between optical maturity and surface exposure time was first suggested by Gold (1955), who hypothesized that ion-solid interactions were the catalyst for surface darkening over time. Early laboratory simulations of the solar wind's interactions with silicate materials confirmed that the reflectance spectra of samples darkened and reddened with increasing exposure duration, but specific mechanisms for optical changes had not yet been determined (Wehner and KenKnight 1963, Rosenberg and Wehner 1964). Additional laboratory studies indicated the extent of darkening

achieved in a given sample was dependent on target composition; with equal radiation dosing, materials containing higher percentages of FeO became darker than samples containing less FeO (Hapke 1965; Hapke et al. 1970). The discovery that darkening was intimately coupled to FeO content was transformative for our understanding of space weathering because it was the first indication that the production of native iron (Fe^0) was responsible for optical maturation.

Analyses of lunar materials during the Apollo missions ushered in a new era of research that propelled forward our understanding of the evolution of regolith on airless bodies. Results from microscopic analyses of regolith samples challenged the untested hypothesis that optical maturation was simply the result of native iron formation. The discoveries of agglutinates (Conel and Nash 1970) and of regolith fines having a lower albedo than intact rock (Adams and Jones 1970) complicated our understanding of the mechanisms that act to optically mature a surface. Several studies of Apollo grains confirmed the presence of iron nanoparticles and identified their locations within agglutinates and amorphous rims on crystalline grains (Hapke 1973, Housley et al. 1973; Hapke et al., 1975; Morris 1976). Other maturation parameters determined through regolith studies included thicknesses of amorphous rims, grain size fractions, density of solar flare tracks, and the number density of gas bubbles (Keller and McKay 1997; Pieters et al. 2000; Pieters and Noble 2016).

More recent studies have provided new insights to both space weathering mechanisms and its products. Analyses of extraterrestrial soil samples from the Moon and Itokawa indicate that multi-phase grains with the same surface exposure histories have developed radiation-induced alterations at markedly different rates (Matsumoto et al. 2015;

Burgess and Stroud 2017, 2018). Compared to earlier studies that confirmed a compositional dependency through reflectance spectroscopy, these studies utilized high-resolution TEM imaging of nanoparticles and amorphous rims. The relatively new ability to resolve features at a sub-nanometer scale is important because the size, orientation, and distribution of nanoparticles have a strong effect on the optical properties of soils (Keller and McKay 1993; Keller et al. 1998; Wentworth et al. 1999; Keller and Clemett 2001; Noble et al. 2007). Thompson et al. (2016) also found through an extensive investigation of Apollo grains that iron nanoparticles are not exclusively found in native form, as previously indicated by studies using magnetic resonance spectroscopy. The optical signatures of Fe^0, Fe^{2+}, and Fe^{3+} are unique and their varied presence may indicate that the valence state of iron is correlated to a grain's exposure age.

1.2 Outstanding Questions

Micrometeoroid and energetic particle bombardment are now broadly accepted as the two dominant space weathering processes throughout the Solar System (Pieters and Noble, 2016; Bennett et al., 2013; Hapke, 2001). The cumulative effects of these processes change the bulk structure of regolith and produce physical and chemical damage on individual grains that affects optical properties of the lunar surface. However, there are still several major effects of space weathering that have yet to be resolved.

Magnetic anomalies. Although the Moon lacks a global magnetic field, it possesses localized regions of stronger crustal fields referred to as *magnetic anomalies* (Hood et al., 2001; Helekas et al., 2001; Tsunakawa et al., 2015). Most magnetic anomalies are associated with *swirls* -- sinuous, high-albedo regolith with distributions that follow local

magnetic field lines (Denevi et al., 2016; Garrick-Bethell et al., 2011). The high albedos in these regions are predominantly thought to be caused by deflection of the solar wind and an associated decrease in solar wind weathering rates (Glotch et al., 2015; Deca et al., 2018; Blewett et al., 2021). However, Kaguya plasma and magnetic field data indicates electrons are trapped in closed field lines (Nishino et al., 2015). The resulting electrostatic fields could contribute to high albedos through compositional sorting, which is indicated by LRO-LAMP far-UV data (Hendrix et al., 2016).

Permanently shadowed regions. The Moon has an inclination of 1.5° relative to the ecliptic plane and as a result, topographic lows at high latitudes remain in permanent shadow. Without a direct line-of-sight to the Sun, these regions receive significantly less solar wind ion flux than illuminated regions. Although the implantation of solar wind ions is reduced and non-uniform in permanently shadowed craters (Zimmerman et al., 2011), cold temperatures that remain <100 K significantly affect the retention and diffusion rates of solar wind hydrogen in the regolith (Starukhina, 2006). LRO-LOLA albedo of PSRs in flat-floored craters are systematically high compared to illuminated craters floors (Qiao et al., 2019; Lucey et al., 2014). The origin of anomalously high albedos is unknown, but has been attributed to decreased solar wind weathering, decreased micrometeoroid bombardment, and increased hydrogen retention or water ice formation (Zuber et al., 2012; Lucey et al., 2014; Fisher et al., 2017; Huang et al., 2022). Whatever the cause, it seems to be more strongly correlated to maximum annual temperature than to incident particle flux (Fisher et al., 2017).

Latitudinal and longitudinal trends. Both latitudinal and longitudinal spectral trends have been identified across the lunar surface. The albedo of both mare basalts and

highlands materials is found to increase with increasing latitude, independent of compositional variation (Hemingway et al., 2015; Lemelin et al., 2016). The trend is attributed to differences in solar wind flux, which varies as a cosine function of latitude. Unlike micrometeoroid bombardment effects, space weathering rates by the solar wind are likely to vary as a function of latitude and thus, temperature. As such, the rates of micrometeoroid bombardment and solar wind weathering decouple with increasing latitude. Asymmetric space weathering has also been identified on crater walls, where solar particle shielding by Earth's magnetotail leads to east-west asymmetries (Sim et al., 2017; Jordan et al., 2022). Despite evidence that space weathering rates by the solar wind are coupled to latitude, FeO abundance has also been proposed as a critical factor (McFadden et al., 2019).

Space weathering processes across the lunar surface and other planetary bodies produce heterogeneous effects that complicate the interpretation of orbital data. Although we have developed a strong understanding of lunar material properties, compositions, and distributions, many questions remain unanswered that are related to how lunar materials evolve with time. More work is required to identify all processes that act to modify planetary regoliths, define the variables that control the functional rate of each process, and determine the relative contribution of each process to overall maturation.

1.3 Dissertation Organization

In the second chapter of this dissertation I will discuss the results of experimentally weathered materials by hydrogen ions with solar wind energies. The damage produced over short timescales across a number of minerals reveals that high beam fluxes used in

laboratory simulations of space weathering result in damage formation timescales several orders of magnitude larger than that which occurs in the natural lunar environment. In addition, it is demonstrated that at simulated short timescales, some crystals develop damage that does not occur in the natural environment even after millions of years of exposure time. The interpretation of damage produced during irradiation experiments needs to consider the effects of high-flux particle beams. Misinterpreting these results may significantly affect the interpretation of extraterrestrial samples and orbital data.

Recent theory suggests that in addition to micrometeoroid and solar wind bombardment, an additional process called "dielectric breakdown weathering" may significantly contribute to optical maturation of the lunar surface (e.g., Jordan et al., 2019, 2017, 2015, 2014). Although dielectric breakdown has been studied extensively in synthetic materials, its effects in natural silicates has not been well studied. This process, which is thought to occur during solar magnetic storms, may electrically charge grains within the top 1 mm of regolith. If the grains have a low enough conductivity and the fluence of particles is sufficiently large, the material dielectric strength can be overcome and electrical failure via arcing could occur. In chapter 3 I will present the results of experiments in which a series of minerals underwent dielectric breakdown by deep dielectric charging. I will highlight the characteristic microstructural and chemical damage produced by electrical discharging in natural silicates and infer how this process should affect optical maturation signatures on the lunar surface.

Chapter 4 will summarize the work of Chapter 2 and Chapter 3, and will provide some insight into how to move forward with experimental space weathering work to provide the most robust and accurate representation of the natural environment.

The final chapter diverges from the topic of lunar space weathering and instead discusses the challenges of working in STEM with a color vision deficiency. I will present a fundamental review of color vision physiology and an algorithm developed to help select color palettes for data visualization that are more perceptible for diverse color acuities. The algorithm is based on empirical data and modeled to produce adjacent colors that are as perceptibly different as possible. A web application for this algorithm is in development and the outline of how it works is also discussed.

1.4 References

Bennett, C. J., Pirim, C., & Orlando, T. M. (2013). Space-weathering of solar system bodies: A laboratory perspective. *Chemical reviews*, *113(12)*, 9086-9150.

Blewett, D. T., Denevi, B. W., Cahill, J. T., & Klima, R. L. (2021). Near-UV and near-IR reflectance studies of lunar swirls: Implications for nanosize iron content and the nature of anomalous space weathering. *Icarus*, *364*, 114472.

Burgess, K. D., & Stroud, R. M. (2017). Glassy with a Chance of Nanophase Iron: Space Weathering of Lunar Soil as Observed with Aberration-Corrected Scanning Transmission Electron Microscopy. *Microscopy Today*, *25*(3), 32-39.

Burgess, K. D., & Stroud, R. M. (2018). Coordinated Nano-Scale EDS and EELS Measurements of Lunar Space-Weathered Material. *Microscopy and Microanalysis*, *24*(S1), 716-717.

Conel, J. E., & Nash, D. B. (1970). Spectral reflectance and albedo of Apollo 11 lunar samples: Effects of irradiation and vitrification and comparison with telescopic observations. *Geochimica et Cosmochimica Acta Supplement*, *1*, 2013.

Deca, J., Hemingway, D. J., Divin, A., Lue, C., Poppe, A. R., Garrick-Bethell, I., ... & Horányi, M. (2020). Simulating the reiner gamma swirl: the long-term effect of solar wind standoff. *Journal of Geophysical Research: Planets*, *125*(5), e2019JE006219.

Denevi, B. W., Robinson, M. S., Boyd, A. K., Blewett, D. T., & Klima, R. L. (2016). The distribution and extent of lunar swirls. *Icarus*, *273*, 53-67.

Fisher, E. A., Lucey, P. G., Lemelin, M., Greenhagen, B. T., Siegler, M. A., Mazarico, E., ... & Zuber, M. T. (2017). Evidence for surface water ice in the lunar polar regions using reflectance measurements from the Lunar Orbiter Laser Altimeter and temperature measurements from the Diviner Lunar Radiometer Experiment. *Icarus*, *292*, 74-85.

Garrick-Bethell, I., Head III, J. W., & Pieters, C. M. (2011). Spectral properties, magnetic fields, and dust transport at lunar swirls. *Icarus*, *212*(2), 480-492.

Glotch, T. D., Bandfield, J. L., Lucey, P. G., Hayne, P. O., Greenhagen, B. T., Arnold, J. A., ... & Paige, D. A. (2015). Formation of lunar swirls by magnetic field standoff of the solar wind. *Nature communications*, *6*(1), 1-8.

Gold, T. (1955). The lunar surface. *Monthly Notices of the Royal Astronomical Society*, *115*(6), 585-604.

Halekas, J. S., Mitchell, D. L., Lin, R. P., Frey, S., Hood, L. L., Acuña, M. H., & Binder, A. B. (2001). Mapping of crustal magnetic anomalies on the lunar near side by the Lunar Prospector electron reflectometer. *Journal of Geophysical Research: Planets*, *106*(E11), 27841-27852.

Hapke, B. (1965). Effects of a simulated solar wind on the photometric properties of rocks and powders. *Annals of the New York Academy of Sciences*, *123*(1), 711-721.

Hapke, B. W., Cohen, A. J., Cassidy, W. A., & Wells, E. N. (1970). Solar radiation effects on the optical properties of Apollo 11 samples. *Geochimica et Cosmochimica Acta Supplement*, *1*, 2199.

Hapke, B. (1973). Darkening of silicate rock powders by solar wind sputtering. *The Moon*, *7*(3-4), 342-355.

Hapke, B., Cassidy, W., & Wells, E. (1975). Effects of vapor-phase deposition processes on the optical, chemical, and magnetic properties OE the lunar regolith. *The moon*, *13*(1), 339-353.

Hapke, B. (2001) Space weathering from Mercury to the asteroid belt, *Journal of Geophysical Research, 106*, 10039-10074.

Hemingway, D. J., Garrick-Bethell, I., & Kreslavsky, M. A. (2015). Latitudinal variation in spectral properties of the lunar maria and implications for space weathering. *Icarus*, *261*, 66-79.

Hendrix, A. R., Greathouse, T. K., Retherford, K. D., Mandt, K. E., Gladstone, G. R., Kaufmann, D. E., ... & Cahill, J. T. S. (2016). Lunar swirls: far-UV characteristics. *Icarus*, *273*, 68-74.

Hood, L. L., Zakharian, A., Halekas, J., Mitchell, D. L., Lin, R. P., Acuña, M. H., & Binder, A. B. (2001). Initial mapping and interpretation of lunar crustal magnetic anomalies using Lunar Prospector magnetometer data. *Journal of Geophysical Research: Planets*, *106*(E11), 27825-27839.

Housley, R. M., Grant, R. W., & Paton, N. E. (1973). Origin and characteristics of excess Fe metal in lunar glass welded aggregates. In *Lunar and Planetary Science Conference Proceedings* (Vol. 4, p. 2737).

Huang, Z., Nomura, K. I., Morrissey, L. S., & Wang, J. (2022). Molecular dynamics simulation of solar wind implantation in the permanently shadowed regions on the lunar surface. *Geophysical Research Letters*, *49*(18), e2022GL099333.

Jordan, A.P., T.J. Stubbs, J.K. Wilson, N.A. Schwadron, H.E. Spence, and C.J. Joyce (2014) Deep dielectric charging of regolith within the Moon's permanently shadowed regions, *Journal of Geophysical Research: Planets, 119,* 1806-1821.

Jordan, A.P., T.J. Stubbs, J.K. Wilson, N.A. Schwadron and H.E. Spence (2015) Dielectric breakdown weathering of the Moon's polar regolith, *Journal of Geophysical Research: Planets, 120,* 210-225.

Jordan, A.P., T.J. Stubbs, J.K. Wilson, N.A. Schwadron and H.E. Spence (2017) The rate of dielectric breakdown weathering of lunar regolith in permanently shadowed regions, *Icarus, 283,* 352-358.

Jordan, A. P., T. J. Stubbs, M. L. Shusterman, N. R. Izenberg, J. K. Wilson, P. O. Hayne, N. A. Schwadron and H. E. Spence (2019) How dielectric breakdown may contribute to the global weathering of regolith on the Moon. Icarus, 319, 785-794.

Jordan, A. P., Case, A. W., Wilson, J. K., & Huang, C. L. (2022). Evidence that Earth's magnetotail affects dielectric breakdown weathering on the Moon. *Icarus*, *383*, 115011.

Lemelin, M., Lucey, P. G., Neumann, G. A., Mazarico, E. M., Barker, M. K., Kakazu, A., ... & Zuber, M. T. (2016). Improved calibration of reflectance data from the LRO Lunar Orbiter Laser Altimeter (LOLA) and implications for space weathering. *Icarus*, *273*, 315-328.

Lucey, P. G., Neumann, G. A., Riner, M. A., Mazarico, E., Smith, D. E., Zuber, M. T., ... & Song, E. (2014). The global albedo of the Moon at 1064 nm from LOLA. *Journal of Geophysical Research: Planets*, *119*(7), 1665-1679.

Keller, L. P. & McKay, D. S. (1993). Discovery of vapor deposits in the lunar regolith. *Science, 261*(5126), 1305-1307.

Keller, L. P., & McKay, D. S. (1997). The nature and origin of rims on lunar soil grains. *Geochimica et Cosmochimica Acta*, *61*(11), 2331-2341.

Keller, L. P., & Clemett, S. J. (2001, March). Formation of nanophase iron in the lunar regolith. In *Lunar and Planetary Science Conference* (Vol. 32).

Keller, L. P., Berger, E. L., Zhang, S., & Christoffersen, R. (2021). Solar energetic particle tracks in lunar samples: A transmission electron microscope calibration and implications for lunar space weathering. *Meteoritics & Planetary Science*, *56*(9), 1685-1707.

Matsumoto, T., Tsuchiyama, A., Miyake, A., Noguchi, T., Nakamura, M., Uesugi, K., ... & Nakano, T. (2015). Surface and internal structures of a space-weathered rim of an Itokawa regolith particle. *Icarus*, *257*, 230-238.

McFadden, J., Garrick-Bethell, I., Sim, C. K., Kim, S. S., & Hemingway, D. (2019). Iron content determines how space weathering flux variations affect lunar soils. *Icarus*, *333*, 323-342.

Morris, R. V. (1976). Surface exposure indices of lunar rocks: A comparative FMR study. *Proceedings of the Seventh Lunar Planetary Science Conference*, *7*, 315-335.

Nishino, M. N., Saito, Y., Tsunakawa, H., Takahashi, F., Fujimoto, M., Harada, Y., ... & Shimizu, H. (2015). Electrons on closed field lines of lunar crustal fields in the solar wind wake. *Icarus*, *250*, 238-248.

Noble, S. K., Pieters, C. M. & Keller, L. P. (2007). An experimental approach to understanding the optical effects of space weathering. *Icarus, 192*(2), 629-642.

Pieters, C. M., Taylor, L. A., Noble, S. K., Keller, L. P., Hapke, B., Morris, R. V., ... & Wentworth, S. (2000). Space weathering on airless bodies: Resolving a mystery with lunar samples. *Meteoritics & Planetary Science*, *35*(5), 1101-1107.

Pieters, C. M., & Noble, S. K. (2016). Space weathering on airless bodies. *Journal of Geophysical Research: Planets*, *121*(10), 1865-1884.

Qiao, L., Ling, Z., Head, J. W., Ivanov, M. A., & Liu, B. (2019). Analyses of Lunar Orbiter Laser Altimeter 1,064-nm albedo in permanently shadowed regions of polar crater flat floors: Implications for surface water ice occurrence and future in situ exploration. *Earth and Space Science*, *6*(3), 467-488.

Rosenberg, D. L., & Wehner, G. K. (1964). Darkening of powdered basalt by simulated solar-wind bombardment. *Journal of Geophysical Research*, *69*(15), 3307-3308.

Sim, C. K., Kim, S. S., Lucey, P. G., Garrick-Bethell, I., & Choi, Y. J. (2017). Asymmetric space weathering on lunar crater walls. *Geophysical Research Letters*, *44*(22), 11-273.

Starukhina, L. V. (2006). Polar regions of the moon as a potential repository of solar-wind-implanted gases. *Advances in Space Research*, *37*(1), 50-58.

Thompson, M. S., Zega, T. J., Becerra, P., Keane, J. T., & Byrne, S. (2016). The oxidation state of nanophase Fe particles in lunar soil: Implications for space weathering. *Meteoritics & Planetary Science*, *51*(6), 1082-1095.

Tsunakawa, H., Takahashi, F., Shimizu, H., Shibuya, H., & Matsushima, M. (2015). Surface vector mapping of magnetic anomalies over the Moon using Kaguya and Lunar Prospector observations. *Journal of Geophysical Research: Planets*, *120*(6), 1160-1185.

Wehner, G. K., Kenknight, C. E., & Rosenberg, D. (1963). Modification of the lunar surface by the solar-wind bombardment. *Planetary and Space Science*, *11*(11), 1257-1261.

Wentworth, S. J., Keller, L. P., McKay, D. S., & Morris, R. V. (1999). Space weathering on the Moon: Patina on Apollo 17 samples 75075 and 76015. *Meteoritics & Planetary Science*, *34*(4), 593-603.

Zimmerman, M. I., Farrell, W. M., Stubbs, T. J., Halekas, J. S., & Jackson, T. L. (2011). Solar wind access to lunar polar craters: Feedback between surface charging and plasma expansion. *Geophysical research letters*, *38*(19).

Zuber, M. T., Head, J. W., Smith, D. E., Neumann, G. A., Mazarico, E., Torrence, M. H., ... & Melosh, H. J. (2012). Constraints on the volatile distribution within Shackleton crater at the lunar south pole. *Nature*, *486*(7403), 378-381.

SOLAR WIND WEATHERING: HIGH-FLUX DAMAGE OF EXPERIMENTALLY IRRADIATED NWA 12008 MARE BASALT

2.1. Abstract

Space weathering of lunar regolith results in physical and structural damage to grains that alters the spectral properties of the surface. Solar wind irradiation is one of the two dominant forms of space weathering that works to optically mature the surface. Despite decades of space weathering research, the relative contributions of individual processes to overall optical maturation remain unknown. To determine the rates of incipient rim development, we experimentally-irradiated a lunar mare basalt with a H^+ fluence equivalent to ~10 years of solar wind exposure. We present compositionally-dependent differential weathering damage and discuss the probable explanations for the development of damage types that are not found to form on the lunar surface.

2.2. Introduction

Minerals directly exposed to micrometeoroid bombardment and the impinging solar wind develop space weathered rims that preserve exposure histories and alter the spectral signatures of planetary surfaces over geologic timescales. The analyses of many lunar regolith grains have explicated the origins and physical nature of these nano-strata. However, there are several weathering mechanisms that each modify regolith grains over different timescales and it remains a challenge to identify the individual contribution of these mechanisms to overall maturation states. Our inability to effectively replicate the lunar environment in laboratory settings, which are used to simulate the effects of space

weathering mechanisms, is a likely source of discrepancy between artificially and naturally weathered samples. Here, we consider how high flux particle beams used in laboratory simulations of the solar wind may produce damage to grains at rates inconsistent with the natural lunar environment.

Space weathered rims are diverse in origin, structure, and chemical composition. Although four types of rims have been identified (Keller and McKay, 1997), all rims can be broadly classified as either indigenous or exogenous in nature. The two classifications are distinguishable based on their chemical likeness to their host grain and the abundance and areal distribution of submicroscopic metallic iron inclusions ($SMFe^0$). Indigenous rims have chemical compositions similar to their unaltered host grains and form as a result of direct solar irradiation. Exogenous rims form via melt and vapor deposition from nearby micrometeoroid impacts and have chemical compositions distinct from their host grains.

Because exogenous rims tend to contain larger and more abundant $SMFe^0$ than indigenous rims, they play a more critical role in forming the spectral characteristics of mature lunar soils: attenuated absorption features, positive spectral slopes, and overall lower albedos (Pieters and Noble, 2016; Noble et al., 2001). However, the deposition of exogenous rim-forming material is stochastic and therefore it is very difficult to constrain their formation timescales (Keller et al., 2021). To better understand the timescales over which weathered rims form, and to unravel the contribution of individual processes to optical maturation, it is useful to first constrain contributions from nonrandom processes such as solar wind irradiation.

Although we understand indigenous rims to form from solar wind processes, there

is no consensus regarding the types of damage produced by impinging ions on the Moon (e.g., whether solar wind exposure directly contributes to the formation of $SMFe^0$) nor the timescales over which optically detectable damage forms. This chapter presents the H^+ damage formed in a laboratory-irradiated lunar meteorite and concludes that the use of high particle flux beams in simulations of the solar wind may produce damage regimes inconsistent with those found in the natural lunar environment. Additional experiments to further constrain the effects of solar wind on lunar regolith are proposed.

2.2.1. Formation of Radiation-induced Rims

Exogenous rims are fully amorphous from the time of deposition, but amorphous, indigenous rims form by irradiation processes that develop over millions of years. When an incident ion enters the crystal lattice, its energy is transferred to atoms in the target material through electronic and nuclear interactions (Märk, 1994). Low-energy, low-mass ions produce damage cascades, in which energy is dissipated through knock-on collisions with the nuclei of atoms in the target material (Caturla et al., 1996). As kinetic energy is transferred through primary and collisional cascades, elementary defects such as vacancies and interstitials, are created along the incident ion pathway. Together referred to as Frenkel pairs, these defects are mobile and interact to achieve the most energetically favorable configuration (Fig. 2.1).

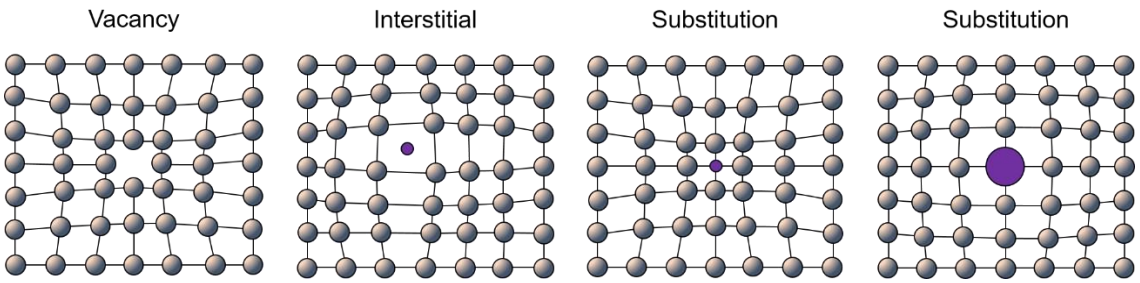

Figure. 2.1. Lattice Deformation. Radiation point defects in the crystal lattice. *Adapted from Dhaher, 2017*.

During prolonged irradiation, damage cascades begin to overlap and the proximity of elementary defects increases the probability of defect interactions (Fig. 2.2). The coalescence of interstitials and vacancies lead to the formation of clusters and holes, respectively (e.g., Jin et al., 2008; Sickafus et al., 2007). As these defects merge into larger structures, they become thermodynamically stable. Stretching and distortion of the lattice around these large structures creates small zones of amorphization. Molecular dynamics models of this process show how implantation cascades generate both isolated point defects and amorphous pockets (Pelaz et al., 2003).

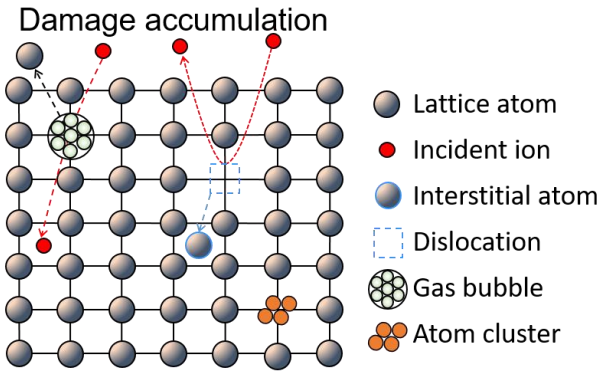

Figure 2.2. Point Defect Accumulation. Point defect accumulation in the crystal lattice.

Although persistent radiation can continually produce damage, the formation of

amorphous rims does not progress linearly with time. Defect formation and recovery are competing mechanisms that proceed simultaneously and dynamically as reaction parameters change. Target composition, distance from the Sun, surface temperatures, and magnetic fields can all affect the rate at which solar wind protons alter grain surfaces. However, the primary controls on defect formation and recovery rates are independent variables, where defect formation is primarily controlled by incident particle flux and defect recovery processes are controlled by target temperature (Goldberg et al., 1995). Rims formed by solar wind irradiation are found on materials throughout the Solar System, including the surfaces of interplanetary dust grains (Bradley and Brownlee, 1986), and the conditions under which these materials are affected play a role in the efficacy of solar wind ions to amorphize surfaces.

2.2.2 Estimated Rim Formation Rates

Despite the complicated process of solar wind-induced amorphization, significant efforts have been made to resolve the timescales over which lunar grains develop indigenous rims. Because of the number of independent variables that work to control amorphization rates, this task has been proven very difficult; no consensus has been reached.

SRIM (Stopping Range of Ions in Matter) model results have indicated that ~20 nm thick amorphous rims should form on olivine over ~10^2 years and that a steady-state should be reached in $5x10^3$-$1x10^4$ years (Christoffersen and Keller, 2015). Although SRIM is a popular program for modeling solid-ion interactions, it contains two constants that are non-ideal for the case of solar wind weathering: a fully amorphous target and an

assumed target temperature of 0 K (Ziegler et al., 2010). Both of these parameters significantly impact the rates of defect production and recovery.

In a study of lunar grains, Keller et al. (2016) compared the width of amorphous rims on lunar grains to the accumulation of solar flare particle tracks. Their results indicate that mature, stratified rims composed of indigenous and exogenous layers reach a steady state in 10^6-10^7 years (Keller and Zhang, 2015). The time to steady-state based on this lunar sample analysis is 2-4 orders of magnitude longer than rates predicted by SRIM models. Although rim thickness and solar flare track densities appear to be well correlated, these values assume that individual grains are exposed to the solar wind and to solar energetic particles (SEPs) for the same lifetime duration. Solar wind weathering requires line-of-sight to the Sun, while SEPs penetrate to depths >1 mm. It has not yet been demonstrated how these two particle populations could weather the surface over equivalent timescales.

Combining SRIM modeling with laboratory measurements of critical fluences required for amorphization in olivine, Poppe et al. (2018) found agreement with the formation timescales reported by Keller and Zhang (2015). The formation of 10-20 nm thick rims on olivine were estimated to form over 20-100 years of exposure to solar wind protons. This model also predicts that olivine should develop amorphous rims 100 nm thick over $5x10^4$ years, and 400 nm thick rims over ~$3x10^6$ years. Although this prediction qualitatively matches the timescale predicted by Keller and Zhang (2015), the thickness of rims estimated to form are inconsistent with what is observed in the lunar sample collection. Olivine rims are neither found to host amorphous indigenous rims, nor rims extending to depths >200 nm.

Without a consensus on the rates of indigenous rim formation, there exists opportunities to constrain the many parameters involved. To provide insight into incipient stages of rim formation, we irradiated a lunar mare basalt with protons to simulate 10 years of surface exposure time. Because all phases in the sample received the same particle dose, it was possible to compare early rim development as a function of composition.

2.3 Methods

A slide-mounted thin section of NWA 12008, a low-titanium lunar mare basalt, was provided by Dr. Anthony Irving of the University of Washington. The bulk composition, mineralogy, and shock metamorphism was previously characterized (Cohen et al., 2019; Zhang et al., 2019). The section used in these experiments consisted of olivine phenocrysts and elongated laths of plagioclase (likely maskelynite) surrounded by a fine groundmass of Ca-pyroxene (Fig. 2.3). Ilmenite and Ti-chromite were also present as accessory minerals.

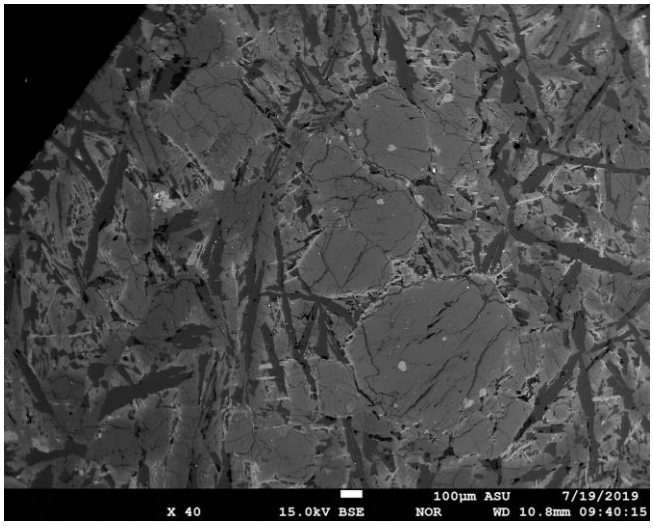

Figure 2.3. BSE Image of NWA 12008. Irradiated region from which TEM sections were extracted.

2.3.1 Experimental Procedures

Experimental treatments were completed in the Surface Analysis Chamber at the University of Virginia's Laboratory for Astrophysics and Surface Physics (LASP) (Fig. 2.4). Prior to irradiation, the section was cleaned in an ultrasonic bath of isopropyl alcohol three times to remove organic contamination.

Irradiation was performed with a differentially pumped, low-energy ion gun. For the duration of the experiment, the vacuum chamber pressure remained stable at (4.7 ± 0.2) x 10^{-9} Torr and the temperature remained stable at 300 ± 3 K. One keV hydrogen ions, which make up ~96% of the solar wind ions, were rastered uniformly across an area of diameter 5 ± 1 mm. Incident hydrogen ions were oriented normal to the sample surface and were accelerated by a Peabody Solar-Wind Accelerator with Wein filter.

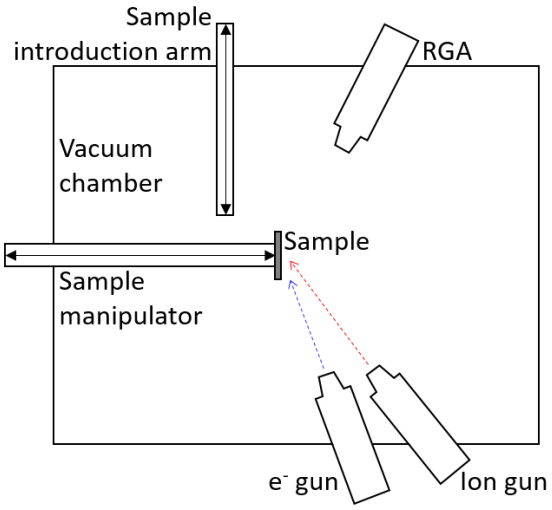

Figure 2.4. LASP Surface Analyzer Chamber. Schematic overview of the experimental chamber located at the University of Virginia's Laboratory for Astrophysics and Surface Physics.

The ion flux was measured with a Faraday cup before (2.9 x 10^{12} H^+ cm^{-2} s^{-1}) and after (4.2 x 10^{12} H^+ cm^{-2} s^{-1}) irradiation. Assuming an average flux of 3.55 x 10^{12} H^+ cm^{-2}

s^{-1} over a 5 hour duration, the sample received a total fluence of 6.4 x 10^{16} H^+ cm^{-2}. Approximately 10 years of surface exposure time on the Moon were simulated based on an average solar wind hydrogen flux of 1.92 x 10^8 H+ cm^{-2} s^{-1} (Hapke, 2001).

To prevent both electrostatic charging at the sample surface and H^+ deflection, we operated a low-energy (<2 eV) electron flood gun concurrently with the H^+ beam. A residual gas analyzer mounted at an angle of 60° with respect to the sample normal ran for the duration of the experiment to measure neutral and sputtered ions. To prevent surface alteration under atmospheric conditions, the section was removed from the sample chamber under N_2 purge and sealed an an N_2-filled bag for transport.

2.3.2 Electron Microscopy Analysis

2.3.2.1 Sample Preparation

Four transmission electron microscope (TEM) foils extracted from NWA 12008 were prepared with an FEI Duobeam Quanta 3D focused ion beam scanning electron microscope (FIB-SEM) at NASA's Johnson Space Center. An energy dispersive x-ray (EDS) spectrometer and backscattered electron images were used to locate regions of interest (ROI). We selected ROIs that included grain boundaries to maximize the number of phases studied while minimizing the number of foils required for the investigation. Selected regions included sections of olivine, pyroxene, ilmenite, and plagioclase glass (maskelynite). To prevent surface damage to the grain during ion milling, regions of interest received an ion-deposited carbon coating approximately 3 µm thick. A Ga^+ ion beam voltage of 30 kV and variable probe current was used for coarse milling. The sections were then platinum-welded to a Cu Lift-Out grid and thinned to electron

transparency (<100 nm). Final polishing was done at 5 kV and 48 pA. Prior to imaging the foils were stored in high-vacuum canisters to drive off adsorbed water.

2.3.2.2 S/TEM Imaging

Images were acquired with a Philips CM200-FEG and a JEOL ARM200F aberration-corrected, Schottky field-emission scanning transmission electron microscope (FE-STEM). Bright field (BF), medium-angle annular dark field (MAADF), and high-angle annular dark field (HAADF) image modes were used. Because bright field images are formed from the acquisition of transmitted electrons, they reveal differences in crystallinity and atomic mass. HAADF images are formed from the acquisition of high-angle scattered electrons and are useful for identifying differences in composition (atomic mass) and characterizing lattice defects. The CM200-FEG was operated at 200 kV with a probe diameter of ~2 Å and the ARM200F STEM was operated at 200 kV and 5.9 pA cm^{-2}, with a probe diameter of ~0.9 Å. Elemental mapping and line scan measurements were acquired with a JEOL 50 sq. mm windowless light-element-sensitive X-ray detector (EDS) and an ultra-fast Gatan Enfinium electron energy loss spectrometer (EELS), respectively.

2.4 Results and Interpretations

NWA 12008 was exposed to 10 years of simulated solar wind proton exposure. Four phases were evaluated for damage, including olivine, augite, ilmenite, and maskelynite. Each of the four phases developed radiation-induced damage layers with distinctive qualities, indicating that for a given proton fluence, differential weathering

occurs. Mass spectra acquired during irradiation showed no sputtered ions or neutrals, however, the lack of detection is likely the result of sub-optimal detector positioning. Unlike other experiments that have used much higher beam fluxes, no $SMFe^0$, gas-filled bubbles, or blisters were identified in any of the samples.

2.4.1 Olivine

The olivine developed a damaged region comprised of two layers (Fig. 2.5). The surface-most layer was fully amorphized to a depth of ~10 nm. Just below the fully amorphous layer was a partially amorphized layer with variable thicknesses of 7-15 nm. In some areas this subsurface layer appeared fully amorphous, indicating an advanced stage of the crystalline-to-amorphous transition. Both damaged layers had a mottled appearance in TEM bright field images with unknown cause. However, there was no evidence of $SMFe^0$ or gas-filled bubbles within either region.

Olivine on the surface of the Moon is not known to form fully amorphous rims. A surface-exposed olivine from rock 64455 has a solar wind exposure fluence of $1x10^{21}$-$1x10^{22}$ H^+ cm^{-2}, equivalent to ~2 million years, yet the rim is nanocrystalline rather than amorphous (Keller et al., 2016). However, in laboratory studies of space weathering by solar wind protons, the use of fluences 4-6 orders of magnitude larger than that at the Moon typically results in partial to fully amorphous rims in olivine (Carrez et al., 2002; Christoffersen et al., 2020, and other). Based on Keller et al. (2021), a ~30 nm rim should form over 15,000-20,000 years. In our olivine sample, we simulated 10 years of exposure time but produced an equivalent of ~18,000 years of damage. This discrepancy between the total supplied fluence to this sample and the extent of damage produced is a strong

indication that damage regimes produced in the laboratory under high-flux beams are inconsistent with those working at the lunar surface.

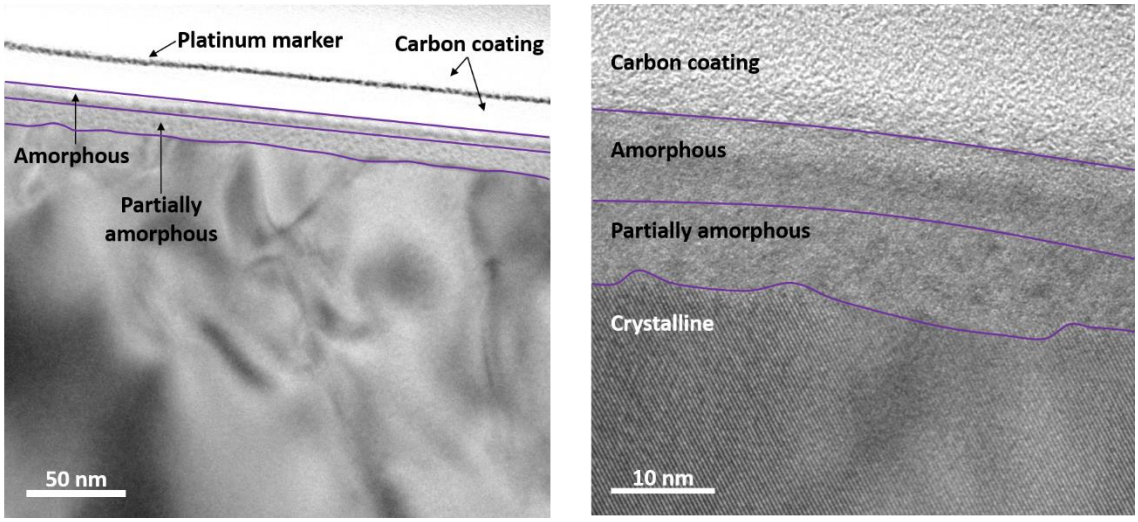

Figure 2.5. Irradiated Olivine. TEM bright field images of olivine from NWA 12008, irradiated with 1 keV H^+. A two-layered damage region formed with a supplied fluence of ~10^{16} H^+ cm^{-2}.

2.4.2 Augite

The augite developed a fully amorphous rim with a thickness of 20 nm. Contrast differences in bright field images indicate the rim is differentiated into a 5 nm upper layer and a 15 nm lower layer (Fig. 2.6). EDX maps indicate the upper layer is depleted in magnesium and oxygen compared to the lower layer and to the undamaged portion of the grain. A mottled texture is visible in bright field and dark field images and is the result of radiation damage effects and not an indication of the presence of either bubbles or iron nanoparticles. The mottling is also not correlated to regions of compositional depletion, so this is likely the result of lattice deformation caused by defect accumulation.

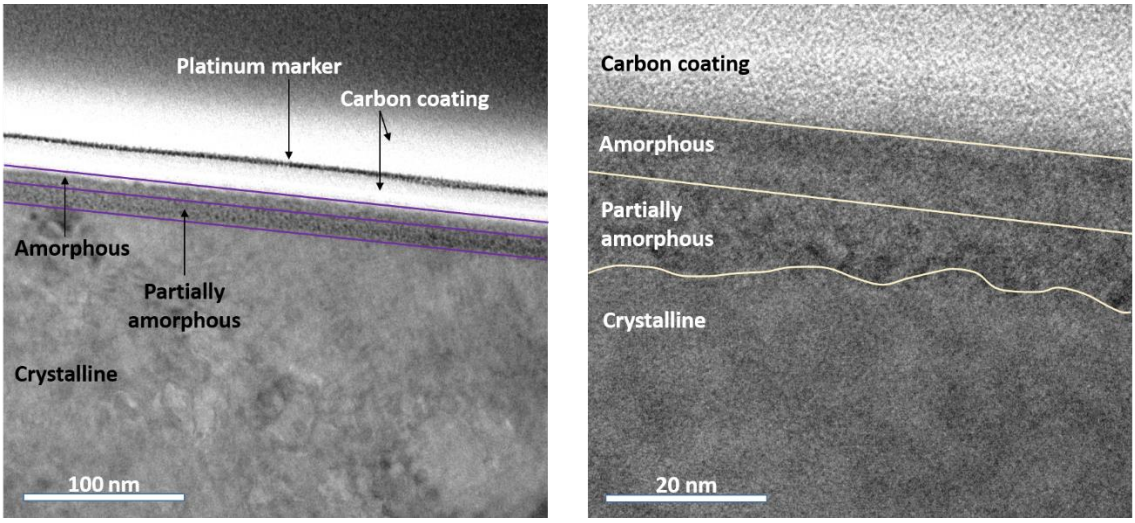

Figure 2.6. Irradiated Augite. TEM bright field images of augite from NWA 12008, irradiated with 1 keV H^+. A 2-layered damage region formed with a supplied fluence of ~10^{16} H^+ cm^{-2}.

2.4.3 Maskelynite

Proton irradiation of maskelynite, a high-density glassy plagioclase, formed a damaged region that in total, extended to a depth of ~190 nm. The region was capped by a smooth ~5 nm layer that was texturally and chemically indistinct from undamaged regions of the grain. This smooth layer extended along a grain boundary with ilmenite and terminated at a depth of ~190 nm (Fig. 2.7). Damage caused by nuclear collisions mainly takes place beyond the penetration depth of the incident ion (Li et al., 2013), and the penetration depth of 1 keV protons is ~5 nm. Thus, considering the smooth, unremarkable appearance within the top 5 nm of the sample, we interpret this layer to be free from significant accumulations of beam damage.

The primary damage layer extended between depths of 5- and 190-nm. This region was characterized by a mottled texture that increased in size and density with proximity to the irradiated surface. We ruled out electron beam damage as a source of

this texture because the density of mottling was surface-correlated and had an apparent scaling much smaller than the damage produced by the TEM electron beam. Additionally, there was no evidence of recrystallization within the mottled zone.

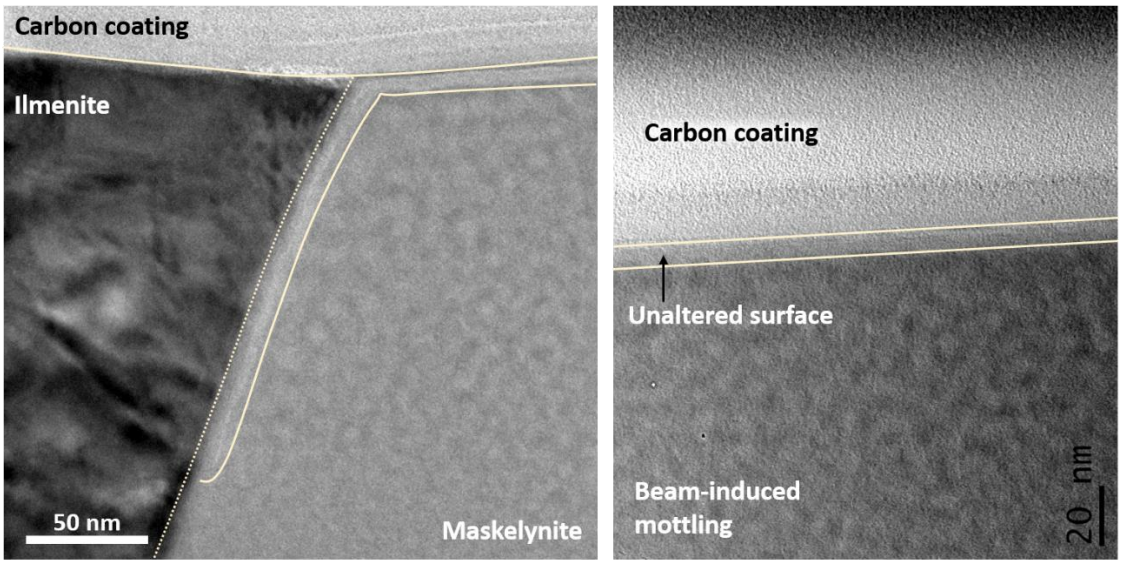

Figure 2.7. Irradiated Maskelynite. TEM bright field images of maskelynite from NWA 12008, irradiated with 1 keV H+. A ~5 nm surface layer retained no damage, but a ~185 nm layer shows evidence of lattice dilation with a supplied fluence of ~10^{16} H^+ cm^{-2}.

Irradiation of crystalline quartz and silicate glasses is known to affect material properties such as density. Dimensional changes to bond angles and lengths have been attributed to isotropic compaction (densification), dilation, and viscous flow (Hirsch et al., 2005; Devine, 1994). During irradiation, silicate structures dilate as point defects coalesce to form large structures. While crystalline quartz can remain dilated post-irradiation, relaxation near vacancies and voices in silicate glasses results in densification (An et al., 2006; Zhang et al., 2006; Piao et al., 2000; Fukumi et al., 1990). Because there was no evidence of partial recrystallization in the surface-correlated damaged layer, the

mottled texture is interpreted to be a change is glass density.

Lunar glasses have been meticulously studied and this texture has not been reported in the literature. Rather than being an inadvertently missed weathering effect, this lattice behavior is more likely to be an effect of non-ideal experimental conditions. The effects of proton irradiation on glass density depends on a number of factors including beam energy and total supplied dose. Thus, the change in density and lattice structure resulting from the rapid accumulation of defects may have an effect on spectral reflectance measurements of laboratory-irradiated samples that contain glassy phases.

2.4.4 Ilmenite

The positive identification of damage in ilmenite was difficult because the evaluated grain had a complex structure with multiple twins and extensive lattice strain. However, the effects of proton irradiation appeared to produce damage with variable thickness as a function of lattice orientation. In some areas, lattice fringes were seen extending to the sample surface, indicating no significant damage accumulation (Fig. 2.8). In other areas, there appeared to be short-range disorder. There were also some small areas in which a fully amorphous damaged layer extended 5-15 nm into the subsurface (Fig. 2.9).

Grain boundaries, including twins, facilitate anisotropic responses to irradiation. At these boundaries, there may be enhanced diffusion pathways and additional space within the lattice structure facilitates the accumulation of more point defects. In this sample, the depth of damage is shallowest near twin boundaries, indicating that those

regions are acting as sinks for the proton-induced defects. The variable depth of damage otherwise present is most likely attributable to grain orientations.

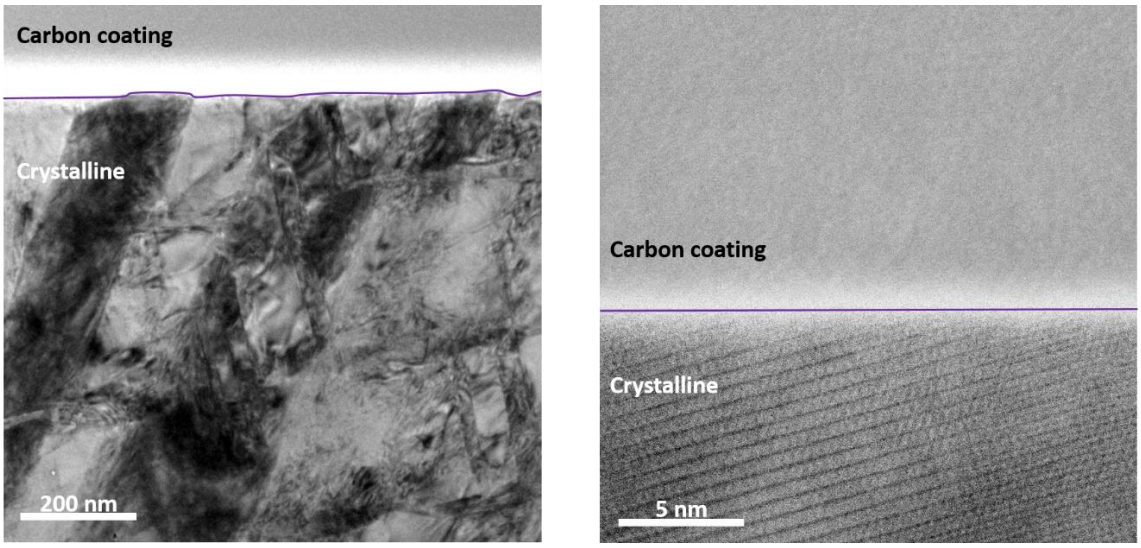

Figure 2.8. Irradiated Ilmenite. TEM bright field images of ilmenite from NWA 12008, irradiated with 1 keV H^+. A rim with variable thickness and short-range disorder formed with a supplied fluene of ~10^{16} H^+ cm^{-2}.

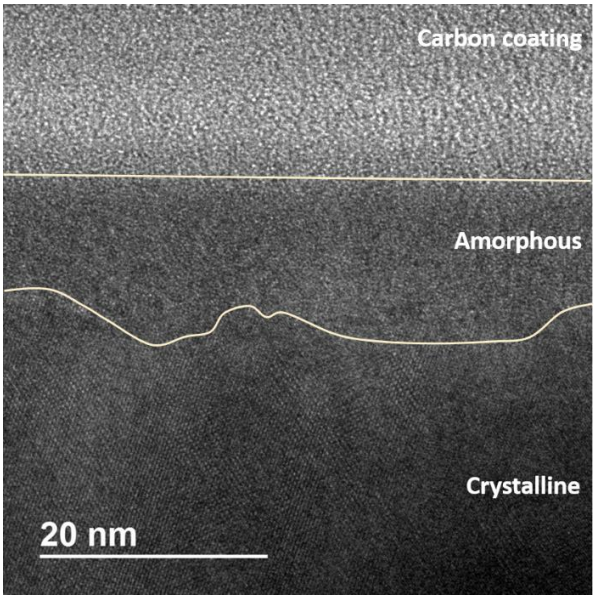

Figure 2.9. Amorphized Ilmenite. TEM bright field image of ilmenite from NWA 12008, irradiated with 1 keV H^+. A rim with variable thickness and short-range disorder formed with a supplied fluence of ~10^{16} H^+ cm^{-2}.

2.5 Discussion

The experimental results presented here support an ongoing effort to better constrain the effects of solar wind ions as a function of mineralogical variation and total proton fluence. Each mineral received a proton fluence equivalent to ~10 years of exposure time, significantly less than previous studies have considered (see Jordan, 2022 for a summary of experimental beam parameters). Amorphization occurred to some degree in all four minerals, but no evidence of $SMFe^0$ was found.

It is well established that solar wind implantation into lunar grains contributes to the formation of amorphous rims. However, not all minerals respond similarly to ionizing radiation; the structural complexity and symmetry of minerals partially determiens how susceptible they are to damage by ionizing radiation (Wang and Ewing, 1992). While a classification scheme exists to describe the physical characteristics of mature regolith grains, olivine and ilmenite stand out as exceptional cases (Keller and McKay, 1997; Christoffersen et al., 2020). Most mature minerals develop fully amorphous indigenous rims under the Moon's ambient radiation environment, but olivine and ilmenite remain relatively radiation-resistant. Analyses of grains from both the Moon and asteroid Itokawa reveal that olivine lacks radiation-induced amorphous rims and instead exhibits disordered, nanocrystalline rims up to 120 nm thick (e.g., Keller and Berger, 2014; Harries and Langenhorst, 2014). The amorphization of olivine and ilmenite in this study is in disagreement with the damage that forms on the same minerals exposed to the real space environment over much longer timescales and thus, raises questions about the limitations of laboratory-based solar wind simulations and the accuracy of derived maturation rates.

2.5.1 Particle Flux and Amorphization Rates

To better understand why laboratory-irradiated samples exhibit more severe damage regimes than those found on the lunar surface, it is important to consider how amorphous material develops and evolves. For a given material, amorphization is predominantly controlled by target temperature and incident particle flux, where flux controls the defect formation rate and temperature controls the rate of relaxation processes. These parameters act as independent variables in the crystalline-amorphous transition, so they should be controlled for individually in laboratory settings. Amorphization occurs only when the rate of defect formation exceeds the rate of defect recovery. As the incident particle flux increases, the probability of damage cascades overlapping and interacting also increases. The interaction of damage cascades accelerates the coalescence of point defects into large voids and clusters that stretch and distort the lattice, which terminates long-range order and forms small pockets of amorphization. Furthermore, pre-existing lattice defects are known to slow recovery processes, so rapidly accumulated damage also works to slow lattice recovery.

A complication introduced by using high beam fluxes in laboratory settings is that defect formation rates and recovery rates work over vastly different timescales. Particle flux controls the number of damage cascades that form over nanosecond timescales, while temperature affects lattice vibrational energies and controls recovery processes that work on timescales ranging from seconds to years, depending on environmental conditions. Thus, ion flux, target temperature, and target composition all play a role in how quickly amorphization occurs in the laboratory and the natural environment. On the lunar surface, where the proton flux is about $3x10^{8}$ H^{+} cm^{-2} s^{-1}, olivine seems to have

sufficient time for damage recovery processes. On the other hand, in the lab where we typically use fluxes 4 to 6 orders of magnitude larger than the solar wind flux at 1 AU, cascades are forming too quickly and preventing recovery processes, which leads to accelerated amorphization rates.

For a given material, amorphization is predominantly controlled by target temperature and incident particle flux, where flux controls the defect formation rate and temperature controls the rate of relaxation processes. These parameters act as independent variables in the crystalline-amorphous transition, so they must be controlled for individually. As the incident particle flux increases, the probability of damage cascades overlapping and interacting also increases. The interaction of damage cascades accelerates the coalescence of point defects into large voids and clusters that stretch and distort the lattice, causing small pockets of amorphization. Furthermore, pre-existing lattice defects are known to slow recovery processes, so rapidly accumulated damage also works to slow lattice recovery.

Although high flux particle beams can create damage regimes incongruent with processes at the lunar surface, the consideration of flux is additionally important for understanding heterogeneous solar wind access to the lunar surface. Magnetic anomaly deflection efficiency is as high as 50% locally for large fields, but deflections are also detected over weak and small-scale anomalies (Lue et al., 2011). More generally, the highest fluence of solar wind particles is deposited onto the farside, and the total ion impact rate is significantly inhibited by Earth's magnetotail (Kallio et al., 2019). At the poles, models indicate wake formation at permanently shadowed regions divert solar wind protons towards the shadowed crater floors (Zimmerman et al., 2011). These

heterogeneities, along with latitudinal variations in solar wind flux, motivate the need for experiments in which particle flux varies by several orders of magnitude. Evaluating the damage incurred under a range of beam fluxes will elucidate the accuracy of our analyses of experimentally weathered materials.

2.5.2 Target Temperature and Amorphization Rates

Although the high proton flux used in this study most likely accounted for the development of amorphous rims over such short timescales, the target temperature during irradiation should also be considered in future studies. Lattice dynamics greatly affect the recombination rate of defects. As temperatures increase, the amplitude of lattice vibrations increases and migration through the lattice occurs more readily. When flux is held constant, the total dose required for amorphization increases as the target temperature increases (Goldberg et al., 1995). Thus, flux and temperature parameters must be considered together to elucidate the true rates of solar wind-driven amorphization.

In general, damage production can be mitigated by simultaneous recovery processes during irradiation. The lifetime of a single cascade is ~10^{-11} s (Caturla et al., 1996). However, recovery processes work over timescales >1 s and macroscopic damage can take years to develop (Sickafus et al., 2007), depending on factors such as target temperature and pre-existing defect density (Wallace et al., 2019). The difference between these timescales is a critical factor in determining the amorphization rate or grains. On the lunar surface, the ratio of recovery to damage is higher than in a laboratory setting.

Most solar wind weathering experiments are performed at temperatures near 300 K despite lunar surface temperatures ranging from ~20-400 K. This large temperature variation will result in heterogeneous amorphization rates that vary as a function of latitude and local topography. Complicating factors such as daily temperature fluctuations are also likely to play a role – a diurnal hydrogen signature (Li and Milliken, 2017; Wöhler et al., 2017) may indicate some damage produced during nighttime exposure when regolith is cold, recovers during the day as temperatures rise. In permanently shadowed regions where temperatures are perpetually low and vibrational amplitudes are exceedingly small, non-heating recovery processes may play a negligible part in the space weathering process. Understanding how temperature-driven recovery rates affect the overall rate of amorphization will also help constrain the effects of weathering on other planetary bodies such as Mercury.

2.5.3 Dilation and Densification of Glass

Evidence of radiation-induced densification or dilation has not been identified in lunar glasses such as agglutinates or pyroclastic beads. Although density changes due to irradiation are compositionally dependent, with densification decreasing as SiO_2 content increases, it shows no significant dependence on temperatures below 400 °C (Hirsch et al., 2005). Thus, this effect would occur at any latitude and is unlikely to be excluded from the lunar sample collection. The response of maskelynite in these experiments was likely due to the use of a high proton flux. It is not evident whether the glass dilated or densified, but changes to density start when large voids are produced during irradiation which act to dilate the lattice. When active irradiation of silicate glasses ceases, it is

possible for the lattice to collapse around the voids resulting in overall densification of the lattice.

Although the response in maskelynite is incongruent with what is observed in extraterrestrial samples, this finding has implications for analyses samples that have been experimentally irradiated. Because the refractive index (RI) is inversely proportional to wavelength (Tan et al., 1998), and increasing densification increases the RI of silicate glasses, lattice density affects its spectral properties. The intensity of reflectance peaks and absorption bands decrease with increasing densification (Tan et al., 1998), which could provide an additive effect to the spectral response of nanophase iron. Additional studies that specifically examine irradiation effects in glassy silicates would provide insight into whether this response could contribute to optical maturation of experimentally-irradiated lunar regolith samples.

2.6 Conclusion

A lunar mare basalt irradiated with 1 keV protons to a fluence equivalent to 10 years of lunar surface exposure time, developed radiation-induced damage in olivine, augite, maskelynite, and ilmenite (Fig. 2.10). The amorphization of olivine and ilmenite, and the density change of maskelynite, under such a low fluence indicates that high flux beams used in laboratory solar wind simulations produce accelerated amorphization rates compared to damage accumulated in the natural environment. We need to be cognizant of the parameters that affect defect formation and recovery rates when trying to extract rim formation timescales or relative ages from the damage incurred by experimentally irradiated grains. Additionally, while most other phases do amorphize in the lunar

environment, the inclusion of olivine and ilmenite grains, or even glassy minerals in lab samples, may skew the interpretation of spectral effects due to irradiation.

Unfortunately, we were not able to derive incipient weathering rates from these experiments. However, the data was a reminder that in addition to weathering rates being a function of target composition, they are also a function of regolith temperature. Grains in colder areas should accumulate more damage than grains in warmer areas, assuming each receives the same flux. The data also indicates that much of the damage accumulated at night likely recovers during the day when temperatures rise. As a result, we should expect the formation timescales of weathered rims to be very complex and those timescales should contribute to heterogeneous rates of solar wind weathering across the Moon.

Although high flux beams are required to simulate processes that work over geologic timescales, mitigation efforts can be made to minimize the limitations posed by such beams. Improvements can be made to solar wind simulation experiments by decreasing beam flux as much as is practical, increasing the target temperature to enhance recovery rates, and performing experiments on both single-phase and mixed-mineral samples. Because amorphization is a non-linear process with rates that will vary across the lunar surface, controlling for target composition, target temperature, and particle flux would provide critical constraints to improve our interpretations of indigenous rim formation rates.

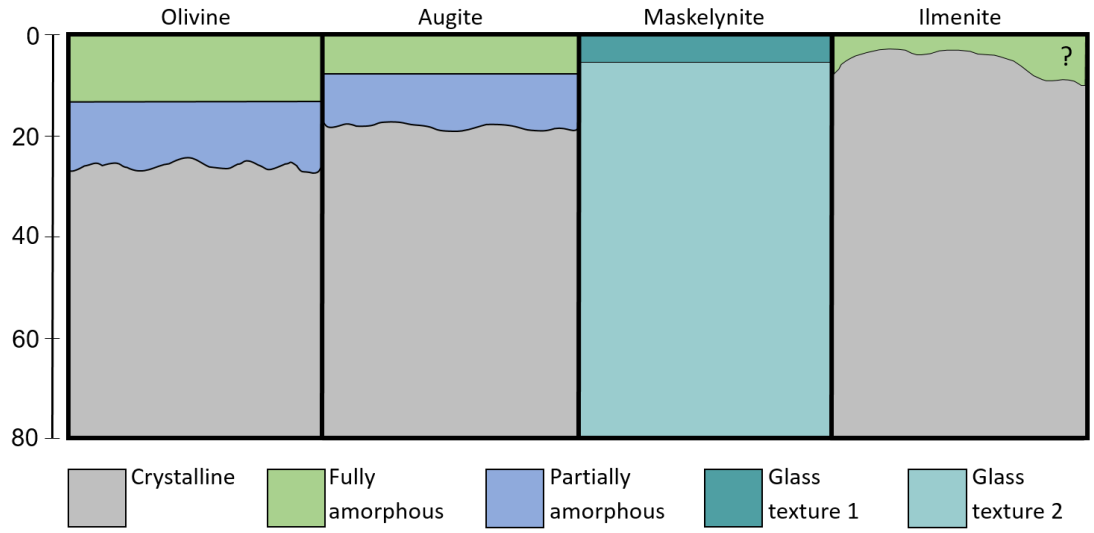

Figure 2.10. Differential Weathering Schematic. Simplified schematic of differential weathering caused by a 10-year simulation of solar wind H^+ irradiation.

2.7 References

An, Q., Zheng, L., & Luo, S. N. (2006). Vacancy-induced densification of silica glass. Journal of non-crystalline solids, 352(30-31), 3320-3325.

Bradley, J. P., & Brownlee, D. E. (1986). Cometary particles: Thin sectioning and electron beam analysis. *Science*, *231*(4745), 1542-1544.

Carrez, P., Demyk, K., Cordier, P., Gengembre, L., Grimblot, J., D'HENDECOURT, L., ... & Leroux, H. (2002). Low-energy helium ion irradiation-induced amorphization and chemical changes in olivine: Insights for silicate dust evolution in the interstellar medium. *Meteoritics & Planetary Science*, *37*(11), 1599-1614.

Caturla, M. J., de La Rubia, T. D., Marques, L. A., & Gilmer, G. H. (1996). Ion-beam processing of silicon at keV energies: A molecular-dynamics study. *Physical Review B*, *54*(23), 16683.

Christoffersen, R., & Keller, L. P. (2015, March). Solar ion processing of Itokawa grains: Constraints on surface exposure times. In *Lunar and Planetary Science Conference* (No. JSC-CN-32917).

Christoffersen, R., Keller, L. P., & Dukes, C. (2020, March). The role of solar wind ion processing in space weathering of olivine: unraveling the paradox of laboratory irradiation results compared to observations of natural samples. In *Lunar and Planetary Science Conference* (No. JSC-E-DAA-TN78282).

Cohen, M.E., S.M. Kuehner, J.H. Tepper, D.C. Burney, C.R. Neal, A.J. Irving, R.L. Korotev, and B. Hoefnagels (2019) Mineralogy and bulk composition of lunar mare basalt Northwest Africa 12008. 50th Lunar and Planetary Science Conference, abstract no. 2508.

Crider, D. H., & Vondrak, R. R. (2003). Space weathering effects on lunar cold trap deposits. *Journal of Geophysical Research: Planets*, *108*(E7).

Dhaher, N. H. (2017) Materials Science and Engineering. *CreateSpace Independent Publishing Platform*. ISBN-13: 978-1544083803.

Devine, R. A. B. (1994). Macroscopic and microscopic effects of radiation in amorphous SiO2. Nuclear Instruments and Methods in Physics Research Section B: Beam Interactions with Materials and Atoms, 91(1-4), 378-390.

Dukes, C. A., Baragiola, R. A., & McFadden, L. A. (1999). Surface modification of olivine by H+ and He+ bombardment. *Journal of Geophysical Research: Planets*, *104*(E1), 1865-1872.

Fukumi, K., Chayahara, A., Satou, M., Hayakawa, J., Hangyo, M., & Nakashima, S. I. (1990). Surface structure of ion-implanted silica glass. *Japanese journal of applied physics*, *29*(5R), 905.

Goldberg, R. D., Williams, J. S., & Elliman, R. G. (1995). Amorphization of silicon by elevated temperature ion irradiation. *Nuclear Instruments and Methods in Physics Research Section B: Beam Interactions with Materials and Atoms*, *106*(1-4), 242-247.

Hapke, B. (2001). Space weathering from Mercury to the asteroid belt. Journal of Geophysical Research: Planets, 106(E5), 10039-10073.

Harries, D., & Langenhorst, F. (2014). The mineralogy and space weathering of a regolith grain from 25143 Itokawa and the possibility of annealed solar wind damage. *Earth, Planets and Space*, *66*(1), 1-11.

Hirsch, S., Klein, H., & Jung, P. (2005). Dimensional changes of silica-, borosilicate-and germania-glasses and quartz under irradiation. *Journal of non-crystalline solids*, *351*(40-42), 3279-3288.

Jin, C., Suenaga, K., & Iijima, S. (2008). Vacancy migrations in carbon nanotubes. *Nano letters*, *8*(4), 1127-1130.

Jordan, A. P. (2021). Evidence for dielectric breakdown weathering on the Moon. Icarus, 358, 114199.

Kallio, E., Dyadechkin, S., Wurz, P., & Khodachenko, M. (2019). Space weathering on the Moon: Farside-nearside solar wind precipitation asymmetry. *Planetary and space science*, *166*, 9-22.

Keller, L. P., & McKay, D. S. (1997). The nature and origin of rims on lunar soil grains. *Geochimica et Cosmochimica Acta*, *61*(11), 2331-2341.

Keller, L. P., & Berger, E. L. (2014). *Space Weathering of Olivine in Lunar Soils: A Comparison to Itokawa Regolith Samples* (No. JSC-CN-31645).

Keller, L. P., Berger, E. L., Christoffersen, R., & Zhang, S. (2016, March). Direct determination of the space weathering rates in lunar soils and Itokawa regolith from sample analyses. In *Lunar and Planetary Science Conference* (No. JSC-CN-35490).

Keller, L. P., & Zhang, S. (2015, November). Rates of space weathering in lunar soils. In *Space weathering of airless bodies: An integration of remote sensing data, laboratory experiments and sample analysis workshop* (Vol. 1878, p. 2056).

Li, S., & Milliken, R. E. (2017). Water on the surface of the Moon as seen by the Moon Mineralogy Mapper: Distribution, abundance, and origins. *Science advances*, *3*(9), e1701471.

Li, Y., Li, X., Wang, S., Li, S., Tang, H., & Coulson, I. M. (2013). Crystal orientation results in different amorphization of olivine during solar wind implantation. *Journal of Geophysical Research: Planets*, *118*(10), 1974-1982.

Lue, C., Futaana, Y., Barabash, S., Wieser, M., Holmström, M., Bhardwaj, A., ... & Wurz, P. (2011). Strong influence of lunar crustal fields on the solar wind flow. *Geophysical Research Letters*, *38*(3).

Märk, T. D. (1994). Mechanisms and Kinetics of Electron Impact Ionization of Atoms, Molecules, and Clusters. In *Linking the Gaseous and Condensed Phases of Matter* (pp. 155-182). Springer, Boston, MA.

McFadden, J., Garrick-Bethell, I., Sim, C. K., Kim, S. S., & Hemingway, D. (2019). Iron content determines how space weathering flux variations affect lunar soils. *Icarus*, *333*, 323-342.

Pelaz, L., Marqués, L. A., Aboy, M., Barbolla, J., & Gilmer, G. H. (2003). Atomistic modeling of amorphization and recrystallization in silicon. *Applied physics letters*, *82*(13), 2038-2040.

Piao, F., Oldham, W. G., & Haller, E. E. (2000). The mechanism of radiation-induced compaction in vitreous silica. *Journal of non-crystalline solids*, *276*(1-3), 61-71.

Pieters, C. M., Taylor, L. A., Noble, S. K., Keller, L. P., Hapke, B., Morris, R. V., ... & Wentworth, S. (2000). Space weathering on airless bodies: Resolving a mystery with lunar samples. *Meteoritics & Planetary Science*, *35*(5), 1101-1107.

Poppe, A. R., Farrell, W. M., & Halekas, J. S. (2018). Formation timescales of amorphous rims on lunar grains derived from ARTEMIS observations. *Journal of Geophysical Research: Planets*, *123*(1), 37-46.

Sickafus, K. E., Kotomin, E. A., & Uberuaga, B. P. (Eds.). (2007). *Radiation effects in solids* (Vol. 235). Springer Science & Business Media.

Sim, C. K., Kim, S. S., Lucey, P. G., Garrick-Bethell, I., & Choi, Y. J. (2017). Asymmetric space weathering on lunar crater walls. *Geophysical Research Letters*, *44*(22), 11-273.

Tan, C. Z., Arndt, J., & Xie, H. S. (1998). Optical properties of densified silica glasses. *Physica B: Condensed Matter*, *252*(1-2), 28-33.

Wallace, J. B., Bayu Aji, L. B., Shao, L., & Kucheyev, S. O. (2019). Impact of pre-existing disorder on radiation defect dynamics in Si. *Scientific Reports*, *9*(1), 1-7.

Wang, L. M., & Ewing, R. C. (1992). Ion-beam-induced amorphization of complex ceramic materials—minerals. *MRS Bulletin*, *17*(5), 38-44.

Wöhler, C., Grumpe, A., Berezhnoy, A. A., & Shevchenko, V. V. (2017). Time-of-day–dependent global distribution of lunar surficial water/hydroxyl. *Science advances*, *3*(9), e1701286.

Ziegler, J. F., Ziegler, M. D., & Biersack, J. P. (2010). SRIM–The stopping and range of ions in matter (2010). *Nuclear Instruments and Methods in Physics Research Section B: Beam Interactions with Materials and Atoms*, *268*(11-12), 1818-1823.

DEEP DIELECTRIC BREAKDOWN OF SILICATES: MICROSTRUCTURAL DAMAGE AND IMPLICATIONS FOR LUNAR SPACE WEATHERING

This manuscript has been submitted to the American Astronomical Society for publishing.

3.1 Abstract

Solar energetic particle events electrically charge the lunar surface and may produce electric fields sufficient to induce dielectric breakdown in regolith grains. We irradiated series of silicate minerals with electrons to determine their physical and chemical response to deep dielectric charging and subsequent breakdown. Two electrical phenomena produced damage: erosional and eruptive channels, surface pits, comminuted grains, and melt and vapor deposits. Iron abundance strongly affected the scale of damage and the minimum fluence required to reach dielectric breakdown. If dielectric breakdown is a prominent space weathering process on the Moon, it should contribute to differential weathering signatures across the lunar surface as a function of target composition.

3.2 Introduction

Dielectric breakdown caused by solar energetic particle (SEP)-induced internal charging is theorized to occur in minerals on the lunar surface and other airless bodies in the Solar System (for a review, see Jordan (2022)). The resulting mineral damage may significantly contribute to regolith space weathering and thus play an important role in optical maturation (Jordan, 2021; Jordan et al., 2017; Lemelle et al., 2003). Although

dielectric breakdown has been well documented as the source of anomalies in insulating spacecraft components (Frederickson et al., 1992; Green and Frederickson, 2006), its microstructural and chemical effects in lunar-relevant materials have not been experimentally investigated, except in a limited study by Lemelle et al. (2003). Here, we present the results of experimentally irradiated minerals that have undergone dielectric breakdown by deep dielectric charging. We characterize the resulting damage as a function of mineralogical variation and identify diagnostic features that can be used for the identification of dielectric breakdown weathering in extraterrestrial samples.

3.2.1 Background

Minerals at the surfaces of airless bodies are exposed to micrometeoroids and to charged particles with energies ranging from hundreds of eV to several GeV. A subset of these incident populations--namely micrometeoroids and the solar wind (energies <10 keV)--are thought to cause most space weathering damage, including amorphous rims, metallic iron nanoparticles, and vapor and melt deposits (see reviews by Pieters and Noble, 2016; Hapke, 2001). However, a key question that remains unanswered is how individual particle populations, with different energy fluxes, contribute to overall space weathering. Specifically, it is unclear whether high energy particles with low energy fluxes optically alter the surface. Considering effects of the full range of incident particle energies can help us better constrain the contribution of each population to overall space weathering.

Charged particles incident to the Moon are separated into three main categories based on energy and source: solar wind (~1 keV), SEPs (~50 keV to ~10 GeV), and

galactic cosmic rays (GCRs) (peak at ~200 MeV); we ignore the magnetotail population, which dominates at energies < ~100 eV (Poppe et al., 2018). The more energetic populations penetrate deeper into the regolith, with the solar wind penetrating 10s of nm, SEPs penetrating to ~1 mm, and GCRs penetrating ~1 m. The solar wind and GCRs continuously shower the lunar surface, while SEPs are episodically accelerated by solar flares and coronal mass ejections. Jordan et al. (2014) hypothesized that SEP deposition may sufficiently charge the lunar surface to cause dielectric breakdown and permanent alteration to insulating regolith grains. However, dielectric breakdown (herein referred to as "breakdown") of lunar regolith has not been experimentally studied and the possible contribution of this phenomenon to optical maturation is currently estimated only by theory (Jordan et al., 2015, 2017, 2019; Jordan, 2021, 2022).

3.2.2 Deep Dielectric Charging and Breakdown

Deep dielectric charging is the process by which an electric field forms within an electrically insulating material as charged particles are implanted to a depth (Fig. 3.1). Hyper-localized polarization can occur because charged particles within a dielectric have very limited mobility; the charge may remain trapped for seconds to weeks (Jordan et al., 2014), depending on the dielectric properties of the material and thermal environment. The rate at which this charge dissipates is called the discharging timescale. When particle fluence exceeds the discharging timescale, the electric field increases in strength and can overcome the dielectric strength of the material, subsequently causing breakdown. Most dielectrics undergo breakdown with exposure to electric fields of ~10^6-10^7 V m^{-1}

(Budenstein, 1980) or a minimum fluence of ~10^{10}-10^{11} particles cm^{-2} (Garrett and Evans, 2001; Green and Dennison, 2008) deposited within the discharging timescale.

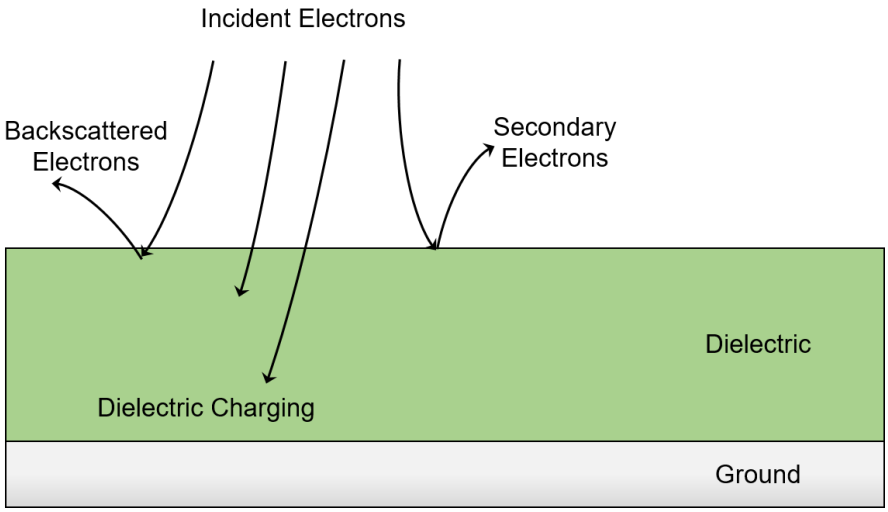

Figure. 3.1. Dielectric Charging. The accumulation of charged particles implanted in dielectric materials such as lunar regolith can create strong internal electric fields.

A combination of material properties, environmental factors, and particle depositional behavior may create strong electric fields within the regolith. Solar electrons have energies of 1 keV – 10 MeV and solar ions have energies of 30 keV – 10 GeV (McGuire and Rosenvinge, 1984), leading to penetration depths of about 0.06 - 3.6 mm for electrons and 0.03 - 1.2 mm for ions (Hapke, 2022). Both populations have similar energies, but the electrons have much less mass, so they often reach the surface before protons. Also, the difference in their penetration depths may create charge separation within insulating grains and lead to strong localized electric fields then subsequently, dielectric breakdown.

Although SEP events typically last 4-6 days, they deposit the majority of particles within the first two days (Jordan et al., 2014, 2019). Low regolith conductivities and long discharge timescales (3-20 days) on the nightside and in regions of permanent shadow

result in charge that accumulates faster than it can be dissipated. Theoretical models predict that deep dielectric charging and breakdown affect up to 25% of grains in the top 1 mm of regolith -- equivalent to the contribution of micrometeoroid impacts to optical maturation (Jordan et al., 2017, 2019). Experimental work has shown that 30 keV electrons, which comprise low-energy SEPs, are capable of causing breakdown in olivine (Lemelle et al., 2003; Shusterman et al., 2021). Hapke (2022) argued that breakdown cannot occur because secondary electron production by SEPs will facilitate charge neutralization, however, this work assumes a secondary yield that is approximately an order of magnitude too high for SEP energies (e.g., Halekas et al., 2009) and should thus be revisited.

Dielectric breakdown is a highly energetic process that results in the permanent deformation or destruction of insulating materials. The breakdown process begins with deep dielectric charging, during which charged particles are injected into a material from an external source. The initiation of breakdown occurs where electric fields are sufficiently strong to overcome the dielectric strength of a material. Depending on particle penetration depth, field concentrations can form within the dielectric volume and at the vacuum-surface interface. Localized molecular bond disruption occurs where the electric field is strongest, such as regions of disorder, surface imperfections, and grain boundaries. There, once the dielectric strength is overcome, a conducting pathway forms to dissipate excess charge. Charge escapes along an ionized channel where plasma is created as dielectric material is vaporized (Budenstein, 1980). The incorporation of material during Joule heating acts as a catalyst for the propagation of primary and secondary channels (Budenstein, 1980), which occurs on the order of tens of

nanoseconds. In certain charging geometries, breakdown may also occur along the surface rather than through the volume of the dielectric. This phenomenon is called a "flashover". The formation mechanism of flashovers is similar to discharges in the subsurface, but its initiation may require gas desorption (Miller, 2015).

Dielectric breakdown weathering is expected to produce measurable changes in optical maturity of lunar grains within the top 1 mm of regolith. Models predict the dielectric breakdown contribution to overall weathering should be comparable to the effects of micrometeoroid bombardment (Jordan et al., 2017, 2019, 2021). The positive correlation between conductivity and temperature suggests there should be latitudinal trends in optical maturation where breakdown frequency increases with increasing latitude (Jordan et al., 2019; Jordan, 2021), and is especially prevalent in permanently shadowed regions (PSRs) (Jordan et al., 2015). Furthermore, east-west weathering asymmetries on crater walls have been correlated to decreased SEP fluxes during the Moon's traverse through Earth's magnetotail (Jordan et al., 2022).

Experimental investigations into the effects of dielectric breakdown in silicates have primarily focused on fluid-assisted, high-voltage pulses to liberate economically valuable grains with terrestrial resource potential (e.g., Andres et al., 1986; Fujita et al., 2001). Lemelle et al. (2003) were the first to compare the effects of dielectric breakdown by charge implantation in iron-poor and iron-rich single crystals of olivine. The structural damage they observed, primarily melt sephrules and micrometer-sized holes on sample surfaces, led to the hypothesis that breakdown could significantly contribute to space weathering of interplanetary dust particles and regoliths on airless bodies. This study describes the microstructural and chemical effects of breakdown caused by electron

irradiation of lunar-relevant silicates with a range of iron abundances. Electron microscope analysis revealed two electrical phenomena, surface and subsurface discharging, which produced microstructural and chemical damage likely to affect the optical signatures of grains.

3.3 Materials and Methods

3.3.1 Sample Preparation and Characterization

We characterized the effects of dielectric breakdown in four gem-quality, single-crystal silicates including an olivine ($Fo_{74}Fa_{26}$), San Carlos olivine ($Fo_{90}Fa_{10}$), diopside ($Wo_{50}En_{48}Fs_{2}$), and labradorite ($An_{60}Ab_{40}$) to characterize the effects of surface and subsurface breakdown as a function of chemical composition. To prepare the samples for irradiation, a section from each mineral was cut to a thickness of 1 mm using a wire saw. We hand polished each section to a roughness of 1 μm using aluminum oxide lapping film lubricated with deionized water; we avoided a perfect polish because lunar grains have highly irregular surfaces and these irregularities can strengthen electric fields. After polishing, a 1x1 mm^2 grid was etched into the experimental surface using a wire saw lubricated with deionized water. These grid squares marked locations of individual experimental runs and served to isolate the effects of discharging. Even slight organic contamination introduced during sample preparation and handling can provide a sufficient conducting pathway for accumulating charge to dissipate, so sections were cleaned in a sequence of ultrasonic baths: 99% isopropyl alcohol, 5% Micro-90 cleaning solution, 1% Micro-90 cleaning solution, and then deionized water. Samples were not

baked out, but experiments were performed at high vacuum pressures sufficient to drive off adsorbed water (~10^{-6} torr).

Major and minor elemental abundances were measured using a JEOL JXA-8530F electron microprobe. The microprobe was operated using an accelerating voltage of 15 kV and a beam current of 20 nA. The beam diameter was ~10 nm. Minerals used as standards included natural hornblende, San Carlos olivine, San Carlos augite, and hypersthene. Ten measurements acquired from randomized locations on each section were averaged to give the oxide abundances in Table 3.1.

Table 3.1. Sample Oxide Abundances. Averaged oxide abundances for olivine (Ol-Fo_{74}), San Carlos olivine (Ol-Fo_{90}), diopside (Dio), and labradorite (Lab). Electron microprobe limits were accurate to the 99% confidence interval.

Ox. Abund. (Wt%)	SiO_2	Al_2O_3	FeO	MgO	MnO	CaO	Na_2O	K_2O	TiO_2	Cr_2O_3	Total	
Ol-Fo74	37.84	0.04	23.35	37.68	0.3	0.16	0.01	0.01	0.02	-0.01	99.4	
Ol-Fo90	40.4	0.02	9.59	48.22	0.11	0.1	0.00	0.01	0.01	0.02	98.48	
Dio	54.92	0.22	1.08	17.41	0.04	25.01	0.34	0.02	0.08	0.67	99.79	
Lab	52.69	29.92	0.37	0.09	0.01	12.11	4.43	0.27	0.06	0.00	99.95	
At. Abund. (%)	Si	Ti	Al	Cr	Fe	Mn	Mg	Ca	Na	K	O	Total
Ol-Fo74	14.23	0.01	0.02	0.00	7.34	0.09	21.12	0.06	0.01	0.01	57.12	100.00
Ol-Fo90	14.35	0.00	0.01	0.01	2.85	0.03	25.53	0.04	0.00	0.00	57.18	100.00
Dio	19.95	0.02	0.10	0.19	0.33	0.01	9.43	9.73	0.24	0.01	59.99	100.00
Lab	18.38	0.02	12.30	0.00	0.11	0.00	0.05	4.53	3.00	0.12	61.50	100.00

3.3.2 Sample Irradiation

Electron irradiation was conducted in an FEI NOVA 200 NanoLab Field Emission Scanning Electron Microscope (FE-SEM). Although deep dielectric charging in lunar regolith grains may sometimes occur as a function of the differential penetration depths of protons and electrons, internal electric fields are often generated by either protons or electrons alone (Jordan et al., 2019). Electrons were selected for this study to

expand on the techniques of Lemelle et al. (2003), who were some of the first to report on the possible importance of breakdown weathering on the Moon.

Cleaned and uncoated mineral sections were mounted in the FE-SEM using a copper clip located opposite of the gridded experimental area. To minimize unintentional beam damage, we over-focused the beam such that its diameter was ~11.2 μm at the sample surface. The accelerating voltage of the electron beam was 30 keV for all experimental runs, giving a maximum electron range of ~5.5 μm (Demers et al., 2011). Parameters including beam current (21-2400 pA), scan area (5.66×10^4 μm^2 or 4.60×10^3 μm^2), and scan duration (60-600 sec) were adjusted to control the total fluence supplied during each run (see Table 2 for a detailed list of parameters). The beam flux was calculated from the beam current, scan duration, and rastered area. Total fluences reported herein refer to the total calculated time integrated flux, not the actual dose received. WE used secondary electron imaging to monitor charging and discharging behaviors, and we used an ammeter beneath the samples to record abrupt changes in current.

Table 3.2. Experimental parameters and outcomes for each run in labradorite (Lab), diopside (Dio), San Carlos olivine (Ol-Fo_{90}), and olivine (Ol-Fo_{74}). The accelerating voltage was held constant at 30 kV for all runs.

Run	Material	Breakdown Event (Y/N)	Current (pA)	Experimental Duration (s)	Flux ($e^- cm^{-2} s^{-1}$)	Fluence ($e^- cm^{-2}$)	Scan Area (μm^2)
1	Lab	N	21	60	2.32E+11	1.39E+13	5.66E+04
2	Lab	N	21	300	2.32E+11	6.96E+13	5.66E+04
3	Lab	N	21	600	2.32E+11	1.40E+14	5.66E+04
4	Lab	Y	44	60	4.85E+11	2.91E+13	5.66E+04
5	Lab	Y	44	300	4.85E+11	1.46E+14	5.66E+04
6	Lab	Y	44	300	5.97E+12	1.79E+15	4.60E+03
7	Dio	N	21	60	2.32E+11	1.39E+13	5.66E+04
8	Dio	N	21	300	2.32E+11	6.96E+13	5.66E+04
9	Dio	N	21	600	2.32E+11	1.40E+14	5.66E+04
10	Dio	Y	44	300	4.85E+11	1.79E+15	4.60E+03
11	Dio	Y	44	300	4.85E+11	1.46E+14	5.66E+04
12	Dio	Y	150	300	1.65E+12	4.95E+14	5.66E+04
13	Dio	Y	2400	300	2.65E+13	7.95E+15	5.66E+04
14	Ol-Fo_{90}	N	21	60	2.32E+11	1.39E+13	5.66E+04
15	Ol-Fo_{90}	N	21	300	2.32E+11	6.96E+13	5.66E+04
16	Ol-Fo_{90}	N	21	600	2.32E+11	1.40E+14	5.66E+04
17	Ol-Fo_{90}	N	44	300	4.85E+11	1.46E+14	5.66E+04
18	Ol-Fo_{90}	Y	44	300	5.97E+12	1.79E+15	4.60E+03
19	Ol-Fo_{90}	N	150	300	1.65E+12	4.95E+14	5.66E+04
20	Ol-Fo_{74}	N	21	60	2.32E+11	1.39E+13	5.66E+04
21	Ol-Fo_{74}	N	21	300	2.32E+11	6.96E+13	5.66E+04
22	Ol-Fo_{74}	N	21	600	2.32E+11	1.40E+14	5.66E+04
23	Ol-Fo_{74}	N	21	140	2.85E+12	3.99E+14	4.60E+03
24	Ol-Fo_{74}	N	150	165	2.03E+13	3.35E+15	4.60E+03
25	Ol-Fo_{74}	N	2400	300	2.65E+13	7.95E+15	5.66E+04

3.3.3 SEM and TEM Imaging

Post-irradiation, we coated each section with ~20 nm of evaporated carbon to prevent further charging during electron microscopy analyses. We then collected secondary electron (SE) images of surface damage using a ThermoScientific Helios 5UX FE-SEM/FIB (focused ion beam). The images were acquired using a Through the Lens detector (TLD) with immersion lens, an accelerating voltage of 2 kV, and a working distance of 4 mm. FIB sections of diopside and labradorite were prepared for transmission electron microscope (TEM) imaging using the Helios 5UX. No FIB sections of Ol-Fo_{90} or Ol-Fo_{74} were prepared because neither sample had any surface damage,

which was used to locate probable subsurface damage. Regions of interest were coated with a thin tungsten strap (~20 nm) and a thick, protective carbon strap (~3 µm). Initial thinning of the section to ~200 nm was done using 30 kV Ga^+ ions. Surface damage was removed and electron transparency thickness (~120 nm) was reached with the use of 5 kV and 2 kV Ga^+ ions.

TEM imaging was performed using an aberration-corrected FEI Titan 300/80 located at the Eyring Materials Center at Arizona State University. To minimize beam damage to the samples, we operated the microscope at 300 kV. Energy dispersive X-ray spectroscopy (EDS) was used to acquire compositional data from damaged and undamaged regions within the TEM sections.

3.3.4 Supplementary Olivine Experiment

A supplementary set of experiments were performed on San Carlos olivine (herein referred to as Ol-Fo_{90}-2) using a much higher fluence than experiments outlined in Table 2. The purpose of these experiments was to initiate enough subsurface discharges to easily locate and characterize the resulting features with TEM. To prepare this sample for irradiation, we cut a section measuring ~5x5 mm^2 with a thickness of 1.5 mm. The experimental surface was hand polished using a series of alumina suspensions (5.0 µm, 1.0 µm, and 0.05 µm) and polishing cloths. To prevent surface contamination from interfering with charging, the section was cleaned using the methods described in §2.1.

After cleaning, half of the sample was coated with ~20 nm of vapor-deposited carbon. The carbon-coated side of the section was secured to an aluminum stub with a

copper clip, then mounted into an FEI XL30 FE-SEM. Once the chamber reached a pressure of ~$7x10^{-6}$ torr, the electron beam (V=30 kV and i=39 nA; flux =$1.9x10^{15}$ particles cm^{-2} s^{-1}) was rastered over an area of $1.08x10^4$ μm^2 to supply a total fluence of $3.1x10^{17}$ particles cm^{-2}. We monitored surface charging and discharging behavior in real-time using secondary electron imaging.

After irradiation, samples were coated with ~20 nm of evaporated carbon. Secondary electron images of surface damage were collected using the FEI XL30 FE-SEM, then we prepared FIB sections using the methods described in §2.3. TEM imaging of subsurface damage was performed on a Philips CM200-FEG.

3.4 Results

Labradorite, diopside, and San Carlos olivine (Ol-Fo_{90}) were modified to varying degrees by electrical discharging from low-fluence, 30-kV electron irradiation. The Ol-Fo_{74} section was the only sample that did not discharge under the maximum supplied fluence in these experiments. In the samples that did discharge, two independent electrical phenomena were detected: flashovers and subsurface discharges. Each phenomenon produced plasma channels bound within the dielectric volume, liberated from the subsurface to the surface-vacuum interface, or propagated laterally along mineral surfaces. The location of electrical discharge nucleation and the physical characteristics of the dielectric (e.g., grain size, existing defects, and grain orientation) were the primary controls on channel characteristics. Volume and surface defects resulting from these discharges included melt-filled channels, lattice strain in the

subsurface, and vapor and melt deposits at the surface. These distinct signatures may be useful for identifying breakdown effects in extraterrestrial samples.

3.4.1 Flashovers

Flashover events in our lower-fluence experiments were detected in real time by monitoring current collected from the sample holder (Fig. 3.2) and watching for an abrupt disturbance in the production of secondary electrons (Fig. 3.3). Flashovers occur as a result of excessive surface charging. Consequently, the principal damage is the formation of "tree" structures: primary and secondary filamentous channels that propagate along the surface with fractal geometries (Fig. 3.4). Maximum channel widths were ~180 nm, and maximum channel lengths were ~90 µm. Minimum channel lengths or widths are not reported due to the fractal geometries , but secondary channels were either enlarged at the termini due to Joule heating, or they tapered to a width of <10 nm (Fig. 3.5).

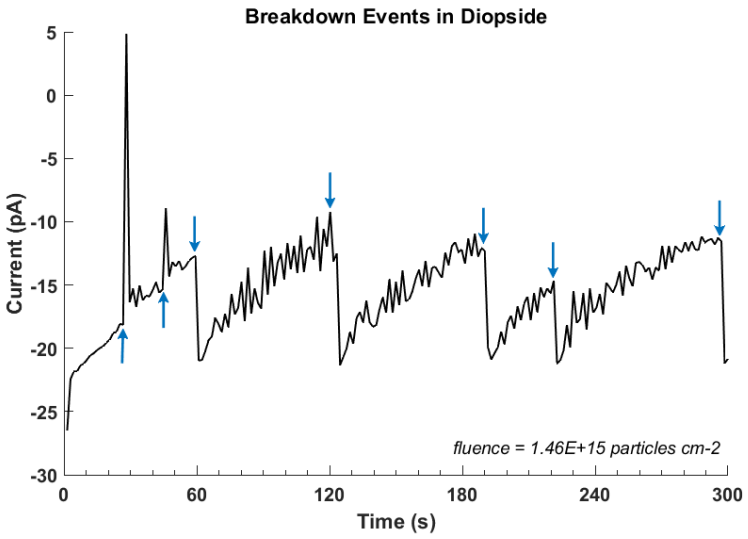

Figure 3.2. Current Measurement for Diopside. Current readout acquired from beneath the samples during active irradiation. Peaks and troughs in the data are interpreted as flashover events and subsurface discharges, respectively. Note that "peaks" are negative in this case because irradiation was conducted using electrons. Blue arrows indicate the approximate time of discharge and correspond to saturated SE line scans shown in Fig. 3.3.

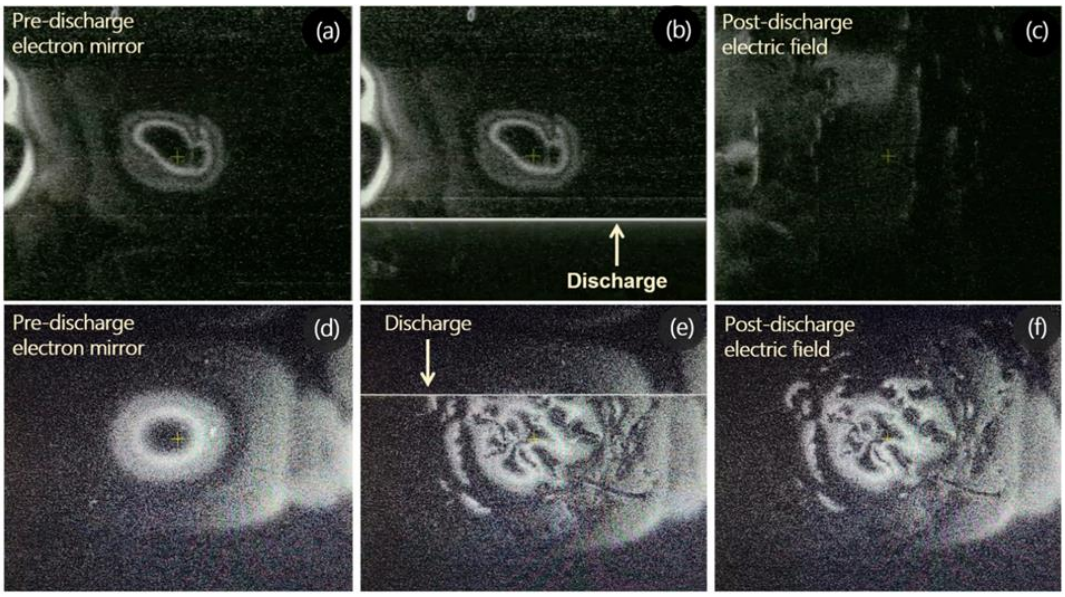

Figure 3.3. Breakdown in Secondary Electrons. A time-sequence of secondary electron (SE) images acquired during irradiation of diopside (a-c) and labradorite (d-f). As the sample surface charged, a weak electron mirror formed (a,d). Discharge produced one or more SE-saturated scan lines (b,e). The electron mirror and surface field were immediately disrupted by the discharge event (c,f).

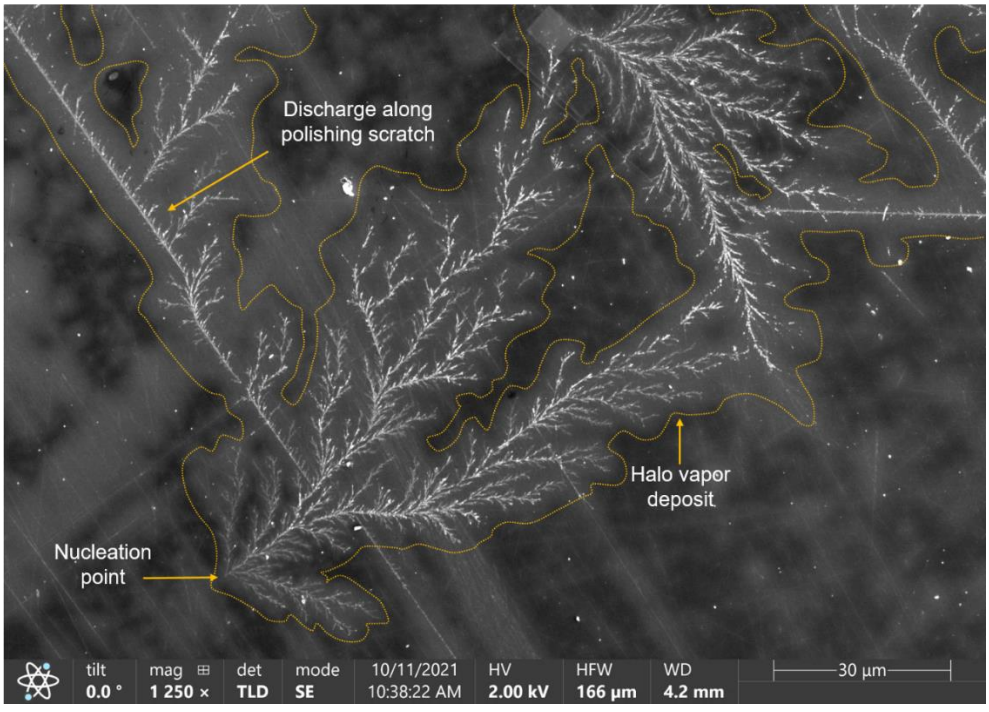

Figure 3.4. Flashovers. Secondary electron image of several flashover discharge features on labradorite. The bright linear channel running northwest to southeast preferentially travelled along a polishing scratch. Note the bright halo vapor deposition surrounding flashover channels (outlined in orange).

The topology of flashovers diverged from fractal geometries where discharge was initiated at, or intersected with, preexisting surface scratches. Scratches in these cases acted as highly efficient conduits and were found to form much longer primary channels than those formed in pristine surfaces. The high pressure and temperature of ionization caused material in contact with the plasma to sublimate and melt, leaving behind amorphized material extending to depths ~150% deeper than the depths of channels themselves (Fig. 3.6). Much of this material was redeposited as thin, amorphous deposits and as melt spherules (<300 nm diameter). The diameter of melt spherules was closely correlated to the width of channels they lined – except at termini, where otherwise large, directional melt deposits formed.

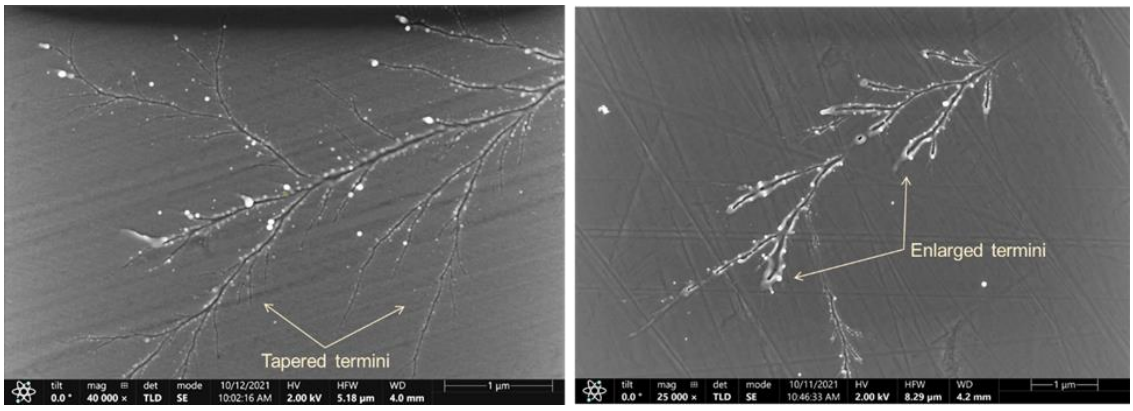

Figure 3.5. Flashover Termini. Tapered termini of flashover channels on diopside. (Right) enlarged termini of flashover channels in labradorite. Tapered and enlarged termini were found in all minerals affected by flashovers

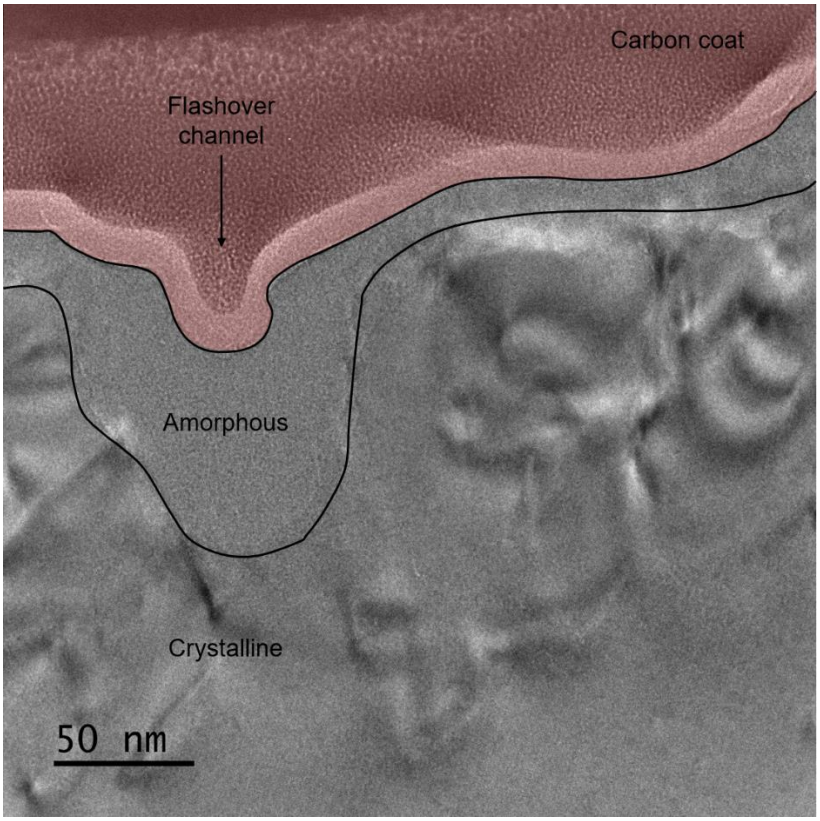

Figure 3.6. Flashover Cross-section in San Carlos Olivine. Amorphous material extends ~150% deeper than the residual erosional channel exposed at the surface.

In one case, a flashover travelled along a grain boundary between labradorite and a surface-exposed inclusion. The force of the expanding plasma appears to have ejected and disintegrated the inclusion. Fragments of the inclusion were deposited in the same direction as the plasma propagation at a minimum distance of ~10 µm from the original location of the inclusion (Fig. 3.7).

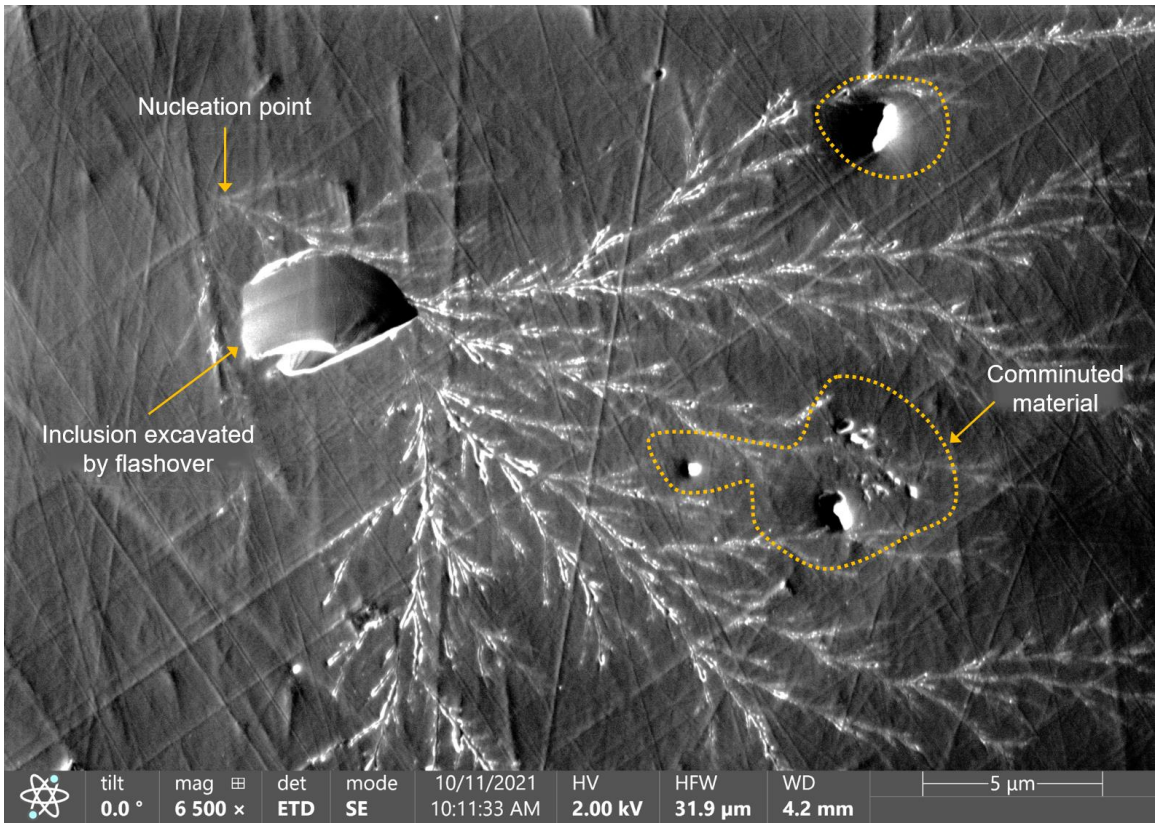

Figure 3.7. Excavated inclusion. A flashover intersecting an inclusion in labradorite ejected and disintegrated the inclusion. The comminuted grain was deposited in the direction of plasma propagation.

The supplementary olivine experiment, in which higher electron fluences were supplied, resulted in areally dense surface damage compared to lower fluence experiments (Fig. 3.7). Discharges were identified by several saturated line scans in SE images in lower flux experiments, but the SE detector was saturated during high flux experiments in Ol-Fo_{90}-2, beginning within one second of exposure. Flashovers were so numerous that the original surface was fully covered with erosional channels and melt deposits (Fig. 3.8). Channels were primarily constrained to the scanned region, but a minority fraction propagated to distances <30 µm outside the irradiation boundary. While these channels extending beyond the boundary had fractal geometries, the channels

within the boundary predominantly bore in the same direction in which the electron beam rastered.

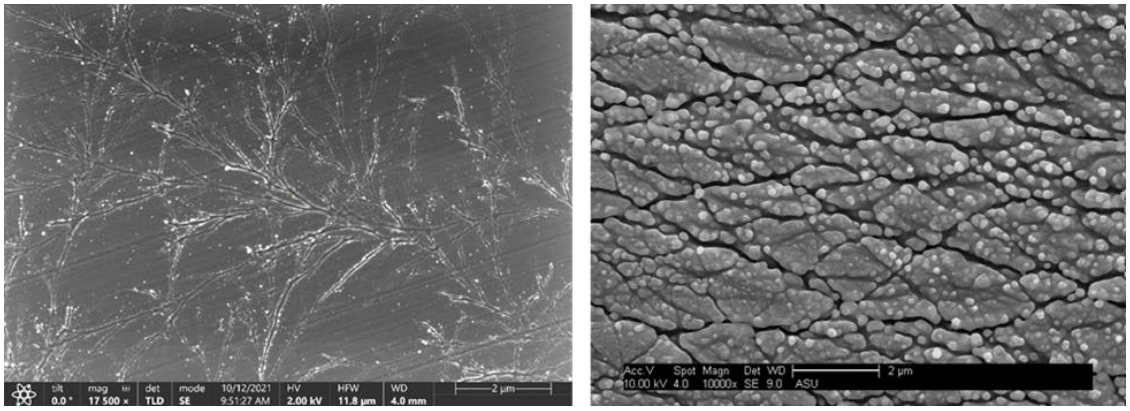

Figure 3.8. Effects of Fluence on Flashover Density. Two images that show the effect of increasing fluence on surface damage. (Left) Dispersed flashover channels formed in diopside after receiving a fluence of $1.5x10^{15}$ electrons cm^{-2}. (Right) A dense flashover network and thick melt deposits formed on San Carlos olivine (Ol-Fo_{90}-2) after receiving a fluence of $3.1x10^{17}$ electrons cm^{-2}, two orders of magnitude greater fluence than the diopside.

3.4.2 Subsurface discharging

A sudden spike in current and an abrupt saturation of a single or several sequential line scans in the secondary electron detector signaled subsurface discharge events. Subsurface discharges occur due to deep dielectric charging and exhibit different characteristics than flashovers at the sample surface. The shape and size of subsurface channels are constrained by the amount of energy released, electrical properties of the mineral, the presence of preexisting lattice defects and inclusions, and the proximity of the discharge to the sample surface. While subsurface discharges were detected in labradorite, diopside, and Ol-Fo_{90}, results from the high-fluence Ol-Fo_{90}-2 experiment are presented because it contained sufficiently dense subsurface discharges to locate damage post-irradiation.

Like flashovers, breakdown channels in the subsurface were formed by ionization and plasma propagation. Although TEM images do not provide a 3-dimensional view of subsurface channels, they appeared to be composed of single, non-branching channels that preferentially propagated along crystallographic planes (Fig. 3.9). Because the electrical conductivity of a single crystal is anisotropic, the subsurface breakdown pathway may tend to follow crystallographic planes rather than propagating with fractal geometries seen with flashovers.

The length of subsurface channels ranged from 100s of nm to >3 μm. Their widths were variable, but typically less than 300 nm at their widest points. The force of plasma expansion and heating produced lattice strain around the channels, especially at the termini. The centers were filled with amorphous material with a composition indistinguishable from the parent material.

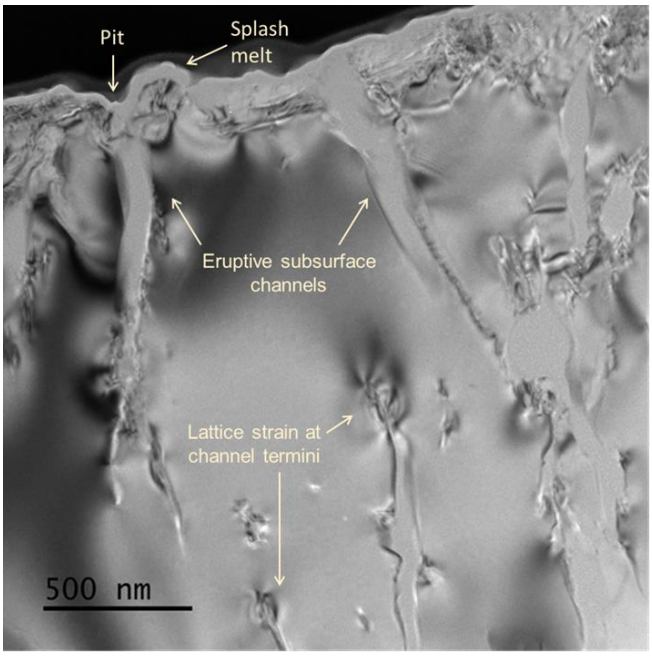

Figure 3.9. Subsurface Breakdown Damage. Bright field TEM image of San Carlos olivine (Ol-Fo_{90}-2). Smooth, linear features are subsurface breakdown channels filled with amorphous melt. Some channels that nucleate at depth breach the vacuum-surface threshold. The surface is comprised of a melt and vapor deposition layer formed by both erupting channels and flashovers.

Subsurface discharges also contributed to surface vapor and melt deposits (Fig. 3.10). Some discharges occurring within 2.5 µm of the surface breached the surface-vacuum threshold. In these cases, eruptive channels produced pits with diameters >80 nm (Fig. 3.11). Pits >100 nm were typically surrounded by melt ejecta, while pits <100 nm did not typically produce melt deposits that were traceable to the erupting channel.

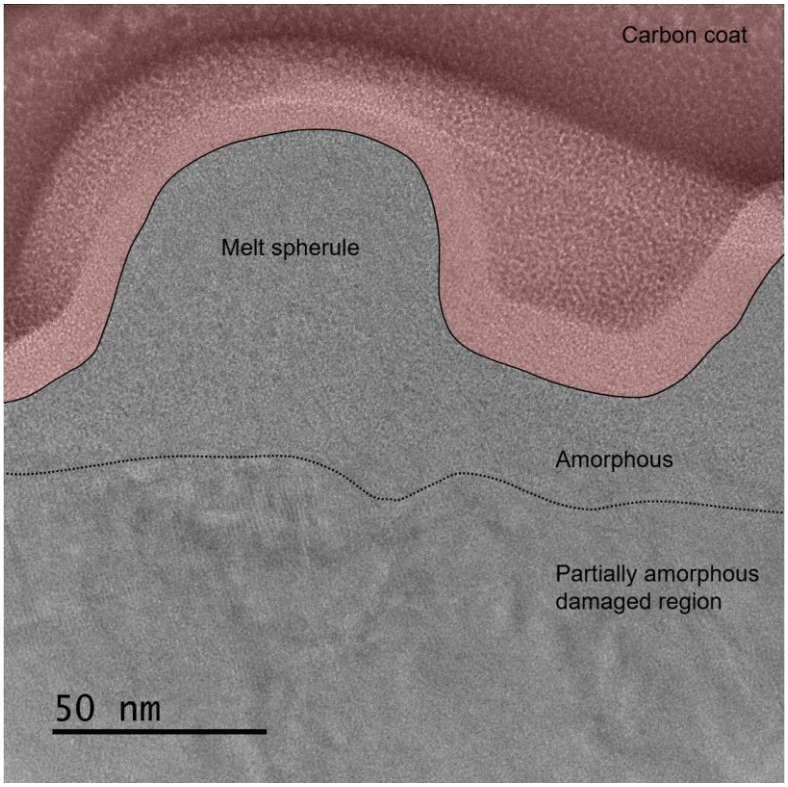

Figure 3.10. Amorphous Rim and Melt Spherule. TEM bright field image of a melt spherule on San Carlos olivine (Ol-Fo90-2). A narrow layer of melt deposited contemporaneously with the melt spherule, overlaid partially amorphous material. The area shaded in red is a protective carbon coating deposited to prevent damage to the surface during FIB preparation.

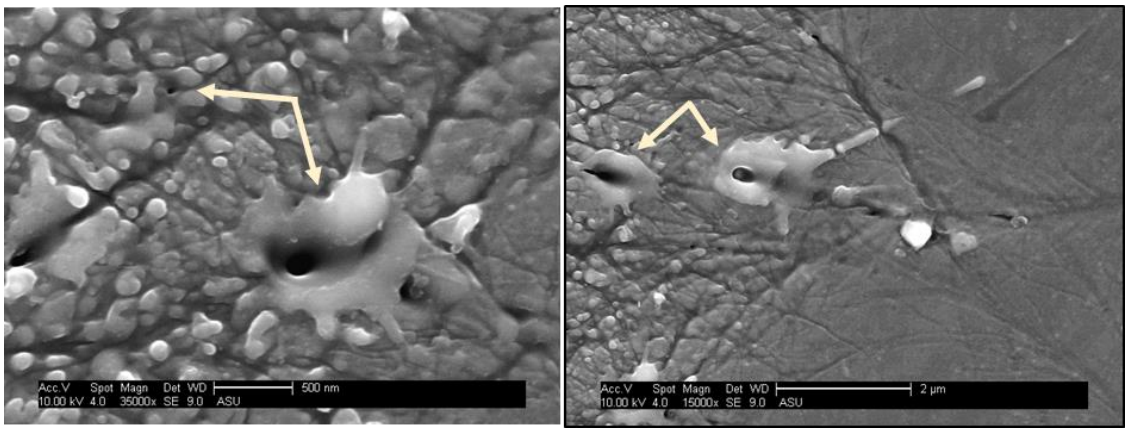

Figure 3.11. Eruptive Pits. Secondary electron images of eruptive channel pits surrounded by melt in San Carlos olivine (Ol-Fo_{90}-2). Melt deposits were Si-enriched.

3.4.3 Effects of compositional variation

Our samples covered a range of iron abundances <25 wt% FeO. We found a strong, positive correlation between iron abundance (wt% FeO) and the minimum fluence required to initiate deep breakdown for silicates containing <25 wt% FeO (Fig. 3.12). The minimum fluence required for flashovers was approximately one order of magnitude lower than that for subsurface discharge, but still positively correlated with iron abundance. For samples that underwent breakdown, the correlation between iron abundance and minimum fluence was roughly linear (although additional data points would improve the understanding of this relationship). We found materials with <10 wt% FeO to be susceptible to small changes in particle fluence (first subsurface discharges occurred at fluences between 2.15×10^{13} particles cm^{-2} for labradorite and 1.86×10^{14} particles cm^{-2} for Ol-Fo_{90}).

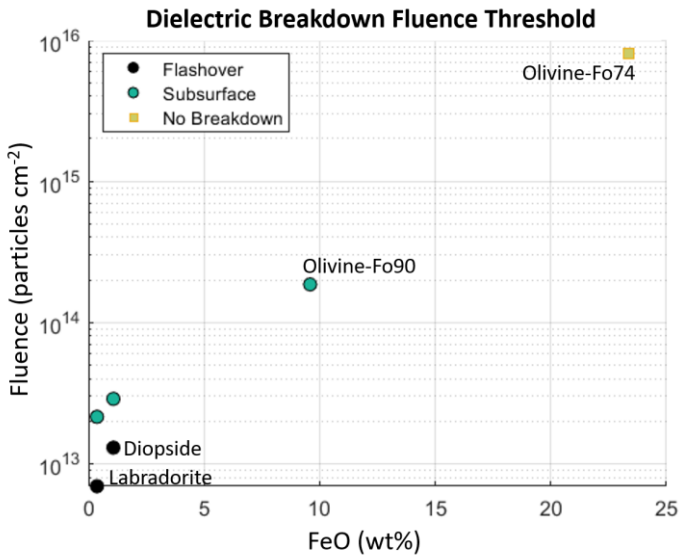

Figure 3.12. Breakdown Fluence Threshold. (Left) This log-linear plot shows the minimum fluence required to initiate breakdown in Byt, Dio and, Ol-Fo_{90}. The yellow marker represents the maximum fluence supplied to Ol-Fo_{74}, but does not represent a breakdown threshold. (Right) The minimum fluence required for subsurface discharging is approximately linear for materials with iron abundances less than 10 wt% FeO.

Although minerals containing lower iron abundances required less incident charge to induce breakdown, diopside sustained significantly more surface damage than labradorite. We only supplied enough fluence to discharge the Ol-Fo_{90} one time during low-fluence experiments, but the surface damage produced in Ol-Fo_{90}-2 during high-fluence experiments indicates it likely would have incurred more surface damage than diopside and significantly more than labradorite.

3.5 Discussion

Four silicate minerals were subjected to electron irradiation to initiate deep dielectric breakdown. These experiments aimed to characterize damage produced by breakdown as it may pertain to space weathering of the lunar regolith. Two electrical phenomena, subsurface discharges and flashovers, were found to occur independently

and produce unique damage types. The types of damage were consistent among all mineral phases for fluences sufficient to cause breakdown, but the areal density of damage changed as a function of both fluence and material properties.

3.5.1 Deep dielectric breakdown

The primary damage features produced by subsurface discharges were channels filled with quenched, amorphous melt. These channels appeared to be approximately oriented along crystallographic planes and vary in shape and size. Despite the use of a single-energy electron beam to irradiate the targets, there was no depth within the stopping range of 30 keV electrons at which discharge nucleation preferentially occurred, suggesting the implanted charge is highly mobile at room temperature and that strong electric fields are hyper-localized. In other words, a single-energy beam does not create a discrete charge layer but instead creates strong electric fields throughout the stopping range of incident particles. The size and shape of subsurface channels are likely controlled by a complex function of target electrical properties and crystal structure. However, it is beyond the scope of this study to determine those parameters.

Many, but not all, subsurface discharges terminated before escaping to the surface-vacuum threshold. Those that did breach the surface, produced Si-enriched melt deposits and broad regions of vapor deposition. They also produced nm-scale craters, many of which were surrounded by melt deposits. We did not find metallic iron particles within melt or vapor deposits. However, because the melt was Fe-depleted, even in the most iron-rich sample, we presume the vapor deposits were Fe-enriched. This suggests that breakdown, if it occurs on the Moon, might contribute to optically significant vapor-

deposited rims that are rich in nanophase iron (e.g., Hapke, 2001; Keller and McKay, 1997). Because the scanned areas were so small ($3.55x10^4$ μm^2), we did not acquire spectral data to determine to what extent the melt and vapor deposits alter the optical properties of the surface.

3.5.2 Flashovers

The primary flashover damage type was erosional surface channels exhibiting fractal geometries. In general, flashover trees were initiated from the edge of the irradiated regions and propagated toward the center, especially for experimental runs receiving lower particle fluences. The electric field in this geometry is strongest at the edge of the scanned region and diminishes to approximately zero at the center (Sutjipto and Takata, 2007). In this regard, the edge of the scanned region can be considered positively charged and the center negatively charged, eliminating the need for a true cathode-anode interaction to generate the electron cascade that begins a flashover event.

Unlike subsurface discharges, which do not appear to travel along the same pathway more than once, flashovers can nucleate in, and travel along, preexisting surface channels or fractures. Nucleation points are most likely to occur at surface imperfections such as scratches or pits, and the irregular topography left by the erosional process of plasma propagation subsequently generates enhanced electric fields. Because these localized discharges do not completely destroy dielectric properties of the sample, discharge events can recur as long as sufficient incident particle fluence is supplied. Discharges along preexisting pathways bore deeper into the surface, creating deeper channels and more abundant melt and vapor deposits.

Although surface defects can produce enhanced electric fields, they can also reduce the likelihood of flashovers. Because secondary electron emission avalanches serve as the nucleation mechanism of flashovers, the inhibition or prevention of flashovers on rough lunar grains may result from decreased secondary electron yields and decreased surface charge accumulation (Guo et al., 2019). We used diopside to test the effects of surface roughness on the frequency of flashovers. The minimum fluence required to initiate flashovers on polished areas of diopside was $1.3x10^{13}$ electrons cm^{-2}. In contrast, the roughened surface experienced no flashovers, even at fluences up to two orders of magnitude greater than that required to breakdown the polished area ($1.5x10^{15}$ electrons cm^{-2}). Additional studies using unpolished sections or granular samples would help constrain the effects of surface roughness on flashover effects.

3.5.3 The role of electrical conductivity

Understanding how plasma interactions alter grains during SEP events requires that we understand how material properties, particularly electrical conductivity, affect charge mobility and accumulation. The regolith is strongly insulating and its low conductivities ($<10^{-9}$ S/m at lunar-relevant temperatures) (Strangway et al., 1972) make it susceptible to breakdown during SEP events with fluences $>10^{10}$ particles cm^{-2}. Although we did not measure the electrical conductivities of our samples, an increase in FeO abundance is known to enhance the conductivity of silicates (e.g., Ciżman et al., 2017; Sirk et al., 2010). We therefore use iron abundance as a proxy for conductivity in our interpretations. Our results show that increasing iron abundance has a strong, positive correlation with the minimum fluence required to initiate breakdown. This relationship

indicates space weathering by breakdown is strongly influenced by the conductivity of lunar grains. For iron oxide abundances below ~10 wt%, the response was especially sensitive and indicated that even minor differences in composition (or conductivity) may lead to observable differential breakdown weathering trends.

Phase-dependent differential weathering, which has been identified in lunar samples and inferred from orbital observations, has been attributed to the availability of Fe^{2+} to produce the nanophase metallic iron particles primarily responsible for optical maturation (e.g., Burgess and Stroud, 2018; McFadden et al., 2019). However, electrical conductivity imparted by iron within the lattice structure has been proposed as an additional control on the production rate of metallic iron particles (Moroz et al., 2014). Because micrometeoroid impacting and dielectric breakdown are similarly energetic processes, it is reasonable to assume both processes generate similar volumes of melt and vapor. Thus, the production of nanophase iron by breakdown is likely to be a partial function of target material conductivity. As a result, we predict the frequency of breakdown to be low, and the relative production of iron nanoparticles to be enhanced, in iron-rich regolith.

Although iron abundance controls the minimum fluence required for breakdown to occur, it does not affect the resulting primary damage types (e.g., erosional channels, melt, and vapor). However, conductivity may increase the efficiency of plasma propagation. If so, the higher conductivity of diopside may explain why its primary and secondary flashover channels were longer and more structurally complex than those in the labradorite, despite diopside having fewer total discharge events. While variations in the goodness of polish and crystal orientation cannot be ruled out as alternative

explanations, channel lengths and structural complexity of breakdown channels in each sample were consistent among multiple experimental runs. This suggests that electrical conductivity was more likely to have played a role in flashover characteristics than imperfections in the sample surface.

3.5.4 Implications for the lunar surface

Highlands vs. Mare. The correlation between conductivity (iron abundance) and the minimum fluence required to initiate breakdown has substantial implications for how breakdown weathering could affect optical signatures of the dichotomous lunar surface. The total number of discharge events for a given particle fluence is directly related to the dielectric properties of the target material (e.g., conductivity and dielectric strength). Thus, we expect breakdown to occur much more readily in the highlands, where conductivities and charge dissipation rates are lower than they are in the maria. Additionally, much of the nearside highlands have FeO abundances of 6-8 wt%, whereas the farside, outside of the South Pole-Aitken basin, has abundances of 2-6 wt%. The breakdown sensitivity of materials with <10 wt% FeO indicates there may be differential weathering effects by breakdown between nearside and farside highlands material.

Chemical differentiation of the target material occurred during both flashover events and eruptive subsurface discharges. Melt deposits were found to be Si-enriched. Although the melt was depleted in iron and magnesium, we found no evidence for the presence of metallic iron was found within associated vapor-deposited rims. The Si-enriched melt deposits could possibly contribute to optical brightening (Adams, 1975),

but those optical effects may be counteracted by the deposition of Fe-enriched vapor deposits.

Although we predict a lower frequency of breakdown events is predicted for the maria when compared to the highlands, the optical effect within the two terrains may be similar. The production of iron nanoparticles is enhanced in iron-rich target materials. Thus, given any single breakdown event, we should expect this event to produce more nanophase iron within mare vapor deposits than it would in highland vapor deposits. However, the frequency of highland discharging events is predicted to be much higher than in the mare, so over time, discharge may play a comparable or equal role in space weathering for the two terrains. Additional studies, including those that incorporate spectral reflectance measurements, are required to effectively determine the optical effects of dielectric breakdown.

Permanently Shadowed Regions. Because cold temperatures reduce material conductivity and increase discharging timescales, in permanently shadowed regions (PSRs) with temperatures below ~120 K, breakdown may occur at frequencies approximately twice that of illuminated areas at high latitude (Jordan et al., 2019). The normal albedo inside PSRs measured by the Lunar Orbiter Laser Altimeter (LOLA) at 1064 nm (Lucey, 2014) is generally higher than in illuminated areas. Conversely, the plane albedo measured by the Lyman Alpha Mapping Project (LAMP) is lower within PSRs across multiple wavelengths within the far-ultraviolet range (Gladstone, 2010; 2012). A reduction in optical maturation cannot explain the reduced far-UV albedos because nanophase iron increases Lyman-α albedo and has no effect on on-band albedo (Byron et al., 2019). Instead, the low far-UV albedo may be explained by increased

porosity resulting from a change in grain size distribution. Breakdown occurs preferentially along grain boundaries and liberates the constituents of polycrystalline grains and rocks, as evidenced in these experiments and in other studies (e.g., Andres and Bialecki, 1986; Biela et al., 2009). If grains separated by breakdown are small enough for van der Waals forces to overcome gravity, then the low albedos measured by LAMP could be explained by increased porosity that contributes to the structure of the epiregolith (Shusterman et al., 2016; Jordan et al., 2015; Hapke and Horn, 1963). However, the extent to which the melt produced during breakdown events may contribute to agglutination of the finest fraction is not yet known.

An increase in porosity should also cause darkening within the near-infrared, but instead, normal albedo is increased at 1064 nm. One explanation may be that the high porosity exists only in the epiregolith (on the scale of <200 nm) (Cahill et al., 2019). The solar wind flux within PSRs is reduced by as much as 90% relative to equatorial latitudes, so grain surfaces may not be as reduced as they are in illuminated areas (Rhodes and Farrell, 2020). Nanophase iron is less likely to form from sublimated material when the surface has not already been reduced. A decrease in the abundance of metallic iron nanoparticles in PSRs would then lead to the increased near-IR albedo relative to illuminated areas that receive the total solar wind flux. Additional work is underway to investigate the effects of deep dielectric breakdown on grain size distributions in granular samples.

Absence of evidence in lunar samples. The fluences at which dielectric breakdown occurred in these experiments suggests that evidence of breakdown should be detectable in the lunar regolith. However, a key question is: why have we not identified physical

evidence of dielectric breakdown in the lunar sample collection? Several differences between the experimental and natural environments may provide some explanations for the absence of distinct breakdown-related features in regolith grains.

First, the results presented herein represent breakdown effects in relatively large grains (~1 mm), which make up a minority fraction of the top few millimeters of regolith. Large samples were required because high-energy discharges in fine granular materials result in the displacement of many grains, making it impractical to locate and characterize damaged grains. We expect variations in grain size will affect the minimum breakdown fluence threshold, and possibly the types of damage produced, both because the electric field among loosely packed grains is complex when compared to a single crystal and because dielectric strength is controlled by grain size.

Due to the use of a mono-energetic beam, our experiments deposited electrons in a thinner layer than would naturally form during SEP events. It is unknown how SEPs, which cover a broad range of energies, would be distributed among and within loosely-packed regolith grains with diameters <100 um, or how that charge distribution would affect the likelihood of dielectric breakdown. Experiments to determine the effects of breakdown in granular materials have been conducted (Shusterman et al., 2016; Izenberg et al., 2018), but these were performed under non-ideal conditions and prior to the characterization of damage caused by breakdown. Experiments in granular materials should be revisited and spectrally analyzed with the consideration of damage presented in this study.

Second, polishing the samples may have encouraged the prevalence of erosional flashovers. While surface irregularities can create areas of enhanced electric fields that

act as nucleation points for dielectric breakdown, too much surface roughness inhibits electron avalanches – a critical component of the flashover process. The surface roughness of lunar grains may therefore prevent or inhibit the formation of flashovers. We were unable to induce discharge in a roughened diposide surface, which is consistent with this hypothesis. Additional studies that evaluate the fluence required to initiate dielectric breakdown as a function of surface roughness are required to understand whether this process could occur in the natural lunar environment.

Third, subsurface breakdown features may be significantly more difficult to find because surface expressions (eruptive pits), which can be used to identify locations of subsurface breakdown, only occur in a fraction of such events. If breakdown channels are preserved in lunar grains, they will most likely be found in iron-depleted minerals at latitudes >40° and <-40°, and especially in regions of persistent and permanent shadow (Jordan et al., 2019). Furthermore, all Apollo samples were collected within ~25 degrees of the equator, where as little as 2% of grains are predicted to be affected by dielectric breakdown (Jordan et al., 2019).

The chemical differentiation of vapor that results from breakdown may be very similar to that which occurs from micrometeoroid bombardment. Isotopic analysis may be required to differentiate melts produced by the similarly energetic processes. Isotopic analyses have been conducted on iron nanoparticles to determine their origins (Wang et al., 2012), but no such study has been conducted on the amorphous layers that form complex weathered rims.

As with all space weathering mechanisms that act together to form complex rims, there are a number of variables that control the overall contribution of each mechanism.

To fully characterize the contribution of dielectric breakdown, additional work is required to better constrain the effects of discharging as a function of grain size, bulk density, and surface roughness. Furthermore, our experiments evaluated the effects of electrons representative of the lowest energy SEPs. Additional work that includes higher energy particles and a mixture of protons and electrons could help us better understand charging behavior within regolith in the natural environment.

3.6 Conclusions

We experimentally discharged a series of silicate minerals via deep dielectric charging and found that dielectric breakdown may play a role in the optical evolution of regolith through the production of chemically differentiated melt and vapor, and by changing the grain size distribution within the top 1 mm of regolith. Two independent discharge phenomena occurred with frequencies that were strongly dependent on iron abundance. Flashovers produced large vapor deposits and melt-lined erosional channels that propagated with fractal geometries. The high temperatures and pressures during subsurface discharging created melt-filled channels, significant lattice strain, and in some cases, the deposition of melt and vapor on sample surfaces. Although melt deposits were Si-enriched, we were unable to locate any Fe-enriched phases. We assume our experimental conditions prevented the formation of nanophase iron and that in the natural environment, nanophase iron is likely to be a major product of dielectric breakdown.

The correlation between breakdown frequency and iron abundance has strong implications for the contribution of dielectric breakdown to regional and global maturation trends. We predict breakdown should occur more readily in the highlands than

in the maria. Because the sensitivity to particle fluence is strong for materials with <10 wt% FeO, there may be measureable differences in optical maturation between the nearside and farside highlands. A latitudinal trend is also predicted to exist because temperature plays a key role in material conductivity and because the solar wind, which varies as a function of latitude, may enhance the production of nanophase iron.

We have shown that deep dielectric charging of silicates by single-energy electrons results in dielectric breakdown at high vacuum and room temperature. Although the majority of space weathering experiments use protons or helium at energies ranging from 1 keV – 4 keV, many utilize energies and fluxes higher than those used in the experiments presented herein. Furthermore, the total fluences supplied in most experimental weathering studies exceed the breakdown fluence threshold of ~10^{10} particles cm^{-2} by several orders of magnitude. Techniques to adequately neutralize samples and/or verify the absence of breakdown damage should be employed when studying other space weathering processes, such as solar wind irradiation.

Dielectric breakdown as a space weathering process is understudied and the conditions under which it occurs in the lunar environment are not well known. Grain size, target temperature, and target energies impact the likelihood of breakdown, the location of discharge nucleation, and its microstructural and chemical effects. Additional studies are required to constrain the effects of breakdown in highly-porous, granular materials on charging behaviors and the impact of very low temperatures on conductivity. Future experiments should focus on characterizing the conditions under which dielectric breakdown may produce nanophase iron. Furthermore, the analysis of lunar grains collected at latitudes ≥ 80° and ≤ -80°, especially from permanently shadowed regions,

could provide significant insight into the role of dielectric breakdown in overall space weathering.

3.7 References

Adams, J. B. (1975). Interpretation of visible and near-infrared diffuse reflectance spectra of pyroxenes and other rock-forming minerals. Infrared and Raman spectroscopy of lunar and terrestrial minerals, 91-116.

Balmain, K.G. (1980) Surface discharge effects, Space systems and their interactions with Earth's environment, Henry B. Garrett and Charles P. Pike, Progress in Astronautics and Aeronautics, 71, 276-298.

Blewett, D. T., Denevi, B. W., Cahill, J. T., & Klima, R. L. (2021). Near-UV and near-IR reflectance studies of lunar swirls: Implications for nanosize iron content and the nature of anomalous space weathering. Icarus, 364, 114472.

Budenstein, P.P. (1980) On the mechanism of dielectric breakdown in solids, IEEE Transactions on Electrical Insulation, 3, 225-240.

Buhler, C. R., C.I. Calle, J.S. Clements, J.G. Mantovani and M.L. Ritz (2007). Test method for in situ electrostatic characterization of lunar dust. IEEE Aerospace Conference, 1-19.

Burgess, K.D. and R. M. Stroud (2018) Phase dependent space weathering effects and spectroscopic identification retained helium in a lunar soil grain, Geochimica et Cosmochimica Acta, 244, 64-79.

Byron, B. D., Retherford, K. D., Greathouse, T. K., Mandt, K. E., Hendrix, A. R., Poston, M. J., ... & Mazarico, E. (2019). Effects of space weathering and porosity on the far-UV reflectance of Amundsen crater. Journal of Geophysical Research: Planets, 124(3), 823-836.

Ciżman, A., E. Rysiakiewicz-Pasek, M. Krupiński, M. Konon, T. Antropova, & M. Marszałek (2017). The effect of Fe on the structure and electrical conductivity of sodium borosilicate glasses. Physical Chemistry Chemical Physics, 19(34), 23318-23324.

Demers, H., Poirier-Demers, N., Couture, A. R., Joly, D., Guilmain, M., de Jonge, N., & Drouin, D. (2011). Three-dimensional electron microscopy simulation with the CASINO Monte Carlo software. Scanning, 33(3), 135-146.

Denig, W.F. and A. R. Frederickson (1985) Deep-dielectric charging – A review, Environmental Research Papers, No. 919.

Frederickson, A.R. (1980) Radiation induced dielectric charging, Space systems and their interactions with Earth's space environment, Henry B. Garrett and Charles P. Pike, Progress in Astronautics and Aeronautics, 71, 386-412.

Frederickson, A.R., E.G. Holeman and E.G. Mullen (1992) Characteristics of spontaneous electrical discharging of various insulators in space radiations. IEEE Transactions on Electrical Insulation, 27(6), 1166-1178.

Garrett, H. B., & Evans, R. W. (2001). Internal electrostatic discharge environment at Jupiter.

Garrick-Bethell, I., J. W. Head III and C.M. Pieters (2011) Spectral properties, magnetic fields, and dust transport at lunar swirls, Icarus, 212(2), 480-492.

Glotch, T.D., J.L. Bandfield, P.G. Lucey, P.O. Hayne, B.T. Greenhagen, J.A. Arnold, R.R. Ghent and D.A. Paige (2015) Formation of lunar swirls by magnetic field standoff of the solar wind, Nature Communications, 6(1), 1-8.

Green, N.W. and A.R. Frederickson (2006) A study of spacecraft charging due to exposure to interplanetary protons, AIP Conference Proceedings, 813(1), 684-700.

Green, N. W., & Dennison, J. R. (2008). Deep dielectric charging of spacecraft polymers by energetic protons. IEEE transactions on plasma science, 36(5), 2482-2490.

Guo, B.-H., G.-Y. Sun, S. Zhang, J.-Y. Xue, R.D. Zhou, B.-P. Song, H.-B. Mu, and G.-J. Zhang (2019) Mechanism of vacuum flashover on surface roughness, Journal of Physics D: Applied Physics, 52, 215301.

Hapke, B. (2001) Space weathering from Mercury to the asteroid belt, Journal of Geophysical Research, 106, 10039-10074.

Hemingway, D.J., I. Garrick-Bethell and M.A. Kreslavsky (2015) Latitudinal variation in spectral properties of the lunar maria and implications for space weathering, Icarus, 261, 66-79.

Izenberg, N. R., Drabenstadt, C. W., Nichols, J. R., Jordan, A. P., & Stubbs, T. J. (2018). Pilot Experiments in Dielectric Breakdown Space Weathering of Planetary Regolith Analogs. In 49th Annual Lunar and Planetary Science Conference (No. 2083).

Jordan, A.P., T.J. Stubbs, J.K. Wilson, N.A. Schwadron, H.E. Spence, and C.J. Joyce (2014) Deep dielectric charging of regolith within the Moon's permanently shadowed regions, Journal of Geophysical Research: Planets, 119, 1806-1821.

Jordan, A.P., T.J. Stubbs, J.K. Wilson, N.A. Schwadron and H.E. Spence (2015) Dielectric breakdown weathering of the Moon's polar regolith, Journal of Geophysical Research: Planets, 120, 210-225.

Jordan, A.P., T.J. Stubbs, J.K. Wilson, N.A. Schwadron and H.E. Spence (2017) The rate of dielectric breakdown weathering of lunar regolith in permanently shadowed regions, Icarus, 283, 352-358.

Jordan, A. P., T. J. Stubbs, M. L. Shusterman, N. R. Izenberg, J. K. Wilson, P. O. Hayne, N. A. Schwadron and H. E. Spence (2019) How dielectric breakdown may contribute to the global weathering of regolith on the Moon. Icarus, 319, 785-794.

Jordan, A. P. (2021), Evidence for dielectric breakdown weathering on the Moon, Icarus, 358, 114199.

Keller, L. P. and D. S. McKay (1997) The nature and origin of rims on lunar soil grains, Geochimica et Cosmochimica Acta, 61(11), 2331-2341.

Keller, L.P. and S. Zhang (2015) Rates of space weathering in lunar soils, Lunar and Planetary Science Conference, Abstract 2056.

Lemelle, L., L. Beaunier, S. Borensztajn, M. Fialin and F. Guyot (2003) Destabilization of olivine by 30-keV electron irradiation: A possible mechanism of space weathering affecting interplanetary dust particles and planetary surfaces, Geochimica et Cosmochimica Acta, 67(10), 1901-1910.

Lucey, P.G., G.A. Neumann, M.A. Riner, E. Mazarico, D.E. Smith, M.T. Zuber, D.A. Paige, D.B. Bussey, J.T. Cahill, A. McGovern and P. Isaacson (2014) The global albedo of the Moon at 1064 nm from LOLA, Journal of Geophysical Research: Planets, 119(7), 1665-1679.

McGuire, R.E. and T.T. von Rosenvinge (1984) The energy spectra of solar energetic particles, Advances in Space Research, 4(2-3), 117-125.

Miller, H.C. (2015) Flashover of insulators in vacuum: The last twenty years, IEEE Transactions on Dielectrics and Electrical Insulation, 22(6), 3641-3657.

Moroz, L. V., Starukhina, L. V., Rout, S. S., Sasaki, S., Helbert, J., Baither, D., ... & Hiesinger, H. (2014). a. Icarus, 235, 187-206.

Pieters, C.M. and S.K. Noble (2016) Space weathering on airless bodies, Journal of Geophysical Research: Planets, 121(10), 1865-1884.

Poppe, A.R., W.M Farrell and J.S. Halekas (2018) Formation timescales of amorphous rims on lunar grains derived from ARTEMIS observation, Journal of Geophysical Research: Planets, 123(1), 37-46.

Rhodes, D. J., & Farrell, W. M. (2020). Mapping the Predicted Solar Wind Hydrogen Flux in Lunar South Pole Craters. The Planetary Science Journal, 1(1), 13.

Shusterman, M. L., Sharp, T. G., & Robinson, M. S. (2021, March). Dielectric Breakdown Weathering: Morphological Effects of Electrical Breakdown in Laboratory-Irradiated San Carlos Olivine. In Lunar and Planetary Science Conference (No. 2548, p. 2141).

Shusterman, M. L., Izenberg, N. R., Wing, B. R., Irvin, B. L., & Liang, S. X. (2016). Laboratory Simulation of Dielectric Breakdown of Lunar Regolith Simulant JSC-1A. In Annual Meeting of the Lunar Exploration Analysis Group (Vol. 1960, p. 5056).

Sim, C.K., S.S. Kim, P.G. Lucey, I. Garrick-Bethell and Y. -J. Choi (2017) Asymmetric space weathering on lunar crater walls, Geophysical Research Letters, 44(22), 11273-11281.

Sirk, A. H., Sadoway, D. R., & Sibille, L. (2010). Direct electrolysis of molten lunar regolith for the production of oxygen and metals on the moon. ECS transactions, 28(6), 367.

Sørensen, J., D.J. Rodgers, K.A. Ryden, P.M. Latham, G.L. Wrenn, L. Levy and G. Panabiere (1999) ESA's tools for internal charging, RADECS 99 (Cat. No. 99TH8471), 27-33.

Strangway, D. W., Chapman, W. B., Olhoeft, G. R., & Carnes, J. (1972). Electrical properties of lunar soil dependence on frequency, temperature and moisture. Earth and Planetary Science Letters, 16(2), 275-281.

Stubbs, T.J., W.M. Farrell, J.S. Halekas, J.K. Burchill, M.R. Collier, M.I. Zimmerman, R.R. Vondrak, G.T. Delory, and R.F. Pfaff (2014) Dependence of lunar surface charging on solar wind plasma conditions and solar irradiation. Planetary and Space Science, 90, 10-27.

Wang, D., M. Mookherjee, Y. Xu, and S. Karato (2006) The effects of water on the electrical conductivity in olivine, Nature, 443, 977-980.

Wang, K., Moynier, F., Podosek, F. A., & Foriel, J. (2012). An iron isotope perspective on the origin of the nanophase metallic iron in lunar regolith. Earth and Planetary Science Letters, 337, 17-24.

Wolak, M.A., A.S. Wan, J.S. Shirk, M. Mackey, A. Hiltner, and E. Baer (2012) Imaging the effect of dielectric breakdown in a multilayered polymer film, Journal of applied polymer science, 123(4), 2548-2557.

Yang, X., H. Keppler, C. McCammon, H. Ni, Q. K. Xia and Q. Fan (2011) Effect of water on the electrical conductivity of lower crustal clinopyroxene, Journal of Geophysical Research, 116(B4).

Yang, X., H. Keppler, C. McCammon, H. Ni (2012) Electrical conductivity of orthopyroxene and plagioclase in the lower crust, Contributions to Mineralogy and Petrology, 163(1), 33-48.

THE FUTURE OF SPACE WEATHERING RESEARCH

The Moon and other airless bodies across the Solar System are subjected to a number of damaging processes that alter the chemical, structural, and optical properties of the surface. Extensive research including remote observations, laboratory analyses of extraterrestrial samples, and laboratory simulations of space weathering processes has uncovered the primary mechanisms and products responsible for space weathering. However, there are still outstanding questions with elusive answers. Studying the effects of particle flux and fluence, target temperature, compositional resistance to weathering, and damage formation and relaxation rates as a function of these parameters can provide insight into discrete albedo anomalies, global and regional reflectance trends, lunar swirls, and weathering processes in permanently shadowed regions.

Space weathering is a convolved process with many mechanisms that work over different timescales and are controlled by different material and environmental parameters. Experimental research should be designed to control for as many parameters as is practical to avoid making erroneous conclusions and global assumptions based on results from a single use case. Experimental studies should be combined with observations and models to deconvolve the complicated time-dependent processes that act together to optically mature the regolith. Although micrometeoroid impacts and solar wind implantation are known to alter planetary surfaces, new avenues of research should be pursued to better understand the role of higher energy particles and the parameters that lead to globally heterogeneous weathering.

4.1 Experimental Studies

Reduce laboratory particle fluxes. High particle fluxes used in laboratory simulations of solar wind space weathering have been shown to produce damage regimes that are inconsistent with regimes in the natural lunar environment. High fluxes accelerate the accumulation of lattice defects which increases the rate of amorphization and decreases the rate of relaxation. Additionally, fluxes $>10^{10}$ particles cm^{-2} s^{-1} may induce dielectric breakdown and affect material properties that control optical signatures.

To better understand the amorphization rate of indigenous lunar space weathered rims, the lowest practical beam flux should be used. A series of experiments using progressively lower particle flux could provide insight into the relationship between damage formation rates at standard laboratory fluxes (e.g., 10^{12}-10^{13} particles cm^{-2} s^{-1}). Where laboratory fluxes cannot be lowered for practical purposes, sample temperatures should be adjusted to compensate for increased damage production rates (e.g., heat samples to accelerate defect relaxation rates). Once damage accumulation and relaxation rates have been correlated to particle flux and sample temperatures, low-fluence experiments could be used to better constrain the formation timescale of indigenous rims.

Control for temperature. Latitudinal trends in reflectance and anomalous reflectance measurements in some permanently shadowed regions are likely to be the result of differential weathering patterns based in part on temperature-controlled damage recovery rates. The optical maturation of regolith decreases with increasing latitude, despite damage recovery rates also decreasing with latitude. Performing irradiation experiments across a range of temperatures will constrain the rates at which indigenous

rims form with respect to latitude and help determine the total exposure time required to produce detectable optical changes.

Control for electric charging. The effects of dielectric breakdown in natural silicate minerals are understudied. The basic discharge event types and resulting damage structures have been characterized but there are many parameters that have yet to be constrained. A primary focus of experimental dielectric breakdown work should be to determine the conditions under which breakdown can produce $SMFe^0$. These conditions are critical for understanding whether dielectric breakdown weathering could measurably contribute to the optical maturation of lunar regolith. Additionally, grain size strongly affects the dielectric properties of a material and experiments using granular samples will be necessary for determining how resulting complex electric fields affect the likelihood of breakdown during SEP events.

Other non-breakdown irradiation-based space weathering studies should also include mitigation techniques to prevent sample charging and discharging. Low-energy electron flood guns are likely sufficient for preventing flashovers, but dielectric breakdown may be occurring in experiments using particles that penetrate hundreds of nanometers or more into the surface. The spectral effects of these internal discharges still needs to be characterized, but early work suggests the process may change grain size distributions and deposit Fe-rich melt and vapor.

Consider the Role of Glass. The density change of maskelynite occurred under a proton beam with a flux of ~$1x10^{13}$ particles cm^{-2}, 5 orders of magnitude more flux than the solar wind at 1 AU. To date, the densification or dilation of glass has not been recorded in the lunar sample collection. A comprehensive study on the spectral effects of irradiated

natural silicate glasses would be helpful for determining whether density changes of glassy materials occurs on the lunar surface as a result of solar wind or solar energetic particle irradiation, or if the spectral signature of laboratory-irradiated regolith samples containing glassy phases is affected by the densification and dilation processes.

4.2 Observational, In Situ, and Sample Studies

Swirls. Lunar swirls provide an opportunity to discriminate the effects of different weathering processes. The magnetic fields co-located with most swirls deflect low-energy solar wind particles, making them a prime location for studying the distinctions between solar wind and micrometeoroid contributions to optical space weathering. An upcoming Commercial Lunar Payload Services (CLPS) mission will carry a small rover called Lunar Vertex (Blewett et al., 2022) that will traverse through a portion of Reiner Gamma, the Moon's most prominent swirl. An onboard plasma spectrometer will take measurements of plasma densities inside and outside the local magnetic field lines. These measurements, along with measurements from an onboard magnetometer, will provide insight into how much solar wind is effectively deflected by the weak magnetic fields.

While Lunar Vertex will be the first mission specifically designed to investigate the magnetic field and solar particle access at swirls, there are additional in-situ measurements that would provide a more holistic picture of how weathering processes differ globally with respect to incident particle fluxes. A companion instrument on the same CLPS mission is Korea's Lunar Surface Environment Monitor (LUSEM) (Sim et al., 2021). This stationary instrument will measure high-energy particles >50 keV over a period of 13 days. LUSEM will help determine the effects of weathering caused by solar energetic particle (SEP)

events. However, it would be beneficial to have long-lived, rover-mounted solid-state telescopes that could measure cosmic radiation with respect to magnetic field strength and time. Combining the data from a plasma spectrometer and solid-state telescopes for high-energy particles would provide a full spectrum of data that could be used to better understand the effects of ionizing radiation on the surfaces of airless bodies.

Sample collection and delivery from swirls would also significantly contribute to our understanding of the origin of their origins and the cause for their optically bright expressions. In addition to sample collection at Reiner Gamma, collections at multiple swirls near Goddard B in *Mare Marginis* would be possible with a long-lived rover capable of traversing 15-20 km. Measurements from these swirls, which are significantly smaller and co-located with much weaker magnetic anomalies than Reiner Gamma, would provide for a strong comparative study. To determine how lower solar wind fluxes affect damage accumulation and recovery rates, the solar flare track density and indigenous rim thickness of grains from inside swirls should be compared to already characterized samples collected outside of swirls.

Permanently Shadowed Regions. Permanently shadowed regions provide unique opportunities to study controls on space weathering because they have both a significant reduction in solar wind access, and they have very low temperatures that reduce lattice defect recovery rates and regolith conductivities. As a result, the effects of solar wind weathering should be suppressed, hydrogen retention should be enhanced, and dielectric breakdown should occur with high frequencies compared to equatorial latitudes. Difficult terrain and lighting conditions have made it difficult to study PSRs. However, there are

emerging opportunities to improve our understanding of surface processes occurring in these unique environments.

High resolution and high signal-to-noise imaging of PSRs by ShadowCam (Robinson et al., 2017), in conjunction with spectral data in the far-ultraviolet range using the Lyman-α Mapping Project (LAMP) instrument onboard the Lunar Reconnaissance Orbiter (Gladstone et al., 2010), could reveal ways in which weathering processes differ at very low temperatures and in the near-absence of solar wind implantation. LAMP data indicates dielectric breakdown may play a role in the formation of "fairy castle" structures. Thus, a LAMP investigation that considers small temperature variations in and around PSRS or small compositional differences at latitudes beyond beyond 80° (N/S) could provide insight into the extent to which breakdown contributes to porosity in the epiregolith.

NASA's Aretemis III polar landing will also provide opportunities to collect samples from the lunar South Pole. There, up to 25% of grains within the top few millimeters of regolith are predicted to have experienced at least one breakdown event. The collection of grains, even in illuminated regions of the South Pole, will provide an important comparative measure to help determine how latitude affects maturation rates of the regolith. A strong comparative study would include the evaluation of rims formed at equatorial latitudes, those formed inside swirls and magnetic anomalies, and those formed at the highest latitudes and/or in permanently shadowed regions. This collection of measurements would highlight separately the effects of solar wind, micrometeoroids, and dielectric breakdown. The addition of sealed samples collected from the surface or as a core would also enhance our understanding of volatile retention and release mechanisms.

4.3 First Principles and the Big Picture

Future investigations of space weathering processes in the lunar environment should emphasize experimental work grounded in first principles. Focusing on first principles will help us understand how our experimental results differ from processes on the lunar surface that cannot be recreated in laboratory settings, then allow us to expand our scope beyond the effects of single processes. The space environment is complex and dynamic, and it is important to simultaneously consider the variety of processes contributing to space weathering and the interactions among them. A holistic approach to experimental work is required to gain a complete and accurate understanding of these phenomena.

The planetary science community has a number of upcoming opportunities to collect new measurements of the lunar surface and analyze novel samples retrieved from sites that have not yet been explored. These opportunities will fill knowledge gaps and lead us towards new perspectives on space weathering on the Moon. A more thorough understanding of individual and combined weathering effects will improve our interpretations of remote sensing observations, new and existing extraterrestrial samples, as well as samples that have undergone simulated space weathering treatments. Furthermore, these new insights will inform more mature models that describe how space weathering affects airless bodies throughout the Solar System.

4.5 References

Blewett, D. T., Halekas, J., Ho, G. C., Greenhagen, B. T., Anderson, B. J., Vines, S. K., ... & Ames, W. F. (2022). Lunar Vertex: A Low-Cost Lander-Rover Investigation of Reiner Gamma. LPI Contributions, 2695, 6022.

Gladstone, G. R., Stern, S. A., Retherford, K. D., Black, R. K., Slater, D. C., Davis, M. W., ... & Hendrix, A. R. (2010). LAMP: the Lyman alpha mapping project on NASA's Lunar reconnaissance orbiter mission. Space Science Reviews, 150, 161-181.

Robinson, M. S., Mahanti, P., Carter, L. M., Denevi, B. W., Estes, N. M., Ravine, M. A., ... & Wagner, R. V. (2017, September). ShadowCam—Seeing in the dark. In Proceedings of the European Planetary Science Congress, Riga, Latvia (pp. 17-22).

Sim, C. K., Choi, Y. J., Ye, S. J., Jin, H., Seon, J., Kim, S. S., ... & Team, C. K. (2021, March). Korea's First Scientific Instruments on the Lunar Surface. In 52nd Lunar and Planetary Science Conference (No. 2548, p. 1806).

ACCESSCOLOR: PRODUCING PALETTES FOR DIVERSE COLOR ACUITIES

This manuscript is under review with the Journal of Geoscience Education.

5.1 Abstract

Color is an essential tool for conveying information and when used effectively, colors appear logically ordered, tell a coherent story, and draw the reader's eye to critical data or features. However, for nearly 9% of the population, color-vision deficiencies (CVD) reduce the number of perceptible colors and limit the ability to interact with and interpret data. Barriers for those with CVD are prominent in many fields, including STEM, where color communicates spatially and temporally varying data sets (e.g., geological sciences) or in which color accuracy is critical (e.g., electrical engineering and medicine). Recent efforts to improve equity, diversity, and inclusion in the sciences have become a catalyst for introducing tools that help scientists better communicate data and findings to broader audiences. Amongst these are a set of tools specifically designed to improve data visualizations for data product consumers with color vision deficiency.

Here we present AccessColor, an algorithm and web tool designed to generate color palettes that maximize the perceptual difference between adjacent palette colors while maintaining a logical order to present data intuitively for audiences with a broad range of color-vision acuities. We will discuss the physiology of color vision and color-vision deficiency, then introduce the methods used to produce accessible color palettes. Finally, we will provide an overview of the web application and its functionality. By introducing this dynamic tool, we intend to make it easier for scientists and educators to present their data in ways that are more accessible to audiences with reduced color vision

acuity.

5.2 Introduction

The optimized use of color palettes in data visualizations is critical for accurately and unambiguously communicating scientific information. The most useful visualizations include colors that are logically ordered, semantically resonant (colors associated with particular objects, information, or other colors), and easily perceptible; and which draw the reader's eyes to essential features (Taft, 1996). However, for nearly 9% of the population (Birch, 2012; Feig & Ropers, 1978), color-vision deficiencies (CVD) reduce the number of perceptible colors (color acuity) and limit the reader's ability to interact with and interpret data. Color vision deficiencies also interfere with a person's ability to make color-object or color-data associations, resulting in a narrow color-related vocabulary. As a result of these traits, those with CVD may find it more challenging and time-consuming to interpret, comprehend, and discuss visual data compared to those with normal color vision.

Defects in photoreceptors within the retina are responsible for color-vision deficiencies. The severity of CVD varies greatly among affected individuals. While some are profoundly impacted in ways that are apparent early in life, the impact on others may be more subtle, leading to a later diagnosis. Students with undiagnosed CVD often underperform in color-related tasks, and their difficulties may present similarly to neurological learning disorders (Espinda, 1973; Wilkinson, 1992). A study investigating students' performance in a high school-level biology course found that those with CVD consistently received lower grades than classmates with unimpaired color vision

(Dannenmaier, 1972). Performance evaluations of medical students reveal similar results, where students with color-vision impairments make frequent mistakes when performing color-based tasks such as gram staining or detecting jaundiced skin (e.g., Spalding, 1999; Tocantins and Jones, 1933). In the geological sciences, those with CVD may face their first major barriers in college courses (De Paor et al., 2017), where students are asked to perform color-based tasks such as interpreting geologic maps or identifying the colors of minerals in plane-polarized light. These difficulties are likely compounded when the student is tasked with additional color-based activities like identifying minerals or distinguishing among geologic map units in the field. Failure to successfully perform color-based tasks may ultimately deter or prohibit students from pursuing careers in science and technology fields. Optimizing the presentation of data via color and making reasonable accommodations for CVD students, readers, and data product consumers should be a priority for STEM professionals. Minimizing the encumbrance of color-related tasks can increase the retention and success rates of students with CVD and is key to effectively communicating scientific data to broad audiences.

Designing colormaps that accurately represent scientific data and are interpretable to those with CVD is challenging because visual design is often subject to stringent requirements. Several colormap generation models (Brewer, 2003; Jenny and Kelso, 2007; Gramazio et al., 2016; and others) have been designed to accomplish this goal and are widely utilized today. A growing interest in using these models indicates both a need and a willingness to use CVD-corrected palettes for communicating scientific and technical data. While these models have been proven to produce more suitable colormaps for some types of data, each comes with its limitations. In some models, the methods for

selecting color values are inconsistent with the physiological drivers of perceptual improvement. We believe that different data types and different modes of visual communication require a wider range of color choices and palette building options that currently available models do not represent.

Here we present AccessColor, a dynamic color palette-building tool that utilizes color schema mathematically derived from the optical sensitivity parameters of the human eye. This tool aims to promote the use of color palettes that accurately connect the structure of data with the perceptual dimensions of color while enhancing readability for those with CVD. The model approach prioritizes maximizing the perceptual distance between palette members and favors the user's ability to choose semantically-resonant colors. Given several input parameters, AccessColor produces colormaps that are more likely to be perceptible to those with the most common forms of CVD. This improved perceptibility is achieved by incorporating the following elements:

- Perceptual uniformity – *the distance in color space must be equal to the difference in perception of the colors;*
- Color constancy – *the colors must remain unchanged across relatively large changes in illumination;*
- Logical progression – *colors representing ordered data that include easily interpretable high and low values.*

5.2.1 Physiology and Neurological Basis for Color Vision

Color experience is a biological causal chain between photoreceptors in the eye and neuronal processing in the brain. The entire information processing system

contributes to the human ability to verbally describe one's respective color sensations, independent of any other person's sensations, given the same stimulus. Due to imprecise processing, there is no direct mapping among physical stimuli, physiological responses, and color appearance (Backhaus, 1998). Color sensations are derivatives of photons that enter the eye and is processed by photoreceptors in the retina (Fig. 5.1). There, optical images are translated into electrical impulses transmitted to the brain by the optic nerve (Fairchild, 2013). Two categories and four classes of photoreceptor cells are responsible for processing visual stimuli under various environmental conditions.

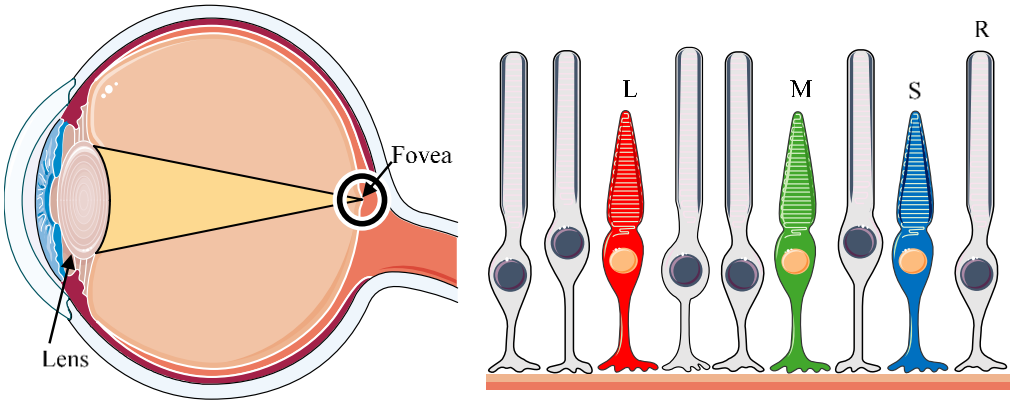

Figure 5.1. Anatomy of the Eye. (Left) Light enters the eye and is focused by the lens onto the fovea. (Right) Rods and cones densely populate the fovea and are responsible for color and nighttime vision. Derivative of "Eye" licensed under CC BY 3.0 by Servier Medical Art by Servier.

The two categories of photoreceptors responsible for visual processing under different illumination conditions are rods and cones. Rods are strongly sensitive to the intensity of reflected light and serve to enhance vision under low illumination conditions. The activation signal from rods, called scoptic vision, is not combined with the signal from any other photoreceptor and does not contribute to color vision. Scoptic vision allows a person to navigate a room with reflected moonlight as the only illumination source; in this case, the forms of unique objects in a room are distinguishable, but the

brain cannot assign colors to those objects. Cones populate the central fovea within the retina and are exclusively responsible for color vision, also called photopic vision. Each of the three cone classes have broad, sun-activated sensitivity peaks located along different regions of the visible spectrum (Table 5.1).

Table 5.1. Summary of reported retinal cone sensitivity peaks.

S-cone (nm)	M-cone (nm)	L-cone (nm)	Reference
440	540	575	Brown and Wald, 1964
420	534	564	Bowmaker and Dartnall, 1980
419	531	558	Dartnall et al., 1983
--	530	560	Schnapf et al., 1987
424	530	560	Oprian et al., 1991
426	530	557	Merbs and Nathans, 1992
--	530	563	Neitz et al., 1999
--	--	559	Kraft et al., 1998
426	*532*	*562*	*Average*

To understand the basis of color vision and color-vision deficiency, one must recognize that each cone class is sensitive only to photon flux and not to wavelength. At any given time, multiple cone classes are activated, and the relative absorption rates of each class are combined in the brain to generate trichromatic color sensations (Purves, 2001; Simunovic, 2010). As a result, humans can interpret single-wavelength light and light mixtures as the same color. We exploit this trait in the design of digital displays, for example, where red and green light are combined to make yellow.

Two nomenclatures exist to describe the three cone classes. Throughout this text we will use the “S, M, L” nomenclature, referring to the physical wavelength range (short, medium, and long) to which each cone class is sensitive. We intentionally avoid the more commonly used “R, G, B” nomenclature (red, green, and blue) here because the

use of color-associated terms is misleading in understanding how these photoreceptors function together to produce color sensations.

5.2.2 Color-Vision Deficiency

For those with unimpaired, trichromatic vision, the primary source of irregularity in color perception is variations in the color of the macula, a yellow-tinted filter that protects the eye from short-wavelength radiation (Kreissig et al., 1981). This variation does not fall under the definition of color-vision deficiency because CVD describes explicitly a variety of color perception disorders linked to photoreceptors in the retina; these disorders are the result of one or more poorly functioning, non-functioning, or missing cone classes that cause a shift in the location of sensitivity peaks. CVD is categorized into four types (monochromatism, dichromatism, anomalous trichromatism, and achromatism) based on the number of cone classes affected (Fig. 5.2) (Judd, 1943; Burnham et al., 1963). The severity of color vision deficiency falls along a broad spectrum, ranging from individuals unaware they have a color deficiency to those with a complete inability to experience chromatic vision. Figure 5.2 provides examples of what those with severe, end-member cases may see. The most noticeable effect of CVD is a reduction in successful color matching: the ability to reproduce color by adjusting the relative proportions of red, green, and blue lights (Wyszecki and Styles, 1982). Trichromats require exactly three colors of light to reproduce any color, given by $C=\alpha R+ \beta G+ \gamma B$, while an individual with CVD can match colors with only one or two colors of light: $C= \beta G+ \gamma B$ for red deficiency, $C= \alpha R+ \gamma B$ for green deficiency, and $C= \alpha R+ \beta G$ for blue deficiency (Pitt, 1943). Degeneracy in the total number of perceptible colors is

therefore revealed by the person's ability to match all colors using only one or two of the three colored lights.

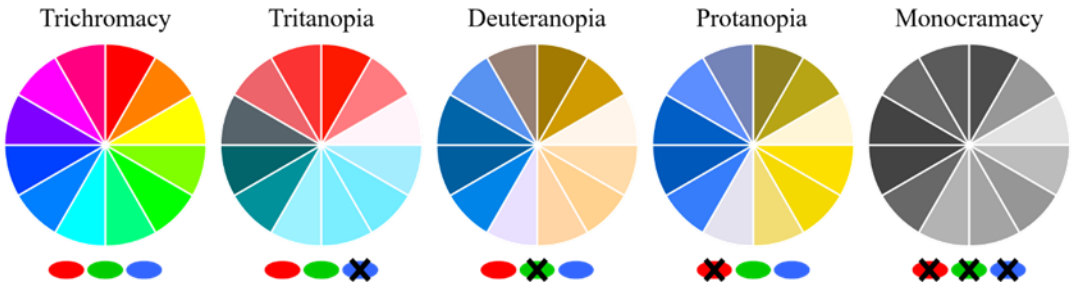

Figure 5.2. Color Vision Deficiencies. Colors as perceived by unimpaired vision (trichromacy) and three severe (end-member) forms of color vision deficiencies affecting S, M, and L cones. In monochromacy, all three cones (S, M, and L) are dysfunctional or absent.

5.2.3 Color Models

The three perceptual dimensions of human color vision are hue, saturation, and brightness (Fig. 5.3) (Wright, 1962; Wyszecki and Styles, 1982). Hue is the perceptual attribute that correlates a color (chromatic or achromatic) with one of the primary or secondary colors. Saturation describes the relative colorfulness of an object when compared to its brightness. Finally, lightness describes the ratio between the apparent emission of light from an object and a similarly illuminated object that is white in hue (Fairchild, 2013). Each color observed by the human eye can be described with a unique triplet containing a value for each perceptual dimension; color models transform these dimensions to describe colors differently. The number and range of colors that a given model can mathematically compute depends on the model's parameters, with dimensional boundaries constrained by the range of calculated triplets. Many models exist in general, and each serves a specific use. For example, additive RGB (red, green, and blue) colors

are best suited to light transmitted from a display whereas subtractive CMYK (cyan, magenta, yellow, and black) colors are better suited to light reflected off ink on paper.

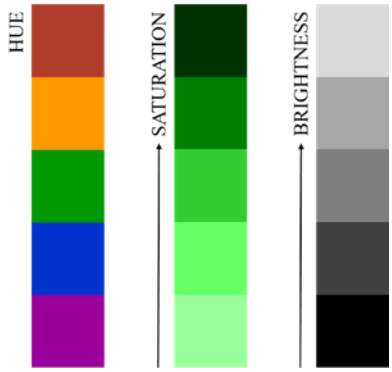

Figure 5.3. The three perceptual dimensions of color.

The RGB model is one of the most widely used color models for use in computer applications. This color space is a unit cell where [0 0 0] describes black and [1 1 1] describes white. The RGB model is additive, meaning that the combination of red, green, and blue in some proportion produces each color. Any colors falling along the diagonal from [0 0 0] to [1 1 1] are comprised of equal proportions of red, green, and blue and thus, represent the lightness dimension of the model. Although the production of colors in RGB space is computationally simple and does not require any transformations to display information on most commercially available screens, the colors are device-dependent because an RGB triplet may appear as a different color on different monitors. Additionally, the linear luminance function used in this model generates a color space that is not perceptually uniform (Fig. 5.4). Perceptual uniformity exists when the Euclidean distance between colors in model space is directly correlated to the perceptual difference between them (See review of color spaces by Ibraheem et al., 2012).

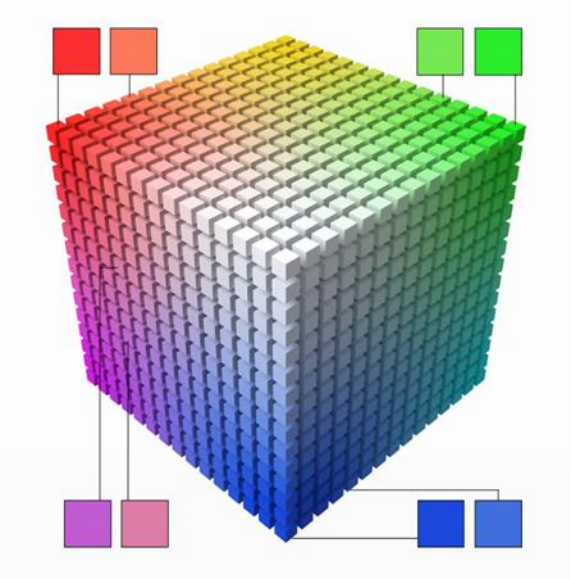

Figure 5.4. RGB color space. A segmented RGB unit cell shows the absence of color constancy. Each pair of colors is equidistant in space, yet the perceived difference between each of the paired colors is different (i.e., the two greens appear much more similar than the purple-pink pair).

Several models have been developed to address these problems including HSV (hue-saturation-value), HSI (hue-saturation-intensity), CIELUV (Robertson, 1990), and CIELab (McLaren, 1976). Although each of these models is approximately perceptually uniform, CIELab and CIELUV generate unintuitive palettes because they lack color constancy (Ibraheem et al., 2012), and HSV and HSI models contain undefined achromatic (black, grey, and white) hue values that do not translate back into RGB space for digital display.

These major pitfalls are addressed by the HCL (hue-chroma-luminance) model, which is built to provide color constancy, defined achromatic hues, and perceptual uniformity (Sarifuddin & Missaoui, 2005). In this model, chroma is defined as the colorfulness of an object or area compared to pure white considered under the same illumination conditions. Luminance describes the perceived radiance of an object or area

weighted by the luminosity function defined by CIE. Changes in luminance are proportional to changes in contrast, making this function more useful than the lightness attribute. In this model, chroma and hue can be defined as a combination of the three chrominance elemental sensations from the Munsell color system: R-G, G-B, and B-R (Munsell, 1919). Luminance values are extracted from RGB colors by considering three fundamentals: (1) a color containing more white is brighter than one containing less white, (2) a saturated color contains no white and has a maximum chroma value, and (3) an increasing value of white results in a decreasing chroma value. Luminance can therefore be defined as a function of Max(R,G,B) and Min(R,G,B). Consistent with human visual sensitivities, increasing luminance decreases the chroma, making a color appear whiter. Additionally, there is constancy in the angles between hues, meaning the spacing between primary and secondary colors are equal. Red, yellow, green, cyan, blue, and purple are located at 0˚, 60˚, 120˚, 180˚, 240˚, and 300˚, respectively (Sariffudin & Missaoui, 2005).

5.3 Palette Construction

The model presented here produces palettes that are functional for a wide range of color acuities by utilizing a color space with perceptual uniformity and color constancy. The addition of functions that (1) maximize the distance between adjacent palette colors and (2) create a smooth transition in luminance across the length of the palette allows this model to satisfy the three specific attributes that enable enhanced readability: color constancy, perceptual uniformity, and logical progression. The net result is that color palettes generated using AccessColor are closely traceable to how the human eye

perceives color.

Palette construction begins with user-defined parameters, including the input and output color model type (RGB, HCL, HEX, or CMYK), the desired number of bins, the selection of starting and ending (endmember) colors, and the choice of palette type. Two palette types are available, sequential and diverging. Sequential palettes are comprised of either a single hue or multiple hues along a straight line on the hue axis in HCL space. Diverging palettes have three user-defined color inputs (starting, ending, and intermediate values) where each half of the palette is independently populated either as a single-hued or multi-hued sequential palette.

5.3.1 Transformation from RGB to HCL Color Space

The HCL color space (herein referred to as "HCL-space"), defined by Sarifuddin and Missaoui (2005), is transformed from the RGB unit cell. HCL triplets are parameterized by hue expressed in degrees from -180° to 180°, chroma expressed in scaled values of 0 to 170, and luminance expressed in scaled values of 0 to 130 (Fig. 5.5). The general transformation is as follows:

$$Hue = \left[\frac{(G-B)}{(R-G)}\right] \quad 1$$

$$Chroma = \frac{e^{\frac{Min(R,G,B)}{100*Max(R,G,B)}*3}(|R-G| + |G-B| + |B-R|)}{3} \quad 2$$

$$Luminance = \frac{e^{\frac{Min(R,G,B)}{100*Max(R,G,B)}*3} * Max(R,G,B) + \left(1 - e^{\frac{Min(R,G,B)}{100*Max(R,G,B)}*3}\right) * Min(R,G,B)}{2} \quad 3$$

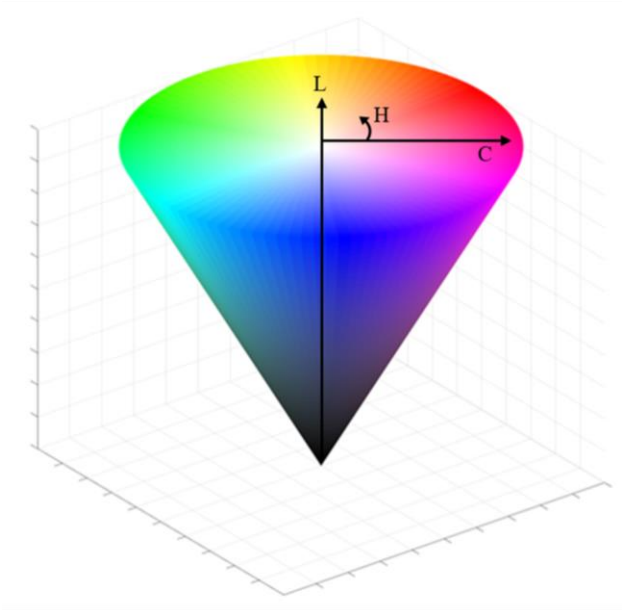

Figure 5.5. HCL vector-space with luminance on the z-axis, chroma on the x-y axis, and hue in degrees from -180° to 180°.

5.3.2 Hue, chroma, and luminance functions

To generate a sequential color palette the user selects an initial color, $P_i=[R_i, G_i, B_i]$, and a final color, $P_f=[R_f, G_f, B_f]$, along with a number of bins, N. We then transform P_i and P_f to equivalent colors in HCL-space (i.e., $P_i=[H_i, C_i, L_i]$ and $P_f=[H_f, C_f, L_f]$) using Sarifuddin's equations. We work entirely within HCL-space to build the intermediate palette members. The hue for each palette member is set by linearly interpolating between H_i and H_f. This is a particularly important step in creating color palettes for end users with reduced color vision acuity because it ensures that adjacent palette members have equal Euclidian spacing and thus, adjacent palette members are equally perceptually distinct. Additionally, the linear hue interpolation ensures the palette has an apparent logical order. The chroma value for each palette member is likewise set by

linearly interpolating between C_i and C_f. This method prevents the inclusion of perceptual "hot spots," or individual palette members that are significantly more intense or saturated than other palette members. Hot spots are problematic for end users because they can lead to inaccurate interpretations or place unintended emphasis on certain elements in the data product, even for those with unimpaired color vision.

For the sequential palette, luminance values are generated by convolving a normal distribution with a linear interpolation between L_i and L_f. The width of the normal distribution is proportional to the distance (in HCL-space) between starting and ending palette colors. The height of the normal distribution is proportional to the endmember luminance, taking into account how saturated in luminance the user-selected palette endmembers are. This prevents palette members from becoming "washed out" when the luminance value of one or both of the end members is high. This method generates larger first-order differences in luminance values where human sensitivity to luminance is low, and smaller differences where sensitivity is high, thereby ensuring adjacent palette members are perceptibly distinct while maintaining logical progression. Examples of HCL-generated palettes projected into RGB-space can be found in Figure 6.

To generate a divergent color palette, the user selects an initial color, P_i, a middle color, P_m, and a final color, P_f, along with the number of bins, N. Because creating logical divergent palettes requires discrete interpolation between P_i and P_m as well as between P_m and P_f, this inherently creates color palettes that are asymmetrical in length when N is even (divergent palettes with symmetrical length can only be created when $N-3 \in 2\mathbb{Z}$).

We handle even N inputs by allowing the color palette to be longer by one palette member between P_i and P_m than it is between P_m, and P_f.

We begin generating the divergent palette by performing the same transformation from RGB-space to HCL-space for P_i, P_m, and P_f. Hue and chroma functions are interpolated linearly from H_i to H_m and from H_m to H_f to maximize the perceptual distance between colors, produce a logical order, and prevent the inclusion of perceptual "hot spots", as discussed above. The same luminance function used in the creation of sequential palettes is used to find luminance values between H_i to H_m and from H_m to H_f. By calculating luminance values each half of the palette independently, we prevent the middle of the palette from becoming overly saturated or washed-out compared to the starting and ending palette members.

5.3.3 Transformation from HCL to RGB Color Space

To make AccessColor palettes usable for a broad range of applications, including data product visualization, we arrived at the conclusion that it is necessary to provide model output options in RGB-space in addition to HCL-space. The RGB model is ubiquitous and easily converted to other popular color spaces (e.g., CMYK), making it a logical format to support. However, the transformation from HCL-space to RGB-space is more complex than the transformation from RGB-space to HCL-space described previously. Each color space has different dimensions, and the size and shape of topological space used to describe colors can vary between different models. It is therefore possible to derive invalid values when converting from one model space to another. For example, the conversion from RGB to HCL is injective, while the conversion from HCL to RGB is surjective; this relationship is a natural result of HCL-

space utilizing parameters tied to human vision as a basis rather than staking the model parameters 1:1 to RGB-space. This inherently leads to the production of some colors in HCL-space that do not exist within RGB-space.

To prevent the inclusion of HCL palette members that are unsupported by the RGB model, we apply a least-squares minimization to identify the RGB color that is closest (in HCL-space) to the given HCL palette member. This ensures that the final-output RGB palette member is selected by choosing the RGB color that is mathematically, *perceptually* closest to the original HCL palette member. The final RGB output palette is then constructed by collecting the set of RGB-space colors that are closest to each respective HCL palette member.

The net result is the "real," allowable RGB value closest to the original, "true" color for each palette member. This conversion, though it diverges slightly from the optimized HCL palette that maximizes perceptual distance between member colors, ensures that an RGB color can be identified for each HCL palette member. HCL color space has not yet been widely adopted, so the transformation to RGB-space is necessary to achieve compatibility with most digital displays and a wide range of software applications. This also allows for easier conversion to other color spaces such as CMYK, which offers more flexibility and utility to the user. Overall, this capability extends use cases for AccessColor data products and provides the set of colors that is (to the human eye) perceptually closest to the optimized color palette. See Fig. 5.6, 5.7, and 5.8 for examples of single-hued sequential, multi-hued sequential, and diverging palette outputs, respectively.

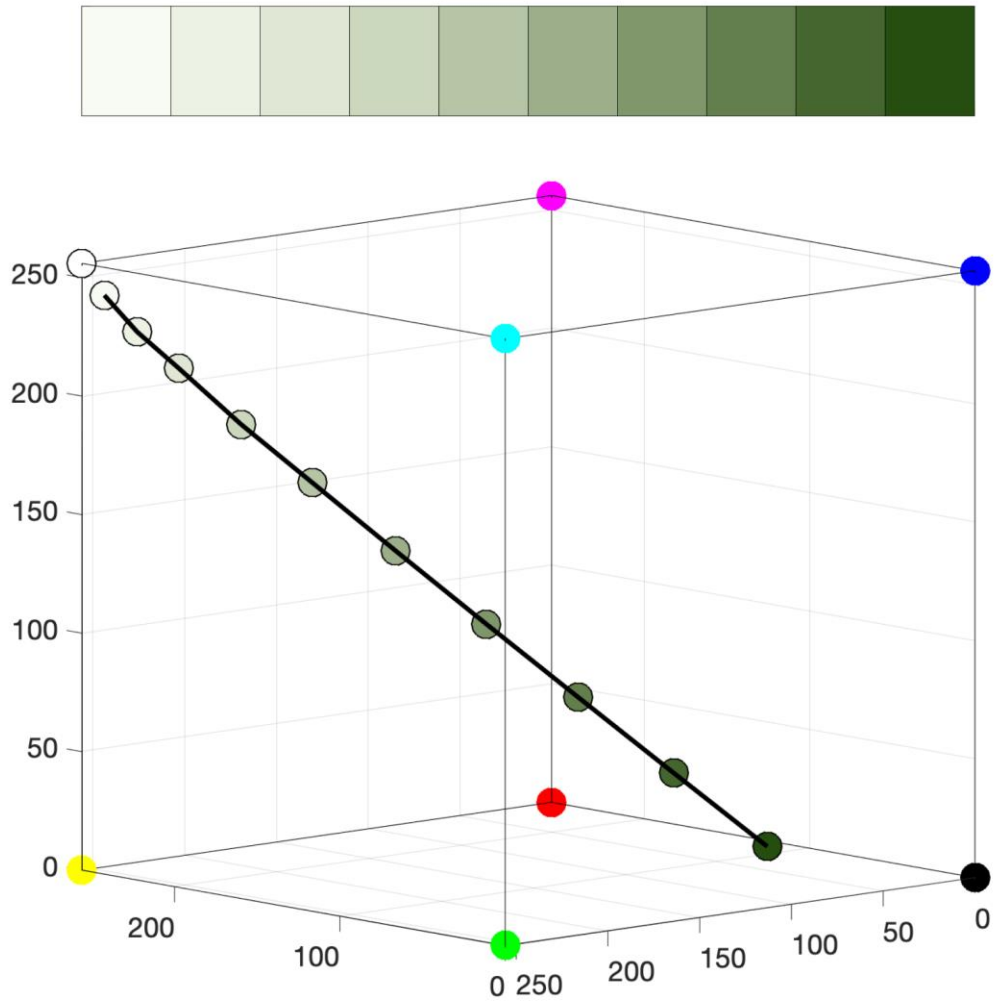

Figure 5.6. Single-hue, sequential palette generated by AccessColor web application. The palette members are plotted in RGB-space to highlight the variable Euclidian distance required between palette members to maintain perceptual uniformity.

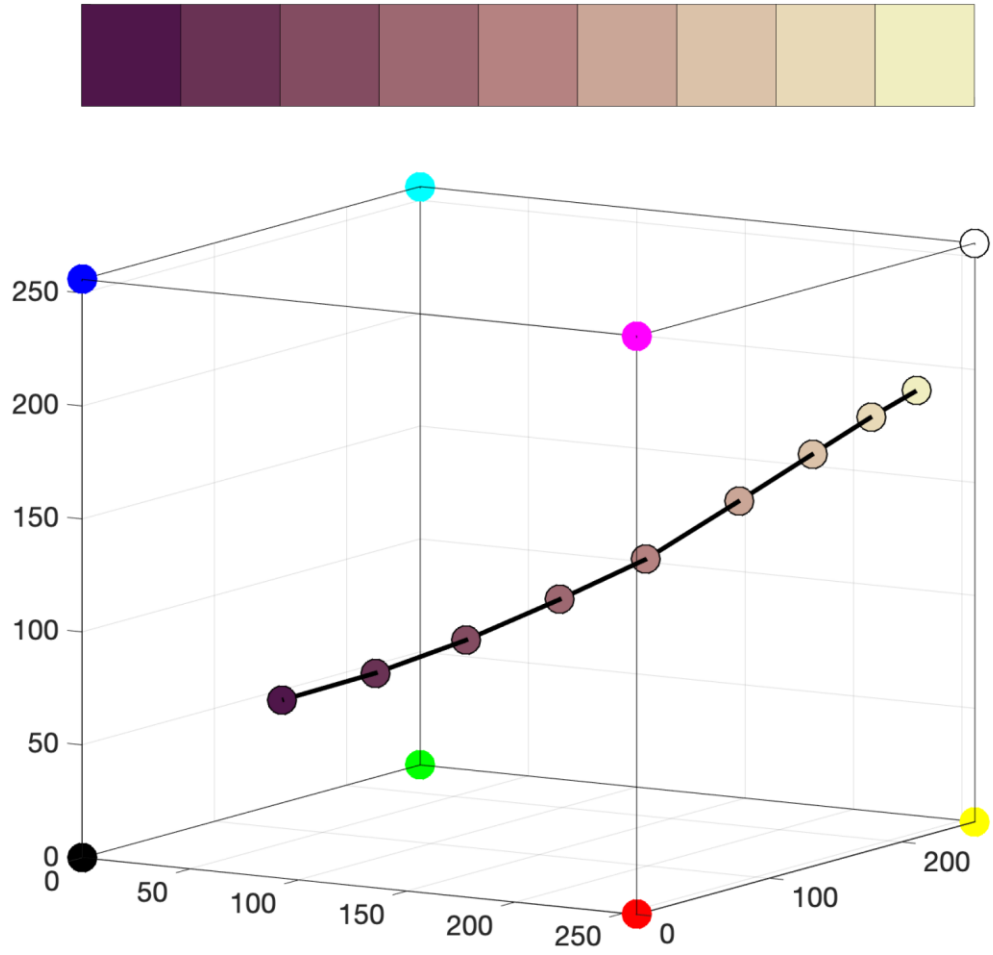

Figure 5.7. Multi- hue, sequential palette generated by AccessColor web application.

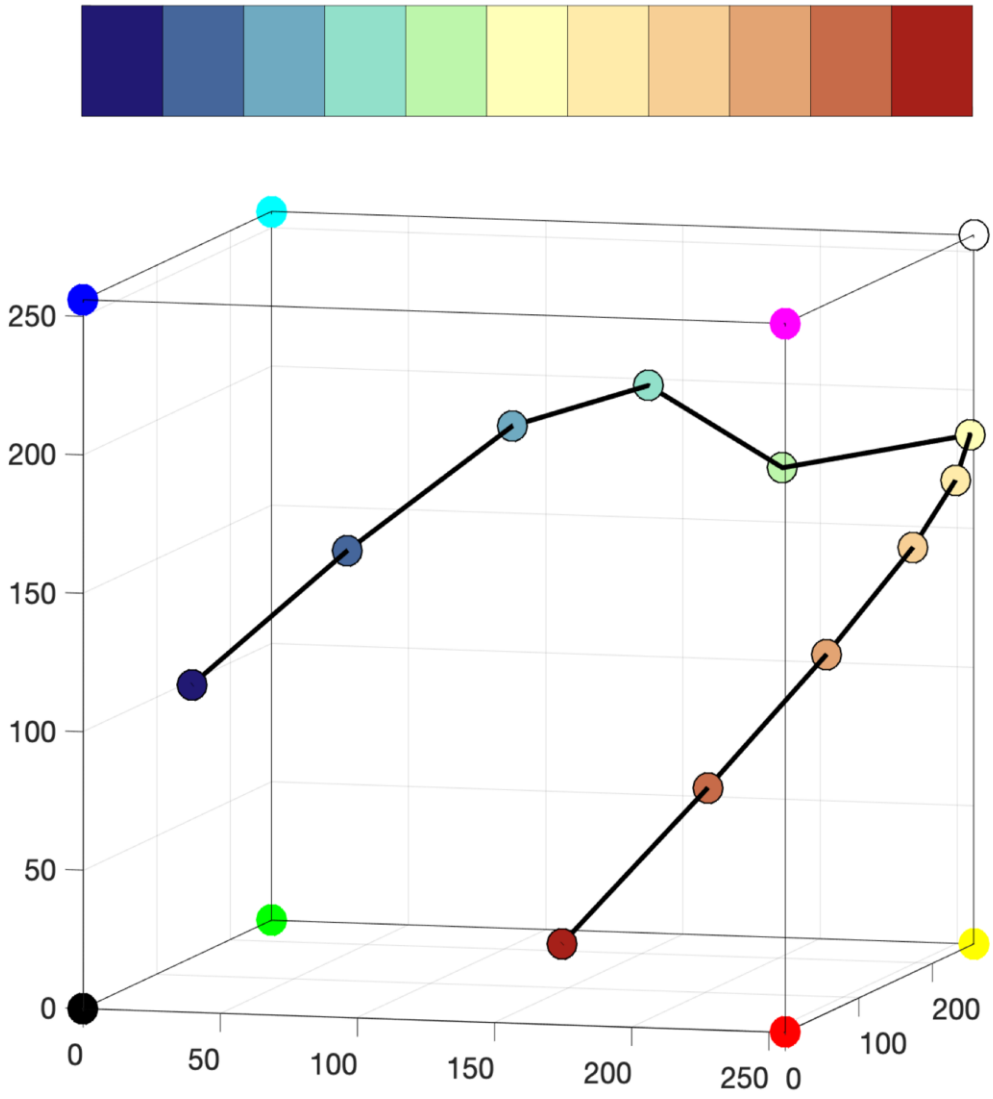

Figure 5.8. Multi-hue, divergent palette generated by AccessColor web application.

5.4 Limitations

The AccessColor model approach prioritizes maximizing the perceptual distance between palette members over generating aesthetically pleasing palettes. We choose not to restrict the number of available bins nor define a parameter for aesthetics because we favor the user's ability to choose semantically resonant colors and acknowledge the need for flexibility in a graphical display. To keep palettes CVD- accessible, we recommend

not exceeding ten bins for sequential palettes and 18 bins for diverging palettes. Furthermore, because aesthetics are a qualitative metric, we posit that the user should make their judgment in determining the intersection between aesthetically pleasing palettes and perceptually sound palettes produced by AccessColor.

5.5 Web Application

The AccessColor web application has reached alpha release and has been deployed internal to the Lunar Reconnaissance Orbiter Camera (LROC) instrument team server environment. Key capabilities of the web application include dynamically generating sequential and diverging color palettes based on user-selected color inputs. AccessColor offers graphical and textual controls for simplistic and intuitive input. The palette output is recalculated after changing any one of the parameters (e.g., start color, intermediate color, end color, the number of bins, or interpolation method), and the new palette is displayed to the user. AccessColor provides both graphical and textual output for the user to perform validation of palette suitability. The User can manually set hue interpolation to follow the shortest or longest path in HCL space, thereby reversing the sequence of hues used to build the palette from one end member to the other (see Fig. 5.9 for an example of this effect). The User can also change settings to manually toggle the Gaussian interpolation for luminance and chroma values, forcing AccessColor to use either linear interpolation or Gaussian interpolation for these values (see Fig. 5.10 for an example of this).

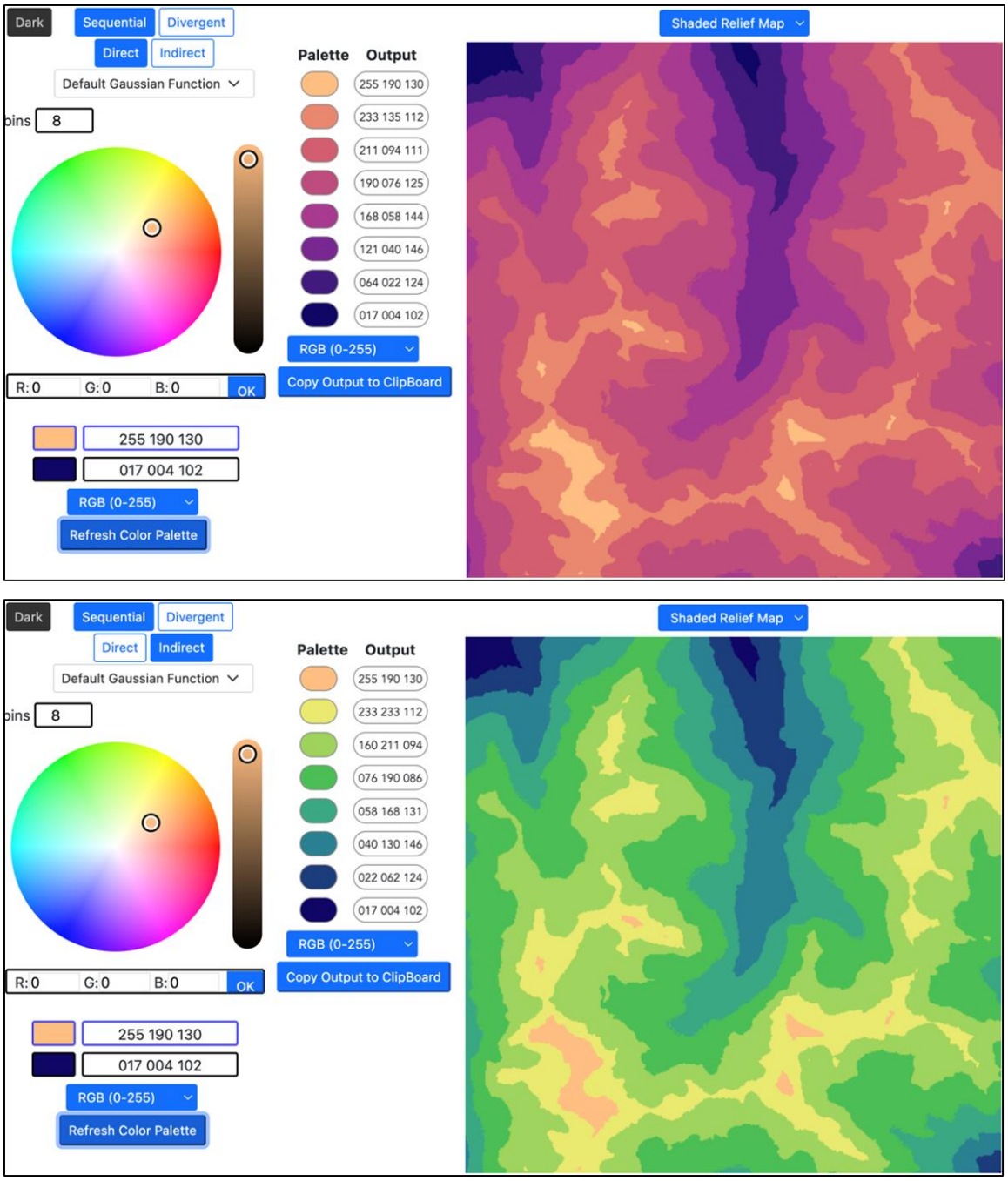

Figure 5.9. Users can toggle between Direct (top) and Indirect (bottom) interpolation, where Direct interpolates across the shortest distance and Indirect interpolates across the longest distance around the color wheel.

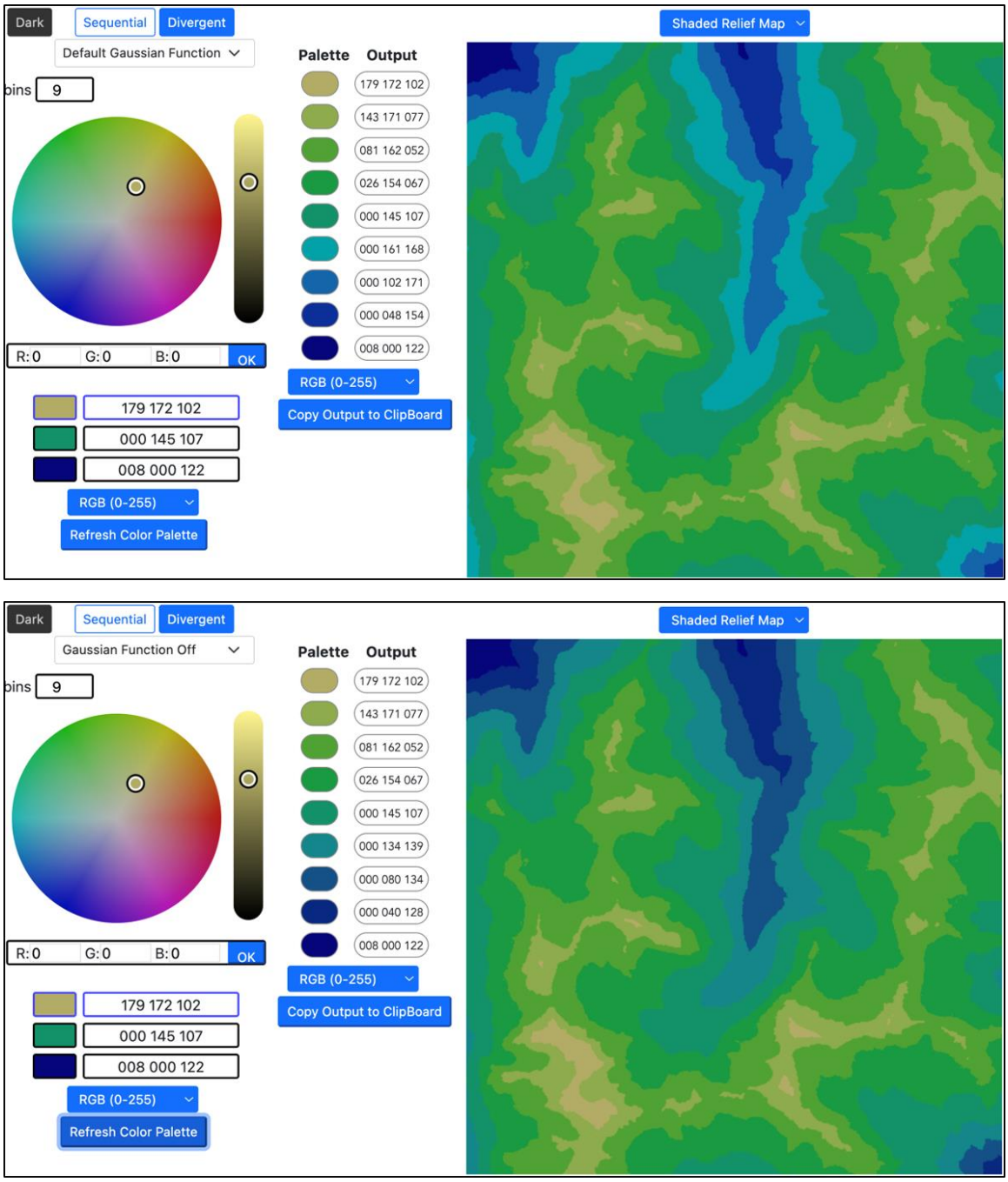

Figure 5.10. Users can toggle between Gaussian interpolation (top) and linear interpolation (bottom) of luminance and chroma values.

The primary output display is a series of "color swatches" (homogeneous squares corresponding to the color value of each palette member) along with text labels positively identifying each color. An auxiliary display demonstrates the application of the output palette to a sample data visualization, including a variety of plots and graphs and a topographic map (Fig. 5.11). Because colors appear less saturated on a dark background (Pitt and Winter, 1974), the User may toggle between a light theme and a dark theme to better assess the suitability of the output palette (Fig. 5.12). Additionally, the User may independently set their desired input and output formats, selecting from a handful of popular color models (RGB, CMYK, HCL).

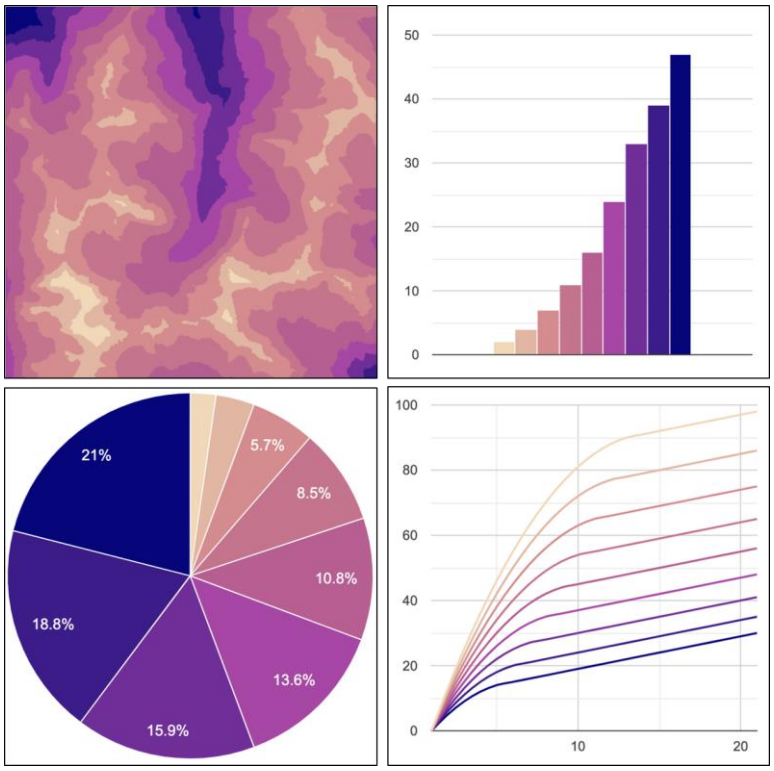

Figure 5.11. Auxiliary outputs provide visualizations for common data types, including a shaded relief map.

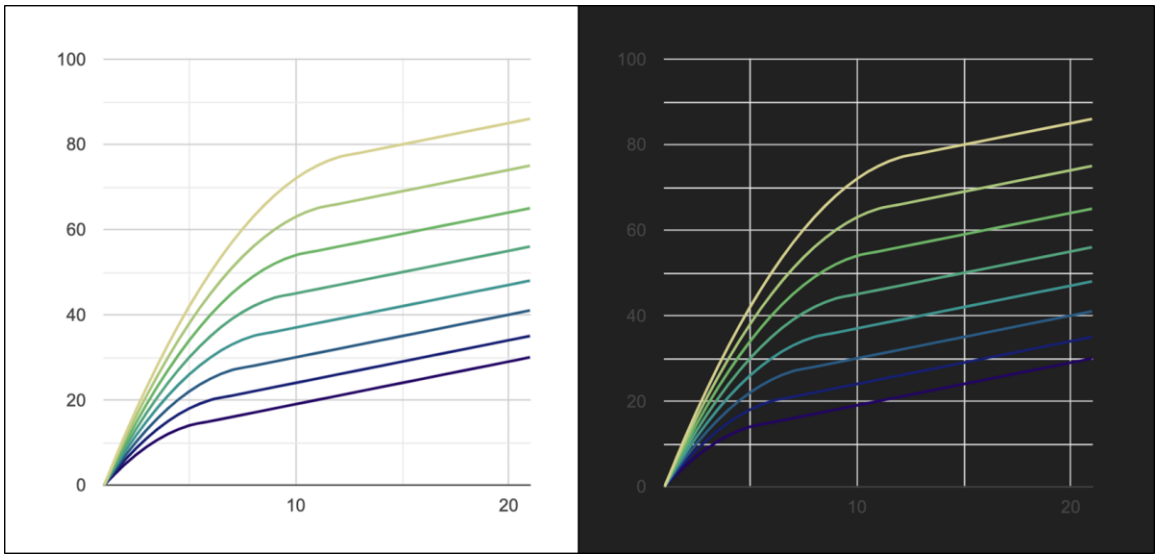

Figure 5.12. Users can toggle between Light Mode and Dark Mode to more easily discern the efficacy of their chosen color palette.

Future work will add support for color palette export/download, allowing the User to save the AccessColor output directly from the browser locally. Additional enhancements will include adapting the AccessColor web application for mobile users, including dynamic display options to scale between mobile and desktop scaling. This will include a multi-page view for mobile users, with adjustments to the core components and context-sensitive controls.

5.6 Summary

Countless domains depend on the interrogation of multiple datasets or multidimensional data and thus rely on color applied to images, plots, and figures to facilitate an understanding of the domain. Color often adds an extra dimension to data that serves to simplify the interpretation of complex information. Therefore, it is prudent to ensure that visualized data products have the widest possible reach by selecting color

palettes that are logically ordered and easily perceptible. A failure to make visualized data CVD-accessible inherently excludes approximately 9% of the target audience and reduces the effectiveness of these visualizations as a tool for communication.

In particular, those affected by CVD tend to have trouble with tasks that require color tracking, or matching colors across discrete regions of a plot, such as matching the color of one data set in a line plot to its corresponding entry in the legend (Brychtova and Coltekin, 2016). CVD also makes it more challenging to identify colors confined to small regions of a plot or map. In some cases, this can be remediated by avoiding the use of schema-like color gradients, which implicitly create broad zones of color that are perceptually near-uniform. Unsurprisingly, for those with CVD this color scheme is much more difficult to interpret. This difficulty likewise applies to the efficacy of controls, interfaces, and graphics when considering user experience. A control that is inaccessible or even ambiguous to 9% of target users is considered a failure from a User Interface or User Experience standpoint. Models like AccessColor, which create palettes from a perceptually uniform color space, allow the reader to overcome color vision barriers to experience and interpret visualized data. Increasing the perceptual distance between palette members is critical to using AccessColor to make visual aids more accessible. Most importantly, AccessColor extends the reach of data products and increases the efficacy of plots and charts for readers with CVD, without diminishing the experience for those with nominal color vision.

Palettes generated by AccessColor are optimized for ease of interpretation, with palette members that are both distinct from their neighbors and progress logically through color space. The perceptual uniformity and color constancy of HCL-space permits us to

use linearized hue and chroma functions, while a non-linear luminance function directly plays to the luminance sensitivity of the human eye; the difference between luminance values of adjacent pallet members increases where optical sensitivity is low and increases where sensitivity is high. This method reduces mid-palette skew, incorporating intermediate palette members with hue, saturation, or lightness values that deviate significantly from their nearest neighbors. AccessColor makes it easy for the user to select palettes suitable for a wide range of color acuities and uniquely suited for a given dataset.

5.7 References

Backhaus, W. (1998). Conscious and unconscious color vision in man and animals. Downward Processes in the Perception Representation Mechanisms, Singapore, New Jersey, London, Hong Kong: World Scientific, 373-389.

Birch, J. (2012). Worldwide prevalence of red-green color deficiency. JOSA A, 29(3), 313-320.

Bowmaker, J.K. and H.J. Dartnall (1980) Visual pigments of rods and cones in a human retina. The Journal of Physiology, 298.1, 501-511.

Brewer, C. A. (2003). A transition in improving maps: The ColorBrewer example. Cartography and Geographic Information Science, 30(2), 159-162.

Brown, P.K. and G. Wald (1964) Visual pigments in single rods and cones of the human retina. Science, 144(3614), 45-52.

Burnham, R. W., Hanes, R. M., & Bartleson, C. J. (1963). Color. Wiley.

Brychtova, A., & Coltekin, A. (2016). An empirical user study for measuring the influence of colour distance and font size in map reading using eye tracking. The cartographic journal, 53(3), 202-212.

Dannenmaier, W. D. (1972). The effect of color perception on success in high school biology. The Journal of Experimental Education, 41(2), 15-17.

Dartnall, H.J., J.K. Bowmaker, and J.D. Mollon (1983) Human visual pigments: Microspectrophotometric results from the eyes of seven persons. Proceedings of the Royal Society of London. Series B. Biological Sciences, 220(1218), 115-130.

Espinda, S. D. (1973). Color vision deficiency: a learning disability? Journal of Learning Disabilities, 6(3), 163-166.

Fairchild, M. D. (2013). Color appearance models. John Wiley & Sons.

Feig, K., & Ropers, H. H. (1978). On the incidence of unilateral and bilateral colour blindness in heterozygous females. Human Genetics, 41(3), 313-323.

Gramazio, C. C., Laidlaw, D. H., & Schloss, K. B. (2016). Colorgorical: Creating discriminable and preferable color palettes for information visualization. IEEE transactions on visualization and computer graphics, 23(1), 521-530.

Ibraheem, N. A., Hasan, M. M., Khan, R. Z., & Mishra, P. K. (2012). Understanding color models: a review. ARPN Journal of science and technology, 2(3), 265-275.

Jenny, B., & Kelso, N. V. (2007). Color design for the color vision impaired. Cartographic perspectives, (58), 61-67.

Judd, D. B. (1943). Facts of color-blindness. JOSA, 33(6), 294-307.

Kraft, T.W., J. Neitz, and M. Neitz (1998) Spectra of human L cones. Vision Research. 38(23), 3663-3670.

Kreissig, I., Lincoff, H., Witassek, B., & Kolling, G. (1981). Color vision and other parameters of macular function after retinal reattachment. Developments in ophthalmology, 2, 77-85.

McLaren, K. (1976). XIII—The development of the CIE 1976 (L* a* b*) uniform colour space and colour-difference formula. Journal of the Society of Dyers and Colourists, 92(9), 338-341.

Merbs, S.L. and J. Nathans (1992) Absorption spectra of human cone pigments. Nature. 356(6368), 433-435.

Munsell, A. H. (1919). A color notation. Munsell color company.

Neitz, J., M. Neitz, J.C. He, and S.K. Shevell (1999) Trichromatic color vision with only two spectrally distinct photopigments. Nature Neuroscience, 2(10), 884-888.

Oprian, D.D., A.B. Asenjo, N. Lee, and S.L. Pelletier (1991) Design, chemical synthesis, and expression of genes for the three human color vision pigments. Biochemistry, 30(48), 11367-11372.

Pitt, I.T. and L.M. Winter (1974) Effect of surround on perceived saturation. Journal of the Optical Society of America, 64(10), 1328-1331.

Purves, D., & Lotto, B. (2001). Explanation of some major features of color perception. Journal of Vision, 1(3), 60-60.

Sarifuddin, M., & Missaoui, R. (2005, August). A new perceptually uniform color space with associated color similarity measure for content-based image and video retrieval. In Proc. of ACM SIGIR 2005 workshop on multimedia information retrieval (MMIR 2005) (pp. 1-8).

Schnapf, J.L., T.W. Kraft, and D.A. Baylor (1987) Spectral sensitivity of human cone photoreceptors. Nature, 325(6103), 439-411.

Simunovic, M. P. (2010). Colour vision deficiency. Eye, 24(5), 747-755.

Spalding, J. A. (1999). Colour vision deficiency in the medical profession. British journal of general practice, 49(443), 469-475.

Taft, C. (1996). Color Meaning and Context: Comparisons of Semantic Ratings of Colors on Samples and Objects. Color Research and Application, 22(1), 40-50.

Tocantins, L. & Jones, H. (1933). Defective color vision and its handicaps in medicine. The American Journal of the Medical Sciences, 185(2), 243-248.

Wilkinson, W. K. (1992). The cognitive and social-emotional correlates of color deficiency in children: a literature review and analysis. Adolescence, 27(107), 603.

Wyszecki, G., & Stiles, W. S. (1982). Color science (Vol. 8). New York: Wiley.

REFERENCES

Adams, J. B. (1975). Interpretation of visible and near-infrared diffuse reflectance spectra of pyroxenes and other rock-forming minerals. Infrared and Raman spectroscopy of lunar and terrestrial minerals, 91-116.

An, Q., Zheng, L., & Luo, S. N. (2006). Vacancy-induced densification of silica glass. Journal of non-crystalline solids, 352(30-31), 3320-3325.

Balmain, K.G. (1980) Surface discharge effects, Space systems and their interactions with Earth's environment, Henry B. Garrett and Charles P. Pike, Progress in Astronautics and Aeronautics, 71, 276-298.

Bennett, C. J., Pirim, C., & Orlando, T. M. (2013). Space-weathering of solar system bodies: A laboratory perspective. *Chemical reviews*, *113(12)*, 9086-9150.

Blewett, D. T., Halekas, J., Ho, G. C., Greenhagen, B. T., Anderson, B. J., Vines, S. K., ... & Ames, W. F. (2022). Lunar Vertex: A Low-Cost Lander-Rover Investigation of Reiner Gamma. LPI Contributions, 2695, 6022.

Blewett, D. T., Denevi, B. W., Cahill, J. T., & Klima, R. L. (2021). Near-UV and near-IR reflectance studies of lunar swirls: Implications for nanosize iron content and the nature of anomalous space weathering. Icarus, 364, 114472.

Bradley, J. P., & Brownlee, D. E. (1986). Cometary particles: Thin sectioning and electron beam analysis. *Science*, *231*(4745), 1542-1544.

Budenstein, P.P. (1980) On the mechanism of dielectric breakdown in solids, IEEE Transactions on Electrical Insulation, 3, 225-240.

Buhler, C. R., C.I. Calle, J.S. Clements, J.G. Mantovani and M.L. Ritz (2007). Test method for in situ electrostatic characterization of lunar dust. IEEE Aerospace Conference, 1-19.

Burgess, K. D., & Stroud, R. M. (2017). Glassy with a Chance of Nanophase Iron: Space Weathering of Lunar Soil as Observed with Aberration-Corrected Scanning Transmission Electron Microscopy. *Microscopy Today*, *25*(3), 32-39.

Burgess, K. D., & Stroud, R. M. (2018). Coordinated Nano-Scale EDS and EELS Measurements of Lunar Space-Weathered Material. *Microscopy and Microanalysis*, *24*(S1), 716-717.

Burgess, K.D. and R. M. Stroud (2018) Phase dependent space weathering effects and spectroscopic identification retained helium in a lunar soil grain, Geochimica et Cosmochimica Acta, 244, 64-79.

Byron, B. D., Retherford, K. D., Greathouse, T. K., Mandt, K. E., Hendrix, A. R., Poston, M. J., ... & Mazarico, E. (2019). Effects of space weathering and porosity on the far-UV reflectance of Amundsen crater. Journal of Geophysical Research: Planets, 124(3), 823-836.

Carrez, P., Demyk, K., Cordier, P., Gengembre, L., Grimblot, J., D'HENDECOURT, L., ... & Leroux, H. (2002). Low-energy helium ion irradiation-induced amorphization and chemical changes in olivine: Insights for silicate dust evolution in the interstellar medium. *Meteoritics & Planetary Science*, *37*(11), 1599-1614.

Caturla, M. J., de La Rubia, T. D., Marques, L. A., & Gilmer, G. H. (1996). Ion-beam processing of silicon at keV energies: A molecular-dynamics study. *Physical Review B*, *54*(23), 16683.

Christoffersen, R., & Keller, L. P. (2015, March). Solar ion processing of Itokawa grains: Constraints on surface exposure times. In *Lunar and Planetary Science Conference* (No. JSC-CN-32917).

Christoffersen, R., Keller, L. P., & Dukes, C. (2020, March). The role of solar wind ion processing in space weathering of olivine: unraveling the paradox of laboratory irradiation results compared to observations of natural samples. In *Lunar and Planetary Science Conference* (No. JSC-E-DAA-TN78282).

Ciżman, A., E. Rysiakiewicz-Pasek, M. Krupiński, M. Konon, T. Antropova, & M. Marszałek (2017). The effect of Fe on the structure and electrical conductivity of sodium borosilicate glasses. Physical Chemistry Chemical Physics, 19(34), 23318-23324.

Cohen, M.E., S.M. Kuehner, J.H. Tepper, D.C. Burney, C.R. Neal, A.J. Irving, R.L. Korotev, and B. Hoefnagels (2019) Mineralogy and bulk composition of lunar mare basalt Northwest Africa 12008. 50th Lunar and Planetary Science Conference, abstract no. 2508.

Conel, J. E., & Nash, D. B. (1970). Spectral reflectance and albedo of Apollo 11 lunar samples: Effects of irradiation and vitrification and comparison with telescopic observations. *Geochimica et Cosmochimica Acta Supplement*, *1*, 2013.

Crider, D. H., & Vondrak, R. R. (2003). Space weathering effects on lunar cold trap deposits. *Journal of Geophysical Research: Planets*, *108*(E7).

Dhaher, N. H. (2017) Materials Science and Engineering. *CreateSpace Independent Publishing Platform*. ISBN-13: 978-1544083803.

Deca, J., Hemingway, D. J., Divin, A., Lue, C., Poppe, A. R., Garrick-Bethell, I., ... & Horányi, M. (2020). Simulating the reiner gamma swirl: the long-term effect of solar wind standoff. *Journal of Geophysical Research: Planets*, *125*(5), e2019JE006219.

Demers, H., Poirier-Demers, N., Couture, A. R., Joly, D., Guilmain, M., de Jonge, N., & Drouin, D. (2011). Three-dimensional electron microscopy simulation with the CASINO Monte Carlo software. Scanning, 33(3), 135-146.

Denevi, B. W., Robinson, M. S., Boyd, A. K., Blewett, D. T., & Klima, R. L. (2016). The distribution and extent of lunar swirls. *Icarus*, *273*, 53-67.

Denig, W.F. and A. R. Frederickson (1985) Deep-dielectric charging – A review, Environmental Research Papers, No. 919.

Devine, R. A. B. (1994). Macroscopic and microscopic effects of radiation in amorphous SiO2. Nuclear Instruments and Methods in Physics Research Section B: Beam Interactions with Materials and Atoms, 91(1-4), 378-390.

Dukes, C. A., Baragiola, R. A., & McFadden, L. A. (1999). Surface modification of olivine by H+ and He+ bombardment. *Journal of Geophysical Research: Planets*, *104*(E1), 1865-1872.

Fisher, E. A., Lucey, P. G., Lemelin, M., Greenhagen, B. T., Siegler, M. A., Mazarico, E., ... & Zuber, M. T. (2017). Evidence for surface water ice in the lunar polar regions using reflectance measurements from the Lunar Orbiter Laser Altimeter and temperature measurements from the Diviner Lunar Radiometer Experiment. *Icarus*, *292*, 74-85.

Fukumi, K., Chayahara, A., Satou, M., Hayakawa, J., Hangyo, M., & Nakashima, S. I. (1990). Surface structure of ion-implanted silica glass. *Japanese journal of applied physics*, *29*(5R), 905.

Frederickson, A.R. (1980) Radiation induced dielectric charging, Space systems and their interactions with Earth's space environment, Henry B. Garrett and Charles P. Pike, Progress in Astronautics and Aeronautics, 71, 386-412.

Frederickson, A.R., E.G. Holeman and E.G. Mullen (1992) Characteristics of spontaneous electrical discharging of various insulators in space radiations. IEEE Transactions on Electrical Insulation, 27(6), 1166-1178.

Garrett, H. B., & Evans, R. W. (2001). Internal electrostatic discharge environment at Jupiter.

Garrick-Bethell, I., J. W. Head III and C.M. Pieters (2011) Spectral properties, magnetic fields, and dust transport at lunar swirls, Icarus, 212(2), 480-492.

Gladstone, G. R., Stern, S. A., Retherford, K. D., Black, R. K., Slater, D. C., Davis, M. W., ... & Hendrix, A. R. (2010). LAMP: the Lyman alpha mapping project on NASA's Lunar reconnaissance orbiter mission. Space Science Reviews, 150, 161-181.

Glotch, T.D., J.L. Bandfield, P.G. Lucey, P.O. Hayne, B.T. Greenhagen, J.A. Arnold, R.R. Ghent and D.A. Paige (2015) Formation of lunar swirls by magnetic field standoff of the solar wind, Nature Communications, 6(1), 1-8.

Gold, T. (1955). The lunar surface. *Monthly Notices of the Royal Astronomical Society*, *115*(6), 585-604.

Goldberg, R. D., Williams, J. S., & Elliman, R. G. (1995). Amorphization of silicon by elevated temperature ion irradiation. *Nuclear Instruments and Methods in Physics Research Section B: Beam Interactions with Materials and Atoms*, *106*(1-4), 242-247.

Green, N.W. and A.R. Frederickson (2006) A study of spacecraft charging due to exposure to interplanetary protons, AIP Conference Proceedings, 813(1), 684-700.

Green, N. W., & Dennison, J. R. (2008). Deep dielectric charging of spacecraft polymers by energetic protons. IEEE transactions on plasma science, 36(5), 2482-2490.

Guo, B.-H., G.-Y. Sun, S. Zhang, J.-Y. Xue, R.D. Zhou, B.-P. Song, H.-B. Mu, and G.-J. Zhang (2019) Mechanism of vacuum flashover on surface roughness, Journal of Physics D: Applied Physics, 52, 215301.

Halekas, J. S., Mitchell, D. L., Lin, R. P., Frey, S., Hood, L. L., Acuña, M. H., & Binder, A. B. (2001). Mapping of crustal magnetic anomalies on the lunar near side by the Lunar Prospector electron reflectometer. *Journal of Geophysical Research: Planets*, *106*(E11), 27841-27852.

Hapke, B. (1965). Effects of a simulated solar wind on the photometric properties of rocks and powders. *Annals of the New York Academy of Sciences*, *123*(1), 711-721.

Hapke, B. W., Cohen, A. J., Cassidy, W. A., & Wells, E. N. (1970). Solar radiation effects on the optical properties of Apollo 11 samples. *Geochimica et Cosmochimica Acta Supplement*, *1*, 2199.

Hapke, B. (1973). Darkening of silicate rock powders by solar wind sputtering. *The Moon*, *7*(3-4), 342-355.

Hapke, B., Cassidy, W., & Wells, E. (1975). Effects of vapor-phase deposition processes on the optical, chemical, and magnetic properties OE the lunar regolith. *The moon*, *13*(1), 339-353.

Hapke, B. (2001) Space weathering from Mercury to the asteroid belt, *Journal of Geophysical Research, 106*, 10039-10074.

Harries, D., & Langenhorst, F. (2014). The mineralogy and space weathering of a regolith grain from 25143 Itokawa and the possibility of annealed solar wind damage. *Earth, Planets and Space*, *66*(1), 1-11.

Hemingway, D.J., I. Garrick-Bethell and M.A. Kreslavsky (2015) Latitudinal variation in spectral properties of the lunar maria and implications for space weathering, Icarus, 261, 66-79.

Hendrix, A. R., Greathouse, T. K., Retherford, K. D., Mandt, K. E., Gladstone, G. R., Kaufmann, D. E., ... & Cahill, J. T. S. (2016). Lunar swirls: far-UV characteristics. *Icarus*, *273*, 68-74.

Hirsch, S., Klein, H., & Jung, P. (2005). Dimensional changes of silica-, borosilicate-and germania-glasses and quartz under irradiation. *Journal of non-crystalline solids*, *351*(40-42), 3279-3288.

Hood, L. L., Zakharian, A., Halekas, J., Mitchell, D. L., Lin, R. P., Acuña, M. H., & Binder, A. B. (2001). Initial mapping and interpretation of lunar crustal magnetic anomalies using Lunar Prospector magnetometer data. *Journal of Geophysical Research: Planets*, *106*(E11), 27825-27839.

Housley, R. M., Grant, R. W., & Paton, N. E. (1973). Origin and characteristics of excess Fe metal in lunar glass welded aggregates. In *Lunar and Planetary Science Conference Proceedings* (Vol. 4, p. 2737).

Jordan, A.P., T.J. Stubbs, J.K. Wilson, N.A. Schwadron, H.E. Spence, and C.J. Joyce (2014) Deep dielectric charging of regolith within the Moon's permanently shadowed regions, *Journal of Geophysical Research: Planets, 119*, 1806-1821.

Huang, Z., Nomura, K. I., Morrissey, L. S., & Wang, J. (2022). Molecular dynamics simulation of solar wind implantation in the permanently shadowed regions on the lunar surface. *Geophysical Research Letters*, *49*(18), e2022GL099333.

Izenberg, N. R., Drabenstadt, C. W., Nichols, J. R., Jordan, A. P., & Stubbs, T. J. (2018). Pilot Experiments in Dielectric Breakdown Space Weathering of Planetary

Regolith Analogs. In 49th Annual Lunar and Planetary Science Conference (No. 2083).

Jin, C., Suenaga, K., & Iijima, S. (2008). Vacancy migrations in carbon nanotubes. *Nano letters*, *8*(4), 1127-1130.

Jordan, A.P., T.J. Stubbs, J.K. Wilson, N.A. Schwadron, H.E. Spence, and C.J. Joyce (2014) Deep dielectric charging of regolith within the Moon's permanently shadowed regions, Journal of Geophysical Research: Planets, 119, 1806-1821.

Jordan, A.P., T.J. Stubbs, J.K. Wilson, N.A. Schwadron and H.E. Spence (2015) Dielectric breakdown weathering of the Moon's polar regolith, *Journal of Geophysical Research: Planets, 120,* 210-225.

Jordan, A.P., T.J. Stubbs, J.K. Wilson, N.A. Schwadron and H.E. Spence (2017) The rate of dielectric breakdown weathering of lunar regolith in permanently shadowed regions, *Icarus, 283,* 352-358.

Jordan, A. P., T. J. Stubbs, M. L. Shusterman, N. R. Izenberg, J. K. Wilson, P. O. Hayne, N. A. Schwadron and H. E. Spence (2019) How dielectric breakdown may contribute to the global weathering of regolith on the Moon. Icarus, 319, 785-794.

Jordan, A. P. (2021). Evidence for dielectric breakdown weathering on the Moon. *Icarus*, *358*, 114199.

Jordan, A. P., Case, A. W., Wilson, J. K., & Huang, C. L. (2022). Evidence that Earth's magnetotail affects dielectric breakdown weathering on the Moon. *Icarus*, *383*, 115011.

Kallio, E., Dyadechkin, S., Wurz, P., & Khodachenko, M. (2019). Space weathering on the Moon: Farside-nearside solar wind precipitation asymmetry. *Planetary and space science*, *166*, 9-22.

Lemelin, M., Lucey, P. G., Neumann, G. A., Mazarico, E. M., Barker, M. K., Kakazu, A., ... & Zuber, M. T. (2016). Improved calibration of reflectance data from the LRO Lunar Orbiter Laser Altimeter (LOLA) and implications for space weathering. *Icarus*, *273*, 315-328.

Lucey, P. G., Neumann, G. A., Riner, M. A., Mazarico, E., Smith, D. E., Zuber, M. T., ... & Song, E. (2014). The global albedo of the Moon at 1064 nm from LOLA. *Journal of Geophysical Research: Planets*, *119*(7), 1665-1679.

Keller, L. P. & McKay, D. S. (1993). Discovery of vapor deposits in the lunar regolith. *Science, 261*(5126), 1305-1307.

Keller, L. P., & McKay, D. S. (1997). The nature and origin of rims on lunar soil grains. *Geochimica et Cosmochimica Acta*, *61*(11), 2331-2341.

Keller, L. P., & Clemett, S. J. (2001, March). Formation of nanophase iron in the lunar regolith. In *Lunar and Planetary Science Conference* (Vol. 32).

Keller, L. P., & Berger, E. L. (2014). *Space Weathering of Olivine in Lunar Soils: A Comparison to Itokawa Regolith Samples* (No. JSC-CN-31645).

Keller, L. P., & Zhang, S. (2015, November). Rates of space weathering in lunar soils. In *Space weathering of airless bodies: An integration of remote sensing data, laboratory experiments and sample analysis workshop* (Vol. 1878, p. 2056).

Keller, L. P., Berger, E. L., Christoffersen, R., & Zhang, S. (2016, March). Direct determination of the space weathering rates in lunar soils and Itokawa regolith from sample analyses. In *Lunar and Planetary Science Conference* (No. JSC-CN-35490).

Keller, L. P., Berger, E. L., Zhang, S., & Christoffersen, R. (2021). Solar energetic particle tracks in lunar samples: A transmission electron microscope calibration and implications for lunar space weathering. *Meteoritics & Planetary Science*, *56*(9), 1685-1707.

Lemelle, L., L. Beaunier, S. Borensztajn, M. Fialin and F. Guyot (2003) Destabilization of olivine by 30-keV electron irradiation: A possible mechanism of space weathering affecting interplanetary dust particles and planetary surfaces, Geochimica et Cosmochimica Acta, 67(10), 1901-1910.

Li, S., & Milliken, R. E. (2017). Water on the surface of the Moon as seen by the Moon Mineralogy Mapper: Distribution, abundance, and origins. *Science advances*, *3*(9), e1701471.

Li, Y., Li, X., Wang, S., Li, S., Tang, H., & Coulson, I. M. (2013). Crystal orientation results in different amorphization of olivine during solar wind implantation. *Journal of Geophysical Research: Planets*, *118*(10), 1974-1982.

Lucey, P.G., G.A. Neumann, M.A. Riner, E. Mazarico, D.E. Smith, M.T. Zuber, D.A. Paige, D.B. Bussey, J.T. Cahill, A. McGovern and P. Isaacson (2014) The global albedo of the Moon at 1064 nm from LOLA, Journal of Geophysical Research: Planets, 119(7), 1665-1679.

Lue, C., Futaana, Y., Barabash, S., Wieser, M., Holmström, M., Bhardwaj, A., ... & Wurz, P. (2011). Strong influence of lunar crustal fields on the solar wind flow. *Geophysical Research Letters*, *38*(3).

Märk, T. D. (1994). Mechanisms and Kinetics of Electron Impact Ionization of Atoms, Molecules, and Clusters. In *Linking the Gaseous and Condensed Phases of Matter* (pp. 155-182). Springer, Boston, MA.

Matsumoto, T., Tsuchiyama, A., Miyake, A., Noguchi, T., Nakamura, M., Uesugi, K., ... & Nakano, T. (2015). Surface and internal structures of a space-weathered rim of an Itokawa regolith particle. *Icarus*, *257*, 230-238.

McFadden, J., Garrick-Bethell, I., Sim, C. K., Kim, S. S., & Hemingway, D. (2019). Iron content determines how space weathering flux variations affect lunar soils. *Icarus*, *333*, 323-342.

McGuire, R.E. and T.T. von Rosenvinge (1984) The energy spectra of solar energetic particles, Advances in Space Research, 4(2-3), 117-125.

Miller, H.C. (2015) Flashover of insulators in vacuum: The last twenty years, IEEE Transactions on Dielectrics and Electrical Insulation, 22(6), 3641-3657.

Moroz, L. V., Starukhina, L. V., Rout, S. S., Sasaki, S., Helbert, J., Baither, D., ... & Hiesinger, H. (2014). a. Icarus, 235, 187-206.

Morris, R. V. (1976). Surface exposure indices of lunar rocks: A comparative FMR study. *Proceedings of the Seventh Lunar Planetary Science Conference*, *7*, 315-335.

Nishino, M. N., Saito, Y., Tsunakawa, H., Takahashi, F., Fujimoto, M., Harada, Y., ... & Shimizu, H. (2015). Electrons on closed field lines of lunar crustal fields in the solar wind wake. *Icarus*, *250*, 238-248.

Noble, S. K., Pieters, C. M. & Keller, L. P. (2007). An experimental approach to understanding the optical effects of space weathering. *Icarus, 192*(2), 629-642.

Pelaz, L., Marqués, L. A., Aboy, M., Barbolla, J., & Gilmer, G. H. (2003). Atomistic modeling of amorphization and recrystallization in silicon. *Applied physics letters*, *82*(13), 2038-2040.

Piao, F., Oldham, W. G., & Haller, E. E. (2000). The mechanism of radiation-induced compaction in vitreous silica. *Journal of non-crystalline solids, 276*(1-3), 61-71.

Pieters, C. M., Taylor, L. A., Noble, S. K., Keller, L. P., Hapke, B., Morris, R. V., ... & Wentworth, S. (2000). Space weathering on airless bodies: Resolving a mystery with lunar samples. *Meteoritics & Planetary Science*, *35*(5), 1101-1107.

Pieters, C. M., & Noble, S. K. (2016). Space weathering on airless bodies. *Journal of Geophysical Research: Planets*, *121*(10), 1865-1884.

Poppe, A. R., Farrell, W. M., & Halekas, J. S. (2018). Formation timescales of amorphous rims on lunar grains derived from ARTEMIS observations. *Journal of Geophysical Research: Planets*, *123*(1), 37-46.

Qiao, L., Ling, Z., Head, J. W., Ivanov, M. A., & Liu, B. (2019). Analyses of Lunar Orbiter Laser Altimeter 1,064-nm albedo in permanently shadowed regions of polar crater flat floors: Implications for surface water ice occurrence and future in situ exploration. *Earth and Space Science*, *6*(3), 467-488.

Robinson, M. S., Mahanti, P., Carter, L. M., Denevi, B. W., Estes, N. M., Ravine, M. A., ... & Wagner, R. V. (2017). ShadowCam—Seeing in the dark. In Proceedings of the European Planetary Science Congress, Riga, Latvia (pp. 17-22).

Rosenberg, D. L., & Wehner, G. K. (1964). Darkening of powdered basalt by simulated solar-wind bombardment. *Journal of Geophysical Research*, *69*(15), 3307-3308.

Rhodes, D. J., & Farrell, W. M. (2020). Mapping the Predicted Solar Wind Hydrogen Flux in Lunar South Pole Craters. The Planetary Science Journal, 1(1), 13.

Shusterman, M. L., Sharp, T. G., & Robinson, M. S. (2021, March). Dielectric Breakdown Weathering: Morphological Effects of Electrical Breakdown in Laboratory-Irradiated San Carlos Olivine. In Lunar and Planetary Science Conference (No. 2548, p. 2141).

Shusterman, M. L., Izenberg, N. R., Wing, B. R., Irvin, B. L., & Liang, S. X. (2016). Laboratory Simulation of Dielectric Breakdown of Lunar Regolith Simulant JSC-1A. In Annual Meeting of the Lunar Exploration Analysis Group (Vol. 1960, p. 5056).

Sickafus, K. E., Kotomin, E. A., & Uberuaga, B. P. (Eds.). (2007). *Radiation effects in solids* (Vol. 235). Springer Science & Business Media.

Sim, C. K., Choi, Y. J., Ye, S. J., Jin, H., Seon, J., Kim, S. S., ... & Team, C. K. (2021, March). Korea's First Scientific Instruments on the Lunar Surface. In 52nd Lunar and Planetary Science Conference (No. 2548, p. 1806).

Sim, C. K., Kim, S. S., Lucey, P. G., Garrick-Bethell, I., & Choi, Y. J. (2017). Asymmetric space weathering on lunar crater walls. *Geophysical Research Letters*, *44*(22), 11-273.

Sirk, A. H., Sadoway, D. R., & Sibille, L. (2010). Direct electrolysis of molten lunar regolith for the production of oxygen and metals on the moon. ECS transactions, 28(6), 367.

Sørensen, J., D.J. Rodgers, K.A. Ryden, P.M. Latham, G.L. Wrenn, L. Levy and G. Panabiere (1999) ESA's tools for internal charging, RADECS 99 (Cat. No. 99TH8471), 27-33.

Starukhina, L. V. (2006). Polar regions of the moon as a potential repository of solar-wind-implanted gases. *Advances in Space Research*, *37*(1), 50-58.

Strangway, D. W., Chapman, W. B., Olhoeft, G. R., & Carnes, J. (1972). Electrical properties of lunar soil dependence on frequency, temperature and moisture. Earth and Planetary Science Letters, 16(2), 275-281.

Stubbs, T.J., W.M. Farrell, J.S. Halekas, J.K. Burchill, M.R. Collier, M.I. Zimmerman, R.R. Vondrak, G.T. Delory, and R.F. Pfaff (2014) Dependence of lunar surface charging on solar wind plasma conditions and solar irradiation. Planetary and Space Science, 90, 10-27.

Tan, C. Z., Arndt, J., & Xie, H. S. (1998). Optical properties of densified silica glasses. *Physica B: Condensed Matter*, *252*(1-2), 28-33.

Thompson, M. S., Zega, T. J., Becerra, P., Keane, J. T., & Byrne, S. (2016). The oxidation state of nanophase Fe particles in lunar soil: Implications for space weathering. *Meteoritics & Planetary Science*, *51*(6), 1082-1095.

Tsunakawa, H., Takahashi, F., Shimizu, H., Shibuya, H., & Matsushima, M. (2015). Surface vector mapping of magnetic anomalies over the Moon using Kaguya and Lunar Prospector observations. *Journal of Geophysical Research: Planets*, *120*(6), 1160-1185.

Wallace, J. B., Bayu Aji, L. B., Shao, L., & Kucheyev, S. O. (2019). Impact of pre-existing disorder on radiation defect dynamics in Si. *Scientific Reports*, *9*(1), 1-7.

Wang, D., M. Mookherjee, Y. Xu, and S. Karato (2006) The effects of water on the electrical conductivity in olivine, Nature, 443, 977-980.

Wang, K., Moynier, F., Podosek, F. A., & Foriel, J. (2012). An iron isotope perspective on the origin of the nanophase metallic iron in lunar regolith. Earth and Planetary Science Letters, 337, 17-24.

Wang, L. M., & Ewing, R. C. (1992). Ion-beam-induced amorphization of complex ceramic materials—minerals. *MRS Bulletin*, *17*(5), 38-44.

Wehner, G. K., Kenknight, C. E., & Rosenberg, D. (1963). Modification of the lunar surface by the solar-wind bombardment. *Planetary and Space Science*, *11*(11), 1257-1261.

Wentworth, S. J., Keller, L. P., McKAY, D. S., & Morris, R. V. (1999). Space weathering on the Moon: Patina on Apollo 17 samples 75075 and 76015. *Meteoritics & Planetary Science*, *34*(4), 593-603.

Wöhler, C., Grumpe, A., Berezhnoy, A. A., & Shevchenko, V. V. (2017). Time-of-day–dependent global distribution of lunar surficial water/hydroxyl. *Science advances*, *3*(9), e1701286.

Wolak, M.A., A.S. Wan, J.S. Shirk, M. Mackey, A. Hiltner, and E. Baer (2012) Imaging the effect of dielectric breakdown in a multilayered polymer film, Journal of applied polymer science, 123(4), 2548-2557.

Yang, X., H. Keppler, C. McCammon, H. Ni, Q. K. Xia and Q. Fan (2011) Effect of water on the electrical conductivity of lower crustal clinopyroxene, Journal of Geophysical Research, 116(B4).

Yang, X., H. Keppler, C. McCammon, H. Ni (2012) Electrical conductivity of orthopyroxene and plagioclase in the lower crust, Contributions to Mineralogy and Petrology, 163(1), 33-48.

Ziegler, J. F., Ziegler, M. D., & Biersack, J. P. (2010). SRIM–The stopping and range of ions in matter (2010). *Nuclear Instruments and Methods in Physics Research Section B: Beam Interactions with Materials and Atoms*, *268*(11-12), 1818-1823.

Zimmerman, M. I., Farrell, W. M., Stubbs, T. J., Halekas, J. S., & Jackson, T. L. (2011). Solar wind access to lunar polar craters: Feedback between surface charging and plasma expansion. Geophysical research letters, 38(19).

Zuber, M. T., Head, J. W., Smith, D. E., Neumann, G. A., Mazarico, E., Torrence, M. H., ... & Melosh, H. J. (2012). Constraints on the volatile distribution within Shackleton crater at the lunar south pole. Nature, 486(7403), 378-381.

APPENDIX A

RELEASE OF WORKS SUBMITTED FOR PUBLICATION

CHAPTER 3 RELEASE

Chapter 3 of this dissertation, entitled “Deep Dielectric Breakdown of Silicates: Microstructural Damage and Implications for Lunar Space Weathering,” has been submitted to the *American Astronomical Society Journal* for publication. Co-authors of this work, including Andrew P. Jordan, Mark S. Robinson, and Thomas G. Sharp, have granted permission to include the article as a chapter in this dissertation.

CHAPTER 5 RELEASE

Chapter 5 of this dissertation, entitled “AccessColor: Producing Palettes for Diverse Color Acuities,” has been submitted to the *Journal of Geoscience Education* for publication. Co-authors of this work, including Chandler F. Chamberlain, Mark S. Robinson, Steven Semken, Cameron Sim, and Benjamin R. Wing, have granted permission to include the article as a chapter in this dissertation.